Heavy Precipitation Events in the Western Mediterranean Area: Physical Processes and Predictability

Zur Erlangung des akademischen Grades eines
DOKTORS DER NATURWISSENSCHAFTEN

von der Fakultät für Physik
des Karlsruher Instituts für Technologie (KIT)

genehmigte
DISSERTATION

von

Dipl.-Met. Luisa Röhner

aus Freiburg im Breisgau

Abstract

Heavy precipitation events in the western Mediterranean area often lead to large social and economic impacts. Especially in late summer and in autumn, rainfall systems can be fed efficiently by warm and moist air masses in low tropospheric levels. Due to complex interactions of various lifting mechanisms and the steep Mediterranean coastal orography, the initiation and the development of those heavy precipitation events is not fully understood. Even more, the accurate prediction of severe weather events remains challenging. The improvement of the predictability of those events is a main subject of current meteorological research.

Within this thesis, the physical processes and the predictability of two prototypic heavy precipitation events in the western Mediterranean area are studied in detail. A synoptically strongly forced event, embedded in a large-scale environment suitable for synoptic-scale uplift, led to significant daily rainfall amounts locally exceeding 200 mm. By simulations with the numerical weather prediction model COSMO and by the analysis of meteorological measurements, a mesoscale low-level horizontal moisture flux convergence line and orographic uplift at the Spanish Mediterranean coast were identified as the two main mechanisms associated with the initiation and the development of deep moist convection and subsequent heavy precipitation. By an investigation of Lagrangian trajectories, the relevant moisture sources for the evaluated case were found to be located in the Mediterranean Sea itself and in the northeastern Atlantic Ocean.

A novel methodology was applied to assess and to improve the predictability of this heavy precipitation event. Five numerical ensemble simulations, based on diverse percentages of two different sources of atmospheric uncertainty, were carried out. Synoptic-scale uncertainty (i.e. large-scale uncertainty) was introduced by various initial and boundary conditions whereas convective-scale uncertainty (i.e. small-scale uncertainty) was gained by a stochastic parameterization scheme for cumulus convection. The evaluation of the ensemble output was performed in comparison to a synoptically weaker forced heavy precipitation event. Regarding the synoptically stronger forced event, a proportionally larger influence of synoptic-scale uncertainty led to a better ensemble performance. Concerning the weaker forced case, an overdispersive ensemble resulted for the settings with more than 50% of synoptic-scale uncertainty. By the use of less large-scale uncertainty, remaining computational resources can be used for the additional implementation of small-scale uncertainty, realized with the stochastic parameterization scheme. The best performance was achieved for the ensemble with equally distributed sources of uncertainties.

Contents

Contents

1 Introduction

The study of heavy precipitation events in the western Mediterranean area is the main subject of this thesis. Typically, their occurrence is most pronounced in late summer and autumn. With daily precipitation amounts that can exceed 800 mm (Ramis et al., 2013), they are often responsible for large social and economic impacts (e.g. Llasat-Botija et al., 2007). Conceptual models of how heavy precipitation in the western Mediterranean is produced highlight several main features. Often, a cyclone is located in the vicinity of the affected rainfall area. By an organized low-level flow, high amounts of warm and moist air from the Mediterranean Sea can be advected into target regions, prone to the initiation of deep convection (e.g. Jansà et al., 2001). Synoptically, those regions are characterized by positive vorticity advection in upper levels and warm air advection at low levels (e.g. Romero et al., 1999). Together with humid surface air, a potentially unstable atmosphere can result. Through a trigger mechanism, the moist low-level air can be lifted up to the level of free convection. Further uplift and associated condensation can then lead to deep moist convection and resulting heavy precipitation (e.g. Doswell et al., 1996). With a persistent feeding of moist air towards the convective systems, highly efficient precipitation can be sustained. Although those general concepts are understood, non-linear interactions of the synoptic situation with various possible mesoscale lifting mechanisms and the complex Mediterranean orography still results in a lack of knowledge concerning the accurate initiation and development of Mediterranean heavy precipitation events. Particularly regarding the strongest of the heavy rainfall cases, progress in the numerical weather forecast of those events has to be achieved (Drobinski et al., 2014).

To assess the predictability of weather events, ensemble predictions are used. Starting from an initial atmospheric state, small perturbations of those initial conditions can lead to different solutions of the future atmospheric conditions (Lorenz, 1963). Further uncertainties regarding the later atmospheric state exist in the description of physical sub-scale processes in the numerical weather prediction systems. Different parameterizations of sub-scale processes cause various temporal developments of the physical parameters (e.g. Palmer et al., 2005). To reproduce this uncertainty in the numerical weather forecast, an ensemble prediction system with a set of several single forecasts is used. It intends to reflect the chaotic nature of the atmosphere and of the numerical model and thus to predict various plausible future scenarios. Especially the predictability of severe events is still subject of current research (e.g. Callado et al., 2013).

Within this thesis, a contribution with respect to the research topics, raised above, is provided. Regarding the physical processes involved in an extraordinary heavy precipitation event, a case study of deep moist convection that occurred at the end of September 2012, is investigated. Driven by a strongly forced synoptic situation, heavy rainfall with daily amounts, locally exceeding 200 mm, affected the Spanish Mediterranean coast. The

event is studied by means of meteorological measurement data as well as with the aid of high-resolution numerical simulations with the weather prediction model COSMO ("Consortium for Small-scale Modeling") (Schättler et al., 2012). Preconditions necessary for the initiation of deep moist convection are evaluated for the whole Spanish Mediterranean area. The available low-level moisture content, the strength of the atmospheric stability and the presence of lifting mechanisms at different meteorological scales are analyzed. The ability of the numerical model regarding an accurate short-range forecast of structure and intensity of the resulting precipitation is approached as well. Further experiments with the numerical model reveal the importance of the horizontal wind convergence and orographic lifting effects for the convection initiation during the investigated case study. The calculation of Lagrangian forward trajectories was used to determine the origin of the moisture that fed the involved precipitation systems.

A quite novel approach of how to study the predictability of the heavy precipitation event is applied. As is known, the initiation of convective cells is dependent on the synoptic-scale environment and affected by the natural variability of convective clouds (Arakawa, 2004). Based on these facts, an ensemble prediction system with two distinct sources of uncertainty was set up. On the one hand, perturbed initial conditions of the parent global model led to different large-scale situations. On the other hand, a stochastic parameterizations scheme for cumulus convection (Plant and Craig, 2008) was implemented for the nested numerical model calculations. The fraction of each source of uncertainty is varied so that mixed-scale perturbations with contributions of large- and convective-scale uncertainties between zero and one hundred percent were generated. Finally, five ensemble settings with different variability origins result. The ability to predict the studied heavy precipitation is evaluated for each ensemble by various probabilistic verification scores. As a strong synoptic forcing was present during the event, it is supposed that an ensemble with more large-scale uncertainty will outperform an ensemble consisting of more convective-scale variability. To better integrate the gained results, the same ensemble prediction system was applied for a second heavy precipitation event that occurred two weeks later in the vicinity of the first studied case. This time, the synoptic forcing was much weaker. It is thus hypothesized that an ensemble with less synoptic-scale uncertainty can successfully encompass the meteorological situation and that added small-scale uncertainty leads to a better representation of the natural variability of convective clouds.

This thesis is integrated in two large research projects. The Hydrological Cycle in Mediterranean Experiment ("HyMeX") program is an international consortium that aims to advance the scientific knowledge of the Mediterranean water cycle variability (Drobinski et al., 2014). The investigated case studies of heavy rainfall occurred during the HyMeX field campaign in autumn 2012, where additional meteorological measurements were taken in the whole western Mediterranean area. Furthermore, a subproject with focus on the Mediterranean area is included in the project "PANDOWAE" (Predictability ANd Dynamics Of Weather systems in the Atlantic-European sector), funded by the German Research Foundation. Here, the initiation, the development and the predictability of Mediterranean extreme weather is emphasized on the synoptic and the convective scale.

2 Meteorological background

In this chapter, the meteorological basics for this thesis are introduced. The focus of chapters 4, 5 and 6 of this work is the better understanding of the initiation and development of convective systems in the western Mediterranean area. Here, the necessary preconditions for the development of deep moist convection are presented. Following an introduction about a favorable synoptic-scale environment, mesoscale lifting mechanisms are described. The second part of this chapter is dealing with specific properties for severe weather in the western Mediterranean region, with focus on particular atmospheric conditions which can provoke heavy precipitation events in autumn months. After this general view, the last part of the chapter provides an overview of two specific heavy precipitation case studies. Both events led to enormous rainfall amounts in the Spanish Mediterranean region in autumn 2012. In this thesis, the initiation and the development of both heavy rainfall cases is investigated by observational and numerical model studies, including a predictability analysis by means of ensemble forecasting.

2.1 Atmospheric lifting processes

For the occurrence of precipitation, saturated airmasses are required. One common mechanism that causes saturation and following condensation is the vertical lifting of an air parcel. In the atmosphere, several effects that can result in a vertical lifting of airmasses exist. The processes differ in spatial and temporal scales. Generally it is: the larger the spatial scale, the larger the temporal scale (e.g. Oke, 2002). The largest meteorological scale is called "synoptic-scale" or "large-scale" and includes all processes with a horizontal length scale around 1000 km and more. Troughs and ridges as well as the resulting high and low pressure systems are part of the synoptic-scale. Large-scale movements can lead to vertical velocities in the order of $cm\,s^{-1}$ (e.g. Holton, 2004). The next smaller meteorological scale is the "mesoscale". It reaches from approximately 10 km to the synoptic-scale. Typical mesoscale processes in mid latitudes are frontal systems, mesoscale convective systems (MCS) and large thunderstorms. Often, orography induces mesoscale lifting processes. Vertical velocities can reach here values of two to three orders of magnitudes larger than synoptic-scale ascent movements (Stevens, 2005). The subsequent "small-scale" or "convective-scale" treats for example single convection cells, tornadoes and free convection.
Vertical ascents can occur at every meteorological scale. While temperature and vorticity differences can lead to synoptic-scale lifting, buoyant forced movements with vertical air speeds up to $10\,m\,s^{-1}$ (Houze, 1993) are responsible for convective processes. The exchange of momentum, temperature and moisture between the Earth's surface and higher

layers up to the free troposphere results. If the vertical motion reaches until the middle and higher troposphere, deep convection takes place. With moist air involved, this occurrence can lead to heavy rain, strong wind and sometimes as well to hail. Massive damages can result. Three ingredients have to be fulfilled for the release of deep moist convection and the occurrence of heavy rain (Doswell et al., 1996):

1. high moisture content in the lower troposphere

2. a conditionally unstable atmosphere

3. a trigger mechanism as source of lifting

In this section, different forms of atmospheric lifting are introduced. Suitable atmospheric conditions as well as examples of triggering mechanisms for deep moist convection are presented.

2.1.1 Large-scale lifting

In terms of spatial scale, the largest lifting mechanism is the synoptic uplift. The quantification of this process is modeled by the quasi-geostrophic ω-equation which is given in Holton (2004) as:

$$
\omega \left(\vec{\nabla}^2 + \frac{f_0^2}{\sigma} \frac{\partial^2}{\partial p^2} \right) = \frac{f_0}{\sigma} \frac{\partial}{\partial p} \left[\vec{v_g} \cdot \vec{\nabla} \left(\frac{1}{f_0} \vec{\nabla}^2 \Phi + f \right) \right]
$$

$$
+ \frac{1}{\sigma} \vec{\nabla}^2 \left[\vec{v_g} \cdot \vec{\nabla} \left(-\frac{\partial \Phi}{\partial p} \right) \right] - \frac{\kappa}{\sigma p} \vec{\nabla}^2 J \tag{2.1}
$$

$\omega = \frac{\mathrm{d}p}{\mathrm{d}t}$ denotes here the vertical velocity in a pressure (p) based coordinate system. f_0 is the Coriolis parameter. The static stability is given by $\sigma = -R\frac{T_0}{p}\frac{\mathrm{d}ln\Theta_0}{\mathrm{d}p}$ with the universal gas constant $R = 8.314\,\mathrm{J\,K^{-1}\,mol^{-1}}$ and the temperatures T_0 and Θ_0 (eq. 2.7) at level $z = 0$. $\vec{v_g}$ denotes the geostrophic wind vector, Φ the geopotential and $\kappa = \frac{R}{c_p}$ the adiabatic exponent with the specific heat at constant pressure $c_p = 1004\,\mathrm{J\,kg^{-1}\,K^{-1}}$. J is the heat rate due to radiation and latent heat release.

For the derivation of the ω-equation (e.g. Holton, 2004), the vorticity equation and the thermodynamic equation were used. This is reflected in the interpretation of the terms in eq. 2.1: The first term on the right side refers to the differential vorticity advection. In case of positive differential vorticity advection, increasing with height, upwards lifting results. This is also the case for warm air advection (second term) and for diabatic heating processes (third term). Large-scale subsidence results due to negative differential vorticity advection, increasing with height, cold air advection and diabatic cooling. The smaller σ, the more unstable the atmosphere and so the larger the resulting vertical movement. Suitable regions for synoptic lifting are areas in front of large-scale troughs and at baroclinic zones, like e.g. fronts. In terms of precipitation, large-scale lifting often leads to rain from stratiform clouds. By modifying the vertical stratification of the atmosphere,

potential instability can result due to a suitable thermodynamic structure. Rain or hail generated by deep convection is much more vigorous than rain from stratiform clouds and can be initiated by a mesoscale triggering mechanism (e.g. Doswell, 1987).

2.1.2 Preconditions for deep moist convection

Deep moist convection often produces heavy precipitation, which requires high sustained rates of condensation. The upward motion process can start with an air parcel lifted dry adiabatically (lapse rate of $\approx 10\,\mathrm{K\,km}^{-1}$). As the air ascends adiabatically, it expands and cools. An increase of the relative humidity RH by reducing the saturation water vapor pressure results. It is:

$$RH = \frac{e}{e_s} \cdot 100\% \tag{2.2}$$

with the water vapor pressure e and saturated water vapor pressure (Bolton, 1980)

$$e_s = 6.11 \cdot \exp\left(\frac{16.67\,\{T\}}{\{T\} + 243.5}\right)\,\mathrm{hPa} \tag{2.3}$$

where $\{T\}$ denotes the temperature in $^\circ$C. If the dew point temperature

$$\mathrm{T_d} = \frac{243.5\,^\circ\mathrm{C}}{\left(\frac{17.76}{\ln\left(\frac{e}{6.11\,\mathrm{hPa}}\right)}\right) - 1} \tag{2.4}$$

is reached by an adiabatic ascent, condensation - and so the formation of a cloud base - occurs. This level is called lifted condensation level (LCL). During a further lifting, the air parcel rises with the saturated adiabatic lapse rate. Through latent heat release, this value is smaller than the dry adiabatic lapse rate. If the air parcel is getting warmer than the surrounding atmosphere and rises upwards freely, the level of free convection (LFC) is reached. In a case with only free convection, the air parcel is lifted saturated adiabatically until the convective condensation level (CCL). From LFC or CCL, the air parcel ascends further pseudo adiabatically due to its own buoyancy. When its temperature is equal to the environment, the equilibrium level (EL) is reached.

Several convective indices exist to characterize the possibility for deep convection (e.g. Groenemeijer, 2009 or Kunz, 2007). As first example, the convective available potential energy (CAPE) is introduced. The CAPE is a measure of how much potential energy is available between the LFC or the CCL and the EL. This energy can be transposed into kinetic energy, which is used for the convective updraft. The computation of CAPE is performed via (e.g. Markowski and Richardson, 2010):

$$\text{CAPE} = \int_{\text{LFC,CCL}}^{\text{EL}} g \frac{T_p - T_e}{T_e} \mathrm{d}z \tag{2.5}$$

with the temperature T_p of the air parcel and environmental temperature T_e. The unit of the CAPE is given in $\mathrm{J\,kg^{-1}}$. Typical CAPE values for moderate convection lie between $500\,\mathrm{J\,kg^{-1}}$ and $1000\,\mathrm{J\,kg^{-1}}$. Beneath, only weak convection is possible; above, the convection is likely to be strong. The LFC or the CCL are reached if the air parcel could overcome the convective inhibition (CIN) (e.g. Markowski and Richardson, 2010). Both parameters can be visualized graphically in thermodynamic diagrams, like the Stüve diagram.

A measure, which takes into account the temperature stratification and the humidity of the atmosphere, is the equivalent potential temperature Θ_e (Rossby, 1932). This is the temperature which would be reached if all water in the air parcel was condensed, all latent heat was released and the parcel was brought adiabatically to $1000\,\mathrm{hPa}$. In a stable atmosphere, Θ_e increases with height. If $\frac{\mathrm{d}\Theta_e}{\mathrm{d}z} < 0$, a saturated atmosphere is called unstable (e.g. Houze, 1993, Emanuel, 1994 or Markowski and Richardson, 2010). As the atmosphere is usually moist, but unsaturated, $\frac{\mathrm{d}\Theta_e}{\mathrm{d}z} < 0$ denotes a so called potential instability. By bringing the moist airmass to its saturation level (e.g. by a lifting mechanism), a convectively unstable layer results. With a vertical profile of Θ_e, a graphical visualization of the atmospheric stability and so for the risk of convection, can be provided.
To calculate Θ_e, several other meteorological parameters have to be used: the latent heat of vaporization $L_c = 2.501 \cdot 10^6 \,\mathrm{J\,kg^{-1}}$, the saturation mixing ratio

$$r_s \approx 0.622 \cdot \frac{e_s}{p - e_s} \tag{2.6}$$

and the potential temperature

$$\Theta_0 = T_0 \left(\frac{p_0}{p} \right)^{\frac{R}{c_p}} \tag{2.7}$$

Through the international standard atmosphere (U.S. Government Printing Office, 1976) the normal surface pressure value in mid latitudes is given by $p_0 = 1013.25\,\mathrm{hPa}$.
In this work, an approximation for Θ_e is used after Holton (2004):

$$\Theta_e \approx \Theta \exp \left(\frac{L_c q_s}{c_p T} \right) \tag{2.8}$$

Freezing and melting processes in the air parcel are neglected in this simplified equation. Further forms for the calculation of Θ_e can be found in Bolton (1980) and in Davies-Jones (2009).

2.1.3 Mesoscale and small-scale lifting mechanisms

Orographic lifting

Over a horizontal non-homogeneous area, including mountainous regions, particular mesoscale processes can lead to rising airmasses. Due to a deceleration of the flow and a resulting lifting mechanism, convection can be released at the surroundings of an orographic formation. Whether this process happens is determined by the Froude number Fr, which is dependent on the wind speed U, the Brunt-Väisälä frequency $N = \sqrt{\frac{g}{\Theta}\frac{\mathrm{d}\Theta}{\mathrm{d}z}}$ and the mountain height H. After e.g. Barry (2008) it follows:

$$Fr = \frac{U}{NH} \tag{2.9}$$

If $Fr > 1$, the flow is called supercritical. Then, the air thickens vertically and slows while its ascent over a barrier (e.g. Smith, 1979, Houze, 1993 or Holton, 2004). This situation is called orographic blocking (e.g. Roe, 2005 or Markowski and Richardson, 2010). With low atmospheric stability, thus small values of N, this situation is often reached for strong wind velocities (Stull, 1988). Favorable regions for orographically induced deep moist convection are given at coastal mountainous areas, when moist air is transported towards the land (e.g. by sea breeze). The Mediterranean basin is such a suitable area. Several events of orographically induced heavy precipitation were investigated for that region (sec. 2.2). But also in non-coastal areas, the convection initiation over complex terrain is topic of several research projects. Results from the "COPS" (Convective and Orographically-induced Precipitation Study) project, which took place over the black forest, are presented e.g. in Kottmeier et al. (2008), Kalthoff et al. (2009) or Corsmeier et al. (2011).

Horizontal wind convergence

Horizontal convergence can be triggered for example by an interaction of the flow with orography. This was often observed during the mentioned COPS campaign. But also synoptically induced convergence zones, e.g. in cyclones or in the transition zone between high and low pressure systems, are common. Examples in which horizontal wind convergence led to deep moist convection in the Mediterranean area are presented in section 2.2. Often, the convergence area is formed in a relatively sharp zone, which is then called convergence line. Mathematically, the divergence of the horizontal wind $\vec{v_h}$ is defined by:

$$\nabla \cdot \vec{v_h} = \frac{\partial u}{\partial x} + \frac{\partial v}{\partial y} \tag{2.10}$$

Convergence means a negative divergence: $\nabla \cdot \vec{v_h} < 0$. Taking into account the moisture in the air, the so called moisture flux convergence (MFC) can be computed after e.g. Banacos and Schultz (2005) by:

$$\text{MFC} = -\nabla \cdot (q\vec{v_h}) = -\vec{v_h} \cdot \nabla q - q\nabla \cdot \vec{v_h} \tag{2.11}$$

q denotes the specific humidity, which is given by:

$$q = \frac{\frac{M_w}{M_d} \cdot e}{p - \left(1 - \frac{M_w}{M_d}\right) \cdot e} \approx 0.622 \cdot \frac{e}{p} \tag{2.12}$$

with M_w = molar mass of water = $18.01528\,\text{g mol}^{-1}$ and M_d = molar mass of dry air = $28.9644\,\text{g mol}^{-1}$.

The vertically integrated MFC is a measure for the prediction of synoptically forced rainfall amount. In several numerical weather prediction models, the MFC is used as closure assumption in the cumulus convection parameterization scheme (sec. 3.1.4). In nowcasting weather prediction methods (up to 3 h), the MFC is used to forecast convective initiation and especially its favorable spatial distribution (Banacos and Schultz, 2005).

Mesoscale convective systems

In the case that small- or mesoscale lifting processes are embedded in an area where synoptic-scale lifting is present, this can lead to a particularly deep and intense development of widespread convection. With high CAPE values and strong vertical wind shear (i.e. rate of wind change with height) over a large region, several neighboring convection cells can develop. If the mesoscale formation of convective cells is aligned along a line in such a way that the inflow and outflow are organized and stable as far as CAPE and low-level wind shear is available, such a formation is called a "squall line". During the decay of a convective cell, precipitation leads to cooling by evaporation at lower levels. The gusts at the leading edge of the developing cold pool can help to initiate new convection (e.g. Stevens, 2005 or Corsmeier et al., 2011). So called mesoscale convective systems can include squall lines and mesoscale convective complexes and can have a life span exceeding 12 h (Maddox, 1980). The spatial extent of a MCS can reach a few hundred kilometers (Houze, 1993). A case study in which the triggering of a MCS over West Africa was linked to the superposition of two convergence zones is investigated in Klüpfel et al. (2012).
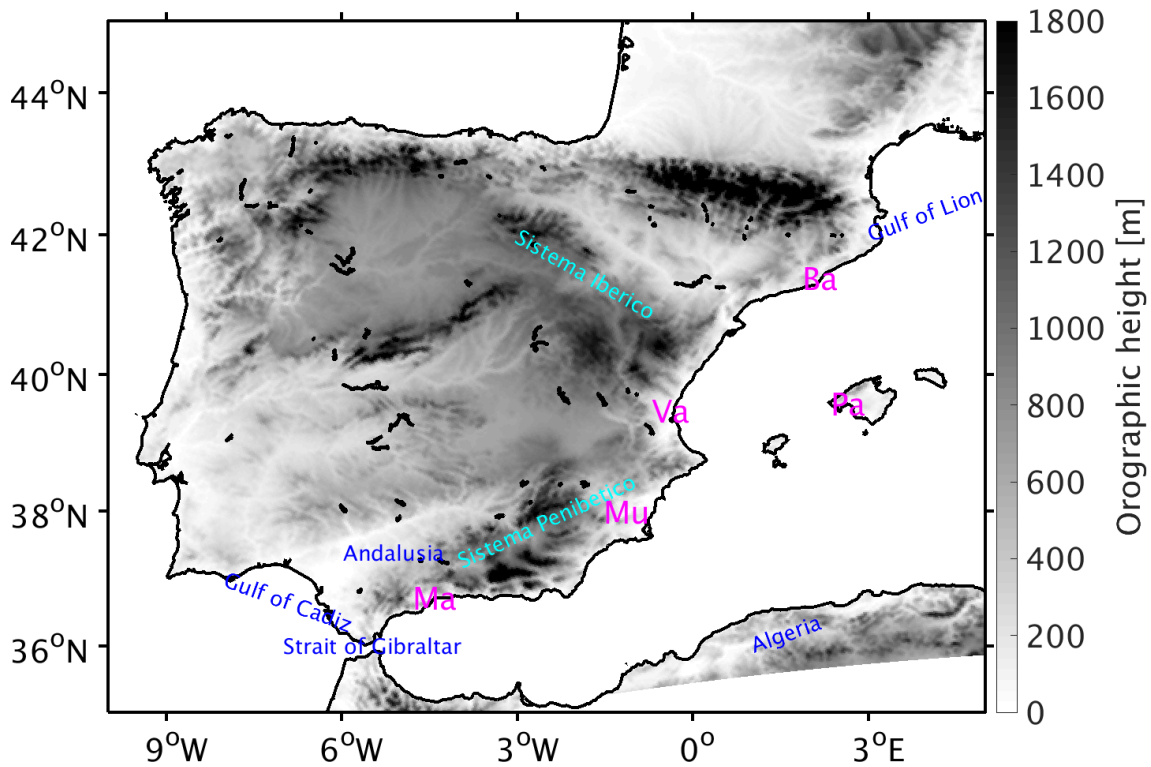
Figure 2.1: Orography of the western Mediterranean area. For a better visibility, the colorbar was chosen to end at 1800 m height, even if in the Pyrenees and in the mountainous areas in southern Spain, heights of around 3000 m are reached. Added are important cities (magenta) and geographical features (blue and cyan). The specified cities are: Malaga (Ma), Murcia (Mu), Valencia (Va), Palma de Mallorca (Pa) and Barcelona (Ba).

2.2 Severe weather in the western Mediterranean area

According to the Köppen-Geiger climate classification system, the western Mediterranean area is situated climatically in the regions Csa and Csb. "C" stands for warm temperate climates with an averaged monthly temperature above 10°C in the summer months; "s" characterizes the precipitation pattern as dry summers, where during the driest summer month less than 40 mm of average precipitation occur. The letters "a" and "b" denote the degree of summer temperatures. In both cases at least four months have to have an average temperature of more than 10°C (Kottek et al., 2006 and Lionello, 2012). Being located in such a dry-summer climate, the Mediterranean Sea can be warmed up during the summer season. Especially in autumn, the available source of warm and moist air can then be used to feed precipitation systems.

Besides, the Mediterranean basin is surrounded by a complex orography. In Spain, different mountain ranges like the "Sistema Iberico" and the "Sistema Penibetico" (Fig. 2.1) as well as the Pyrenees and the topography of the Balearic Islands can interact with the atmospheric flow. In France, the Pyrenees, the Massif Central, the western part of the Alps and

the Corsican Island are favorable for orographic lifting processes. In Italy, the Alps and the Sardinian and Sicilian Islands are the main topographic elevations. At the southern coast of the western Mediterranean, the Atlas mountains can deform the atmospheric flow.

The remarkable land-sea contrast and the reservoir of heat and moisture can favor the initiation of heavy precipitation events. The location and intensity of those events is dependent on large-scale upper-level atmospheric conditions as well as on low-level thermodynamical processes. A classification of atmospheric patterns leading to heavy rain in the western Mediterranean region is given by Martinez et al. (2008). More than seven years of high impact weather data are analyzed with the help of the MEDEX database (Jansà et al., 2014b). The same database was used in Fita et al. (2006) to study the impacts and interactions of baroclinic and diabatic factors on the cyclogenesis in the Mediterranean area. Cyclonic systems can organize the advection of warm and humid air at low levels in order to transport it from the Mediterranean Sea into the affected area. The so produced large potential instability can be released by lifting and deep moist convection can occur. Thus, it is favorable for the initiation of deep moist convection if a cyclone center - which does not have to be very intense - is located in the vicinity. For the Mediterranean region, Pfahl and Wernli (2012) found a frequency of more than 80% of precipitation extremes correlated with cyclones. Similar high correlations between cyclones and heavy precipitation are found in Jansà et al. (2001), Campins et al. (2006) and Campins et al. (2007). To understand where cyclones are initiated frequently, Homar et al. (2007), Garcies and Homar (2009), Garcies and Homar (2010) and Campins et al. (2011) investigated sensitive regions within the ERA40 reanalysis dataset (Uppala et al., 2005). The results from these studies especially highlight areas in the Mediterranean Sea, over the North Atlantic Ocean and in North Africa. Climatological studies for heavy precipitation events in the Spanish and French Mediterranean regions were conducted by Romero et al. (1999) and Ricard et al. (2012). One study based on observational data is presented by Tuduri and Ramis (1997). The analysis of more than 300 convective events in the western Mediterranean revealed that heavy rain events occurred mainly with warm and humid air in the troposphere and warm air advection at low levels. In Mehta and Yang (2008), a climatology of 10 years of satellite derived rainfall measurements showed 20% more precipitation over the western Mediterranean Sea than over its eastern part. The mountainous regions were found as hotspots within the studies dataset. Ramis et al. (2013) analyzed several decades of the measurements of more than 8000 raingauges in Spain. Most extreme rainfall occurred in the Mediterranean coastlands with a pronounced hotspot around Valencia. The investigation of associated typical meteorological situation revealed the importance of a low pressure system over North Africa and high pressure over central Europe. The resulting warm and moist easterly flow over the Mediterranean Sea favors the advection of conditionally unstable air towards the eastern coast of Spain. For long-lasting rainfalls, a cold deep mid-tropospheric trough to the west or southwest of the Iberian Peninsula and a ridge over central Europe were found to bring stationarity to the meteorological situation and enhance the low-level easterly circulation.

In the climatological studies, mentioned above, many investigations of single case studies of heavy precipitation events in the western Mediterranean area are integrated. The influence of the synoptic scale is often found as crucial. An upper-level trough, located

southwesterly of the Mediterranean provided suitable large-scale conditions for the development of heavy precipitation in the case studies by Homar and Stensrud (2004), Fresnay et al. (2012), Lenz et al. (2012), Romero et al. (2014) or Rysman et al. (2015). Cut-off low characteristics were present in events studied by Romero et al. (2000), Homar et al. (2002) and Cohuet et al. (2011).

Mesoscale features to enhance the conditions for heavy rainfall were often given by surface lows. This is in agreement with the above cited climatological studies about the importance of cyclones. Case studies are presented in Doswell et al. (1998), Romero et al. (2000), Romero (2001), Homar and Stensrud (2004), Lenz et al. (2012) and Romero et al. (2014). A case study in which the Mediterranean cyclone was linked to a former Hurricane is given by Grams et al. (2011). An example of an orographically induced cyclone is shown in Horvath et al. (2006), where cyclogenesis took place in the lee of the Atlas mountains. Sometimes, cyclones in the Mediterranean can develop into hurricane-like structures. Favorable meteorological environments for those so called "Medicanes" are investigated in Tous and Romero (2012). High mid-tropospheric humidity, diabatic contributions to surface Θ_e and low tropospheric wind shear were found as suitable preconditions for the development of Medicanes. Two case study examples are given in Pytharoulis et al. (2000) and Chaboureau et al. (2012). The interactions of aerosols, clouds and dynamics in a Medicane are addressed in Kraut (2015). Besides the low pressure systems, also low-level jets (Buzzi and Foschini, 2000, Romero et al., 2000 or Homar et al., 2002), cold pool dynamics (Bresson et al., 2009) or convergence zones (e.g. Pascual and Callado, 2002, Pascual et al., 2004, Khodayar et al., 2015 or Rysman et al., 2015) are typical mesoscale features linked to heavy rainfall in the western Mediterranean. Often, convective cells are organized in mesoscale convective systems. Examples are given in Romero et al. (2000), Delrieu et al. (2005), Vie et al. (2011) and Fresnay et al. (2012). Squall lines were observed by Ramis et al. (2009), Cohuet et al. (2011) and Romero et al. (2014).

Very prominent on the initiation of heavy precipitation is the role of the Mediterranean orography. Studies from Doswell et al. (1998), Buzzi and Foschini (2000), Romero et al. (2000), Pascual et al. (2004), Bresson et al. (2009), Cohuet et al. (2011), Barthlott et al. (2014), Romero et al. (2014), Adler et al. (2015) and Khodayar et al. (2015) revealed orographic lifting effects at various coastal Mediterranean elevations. An event with only weak orographic influence is evaluated in Homar et al. (1999).

Although the evaporation from the Mediterranean Sea is usually a major source to feed the convection systems, also cases with moisture sources from outside the Mediterranean area are reported. In Reale et al. (2001), Duffourg and Ducrocq (2011) and Duffourg and Ducrocq (2013), moisture sources from the Atlantic Ocean and from African regions are investigated regarding their effects on precipitation and floods in the Mediterranean region.

Regarding the future perspective, a trend for increasing heavy precipitation is expected due to global warming in the Mediterranean area (Alpert et al., 2002). Sanchez et al. (2004) stated this fact especially for summer and early autumn - precisely the seasons in which most heavy rainfall events occur. A study that examines the risk of Medicanes in a changing climate is given by Romero and Emanuel (2013). With a high population density in coastal Mediterranean regions (Lionello, 2006), these areas are also in future

especially exposed to hazards. Thus, the Mediterranean area is highly vulnerable to climate change (Giorgi, 2006 and Giorgi and Lionello, 2008).

This is one important reason to improve the predictability of Mediterranean heavy precipitation events. Regarding the uncertainty of large-scale conditions in the numerical weather prediction, studies were executed by Homar et al. (2002), Homar et al. (2006b), Vich et al. (2011), Vie et al. (2011), Hally et al. (2014) and Amengual et al. (2015). Whether and where more meteorological observations could help to better predict heavy rainfall events is studied in Homar et al. (2006a) and Campins et al. (2013). The impact of parameterizations for cloud physics and turbulence in weather prediction models is investigated in Fresnay et al. (2012) and Hally et al. (2014).

In summary it can be concluded that the mesoscale and synoptic-scale ingredients, leading to high precipitation amounts in the western Mediterranean region, are diverse. Complex interactions of synoptic upper-level steering flow, mesoscale lifting mechanisms and local topographic barriers complicate the comprehension of the formation of heavy rainfall. Thus, it remains a challenge for numerical weather forecast models to provide a proper prediction of heavy precipitation events in the Mediterranean region.

2.2.1 The HyMeX measurement campaign

The HyMeX program is a concerted effort at the international level that aims to advance the scientific knowledge of the atmospheric water cycle variability based on observations and comparing model calculations (Drobinski et al., 2014). HyMeX is split up into four kinds of measurement periods: a long-term observation period, two enhanced observation periods and two special operation periods (SOPs). The first SOP (SOP1) took place during nine weeks from 5 September to 6 November 2012. During these nine weeks about 20 intense weather events were investigated as intense observation periods (IOPs) (Ducrocq et al., 2014).

Data from various meteorological measurement systems were gained in the whole western Mediterranean area. In addition to the existing measurement systems, like satellites, stationary radar systems, surface weather stations and raingauges, extra measurements were performed at several so called "super sites" in the western Mediterranean area. In Spain, additional measurement systems were installed around Valencia, at the Balearic Islands and in Catalonia (Quintana et al., 2012). In France, the two regions Cévennes-Vivarais and Corsica (Lambert et al., 2011) stand in the foreground. In Italy, the Liguria-Tuscany, northeastern Italy and Central Italy were covered with extra measurements during the field campaign. All measurement data from HyMeX are collected in a database[1]. For this work, raingauges data, data from surface weather stations, radiosoundings and output from radar and satellite systems are used for the description and the validation of experiments with numerical weather prediction models of both heavy precipitation events.

---

[1] http://mistrals.sedoo.fr/HyMeX/

2.2.2 HyMeX IOP8 - a synoptically strongly forced event

Chosen for this discussion is a heavy precipitation event which occurred on the 28 and 29 September 2012 in the western Mediterranean area. Especially the Spanish Mediterranean coast was affected on the 28 September by heavy rain. After Jansà et al. (2014a), this was the most significant situation which affected areas of Spain during HyMeX SOP1. The working title of the observation period in which the strong rainfalls were measured, is "HyMeX IOP8". This name will be used as well in the following.

The synoptic preconditions of HyMeX IOP8 are based on a long wave trough which established on 25 September 2012 west of Europe above the North-East Atlantic. On 27 September a cut-off process started west of Portugal, which was completed at 1800 UTC (Fig. 2.2, top left). In front of the cut-off low a corresponding surface low (Figure 2.2, top left, white isolines) developed due to uplift in 500 hPa (Fig. 2.2, middle left), warm air advection in lower levels (Fig. 2.2, middle right) and a strong horizontal divergence located at 300 hPa. The surface low forced a transport of warm and moist air at lower levels to the southeast of the Iberian Peninsula. Therefore, the atmosphere became more and more unstable (shown later in Fig. 6.3 in section 6.2). At 1800 UTC on 28 September the cut-off low was located over the southern part of the Iberian Peninsula, over the Strait of Gibraltar (Fig. 2.2, top right).

East of the cut-off low, large-scale uplift and a vertical stretching - due to a strong advection of warm and moist air at 850 hPa from North Africa into the southern Spanish region - occurred. Due to this large-scale stretching, a release of latent heat energy by condensation of water vapor in lower levels and a cooling of drier air masses in higher levels led to a potential instability (sec. 2.1.2) of the atmosphere. For the initiation of convection in a potentially unstable situation, a trigger mechanism is needed. In this case, it was given by a horizontal divergence and a positive vorticity advection at 300 hPa (not shown) leading to a ground-level wind convergence where air masses converged from the central and northern Mediterranean at the Gulf of Cadiz. This scenario is typical for the eastern Spanish region during late summer (see references in sec. 2.2).

In the course of the next hours, the cut-off low and the corresponding surface low moved along the Spanish coast to the northeast. The surface low is estimated to be persistently located at nearly 100 km north-eastwards of the cut-off low in the 500 hPa level. On 30 September the cut-off low vanished (not shown).

In the night to 28 September 2012, first orographic induced precipitation occurred in the southern Spanish mainland between Gibraltar and Malaga. This precipitation was quasi stationary for several hours and was only shifted slowly eastwards during the next few hours. At 1200 UTC, significant rainfall amounts occurred. This was due to continuous evaporation from the Mediterranean and advection of moist and warm air masses: first from the Atlantic and from the Mediterranean to southern Spain and finally only from the Mediterranean to south-eastern Spain. The uptake regions of the humidity are discussed in detail in section 6.4. At stations near Murcia and Alicante, more than $50 \, \text{mm} \, \text{h}^{-1}$ of precipitation were measured. In Amengual et al. (2015), the extreme flash flood in Murcia is studied by a hydrological runoff model. From 28 September 0600 UTC until 29 September 0600 UTC, the precipitation led regionally to a 24-hourly accumulated precipitation

amount up to 200 mm (Fig. 2.2, bottom left). Also near Malaga, precipitation maxima with values up to $80\,\mathrm{mm\,h^{-1}}$ were measured. The related strong convection can also be seen by the high level clouds in the satellite image from 28 September at 1200 UTC. At this time step, a MCS (see section 2.1.3) with a V-shaped cloud structure (indicated by the white arrow in Figure 2.2, bottom right) had developed over the southern Spanish Mediterranean coast. This structure can be linked to an overshooting top (e.g. Houze, 1993), that often occurs in warm subtropical or tropical maritime air masses which can store a large amount of water vapor. In Andalusia and Murcia (southern Spain), rainfall caused 120 million Euro damage (Jansà et al., 2014a). Thirteen people lost their lives in Andalusia and Murcia. A tornado was registered in Gandia (Valencia) (Ducrocq et al., 2014). The rainfall reported in central Spain mainly developed in stratiform clouds and ranged up to 100 mm per 24 h.

Based on the large amount of available meteorological measurement data, Khodayar et al. (2015) performed a detailed study of this case. Humidity measurements by Global Positioning System (GPS) data, raingauges, surface weather stations, lightning sensors and radiosoundings were used in that study to investigate the temporal and spatial variability of water vapor. Additionally, several mesoscale convergence zones were detected over land. High uncertainty was present for the processes over the Mediterranean Sea. At this point, this thesis improves the knowledge about HyMeX IOP8. With numerical model studies and the integration of remote sensing information, continuative investigations are presented in chapters 4, 5 and 6.
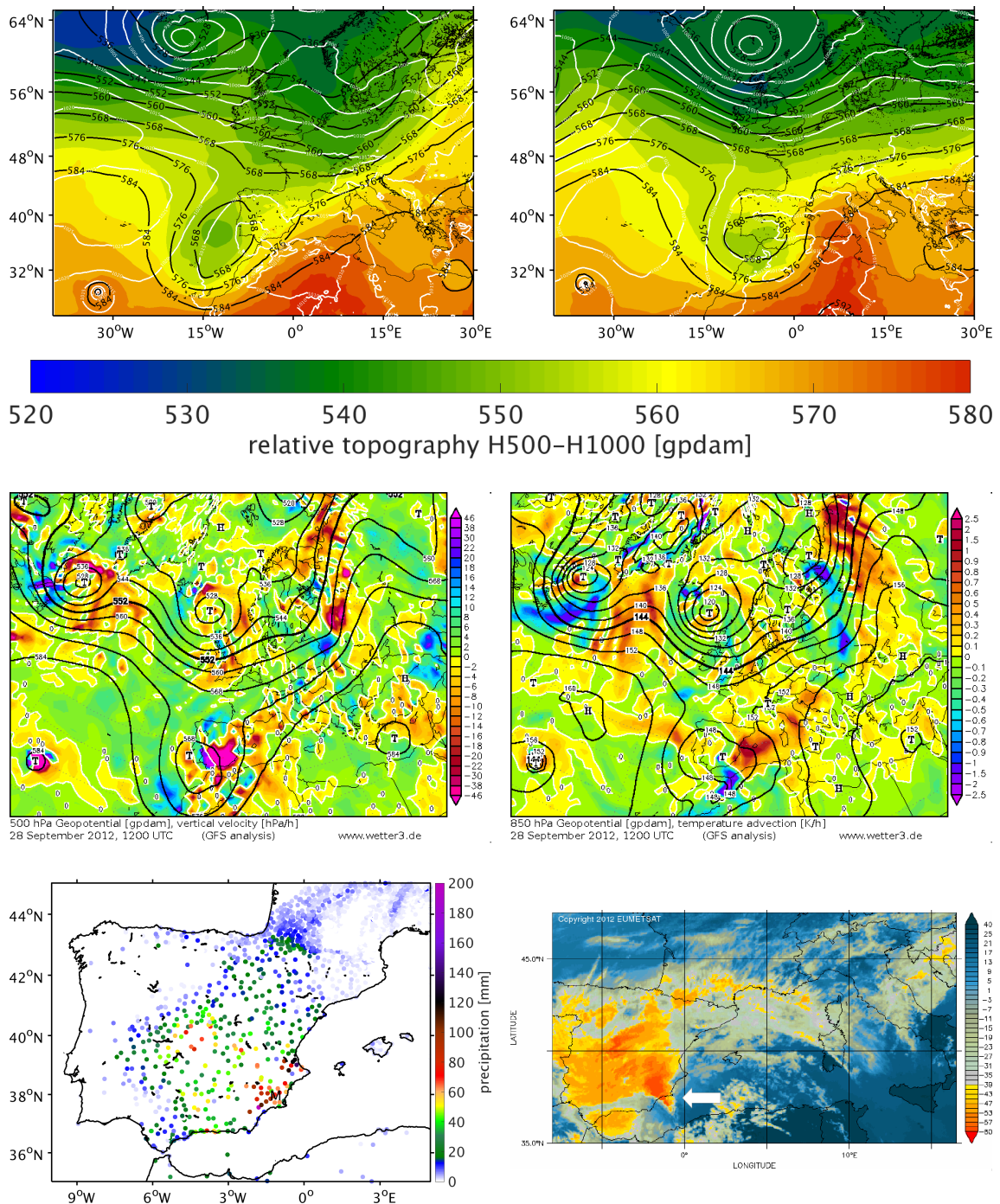
Figure 2.2: Top: Geopotential at 500 hPa (black contour lines), surface pressure (white contour lines) and relative topography between 500 hPa and 1000 hPa (color shaded) on 27 September 2012 at 1800 UTC (left) and on 28 September at 1800 UTC (right). Data basis: IFS analysis data (Barros et al., 1995) with a spatial horizontal resolution of 0.25°. Middle left: Geopotential (black contour lines) and vertical velocity (color shaded) in 500 hPa on 28 September at 1200 UTC. Middle right: Geopotential (black contour lines) and temperature advection (color shaded) in 850 hPa on 28 September at 1200 UTC. Courtesy of `www.wetter3.de`. Bottom left: Observed 24-hourly rainfall amount from 28 September 2012 at 0600 UTC to 29 September 2012 at 0600 UTC. Bottom right: 10.8 μm infrared brightness temperature in °C from MSG on 28 September 2012, 1200 UTC. Courtesy of EUMETSAT. The MCS with a V-shaped cloud structure is indicated by a white arrow.

15

2.2.3 HyMeX IOP12b - a synoptically weakly forced event

The second case study, which was selected for this work, is "HyMeX IOP12b". At 12 October 2012, heavy precipitation of partly more than $100\,\mathrm{mm}\,24\mathrm{h}^{-1}$ occurred in the areas of Valencia, Catalonia and the Balearic Islands (Fig. 2.3, bottom left). This was due to a very well organized MCS (Fig. 2.3, bottom right) embedded in a weak synoptic forcing. On 11 October at 1800 UTC, two prominent low pressure systems were located west from Iceland and over western Russia (Fig. 2.3, top left). In between, a steep ridge arched upward. Over Spain and the western Mediterranean area, the geopotential field at $500\,\mathrm{hPa}$ showed a weak zonal flow. A short-wave trough was located over the North-East Atlantic Ocean, nearby the Portuguese coast. 24 h later, the situation did not change much (Fig. 2.3, top right). With the zonal flow over the Mediterranean area and a new short-wave trough west of the Strait of Gibraltar, only a weak synoptic forcing was present. This is also visible by relatively low uplift values in $500\,\mathrm{hPa}$ (Fig. 2.3, middle left) and almost no warm air advection in $850\,\mathrm{hPa}$ (Fig. 2.3, middle right).

At lower levels, a horizontal wind convergence developed between a low and a high pressure system. On 11 October at 1800 UTC, both airmasses converged over central Spain. During the following hours, the convergence zone moved towards the Mediterranean Sea. On 12 October, 1800 UTC, the convergence line was located between southern Spain and the Balearic Islands. The corresponding surface pressure distribution shows lower values in the North and higher values in the South (Fig. 2.3, top right, white isolines). Similar to HyMeX IOP8, the interaction of convergence line and the warm sea surface temperatures led to the release of potential instability and consequently to deep convection. Organized cells clustered together in a MCS. On 12 October around noon, the convective system near the Balearic Islands was most active (Rysman et al., 2015). This system remained almost stationary for about 15 h. Almost all precipitation amount registered during IOP12b on 12 October 2012 was linked to the MCS over the Balearic Islands. Between 1000 UTC and 1500 UTC, more than 100 mm were measured in a Majorcan station. The summit of the heavy precipitation event can be fixed between 1100 UTC and 1300 UTC. Further significant rainfall amounts could be measured between 1600 UTC and 1900 UTC in regions near Valencia (over 100 mm as stated in Jansà et al., 2014a) and Barcelona (over 50 mm). Due to the heavy precipitation, flooding events occurred in Mallorca. Several flights had to be deviated from Palma to other destinations. Strong wind velocities of more than $100\,\mathrm{km}\,\mathrm{h}^{-1}$ were measured in Mallorca as well (Jansà et al., 2014a and Rysman et al., 2015).
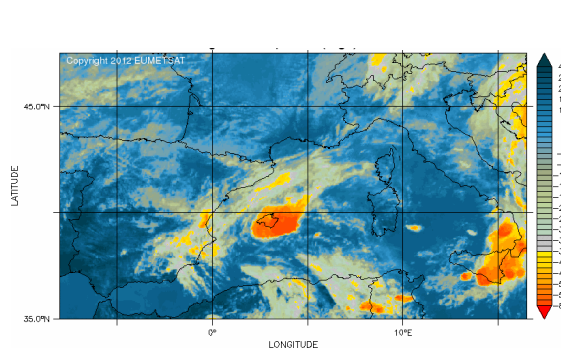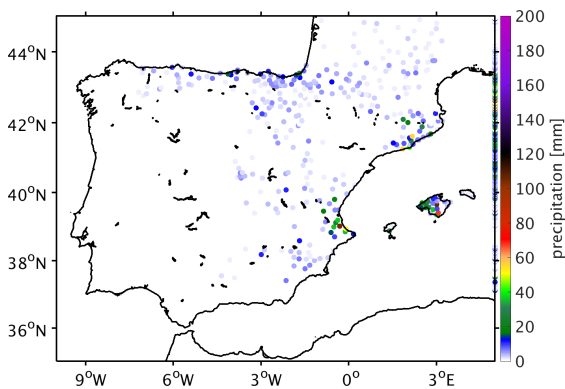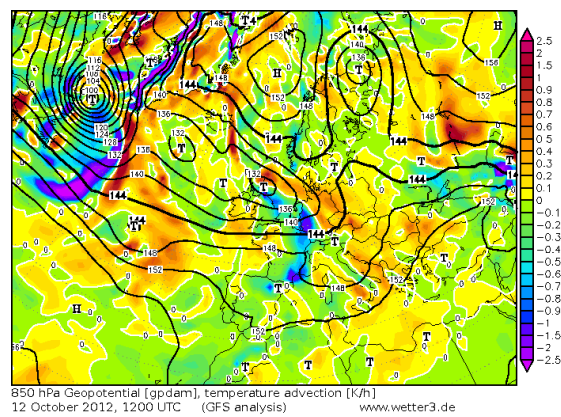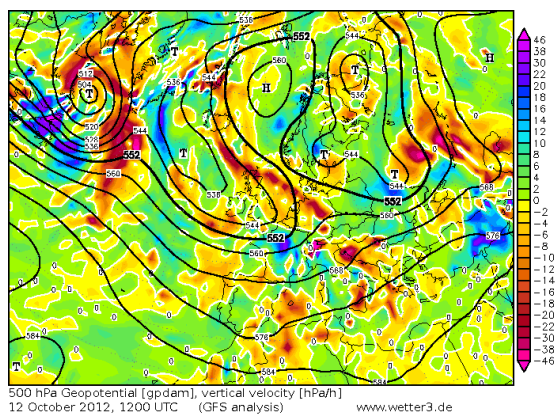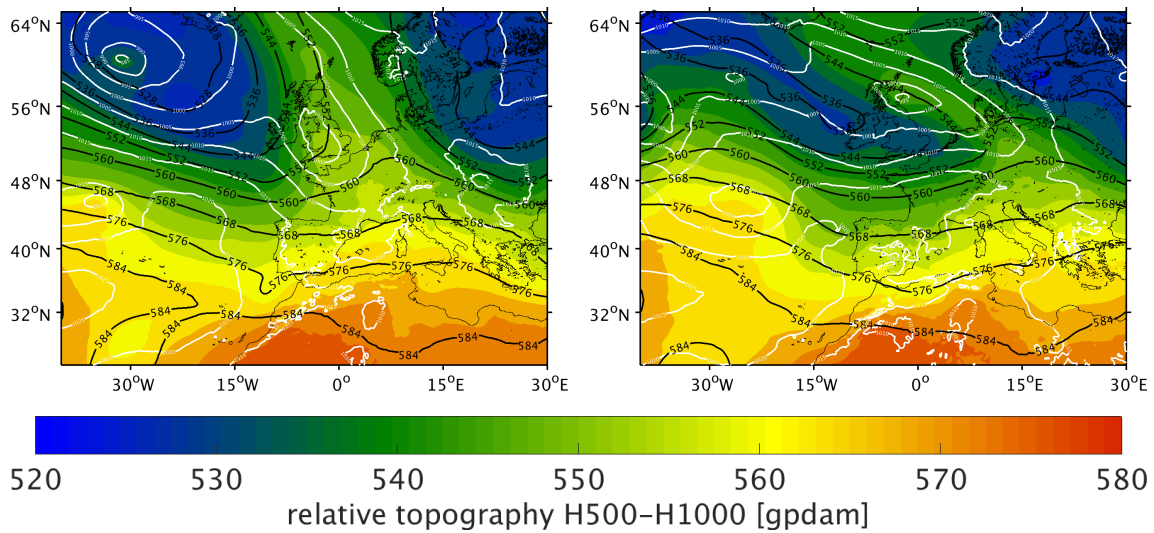
Figure 2.3: Top: Geopotential at 500 hPa (black contour lines), surface pressure (white contour lines) and relative topography between 500 hPa and 1000 hPa (color shaded) on 11 October 2012 at 1800 UTC (left) and on 12 October 2012 at 1800 UTC (right). Data basis: IFS analysis data (Barros et al., 1995) with a spatial horizontal resolution of 0.25°. Middle left: Geopotential (black contour lines) and vertical velocity (color shaded) in 500 hPa on 12 October at 1200 UTC. Middle right: Geopotential (black contour lines) and temperature advection (color shaded) in 850 hPa on 12 October at 1200 UTC. Courtesy of www.wetter3.de. Bottom left: Observed 24-hourly rainfall amount from 12 October 2012 at 0000 UTC to 13 October 2012 at 0000 UTC. Bottom right: 10.8 µm infrared brightness temperature in °C from MSG on 12 October 2012, 1400 UTC. Courtesy of EUMETSAT.

17

3 Numerical weather prediction and forecast validation

A numerical weather prediction (NWP) model is a suite of computational codes and algorithms to solve numerically the fundamental differential equations that model the physical processes in the atmosphere with the aim to forecast various meteorological variables. The first thoughts of a NWP were made by Vilhelm Bjerknes in 1904. He noted in his publication (Bjerknes, 1904) that a future atmospheric state is dependent of the initial state of the atmosphere as well as of known boundary conditions.

In this chapter, the COSMO model (Schättler et al., 2012) is introduced. It is used for a detailed diagnostic study of the investigated case study HyMeX IOP8 (sec. 2.2.2) and for a predictability study - realized by ensemble forecasts - of HyMeX IOP8 and HyMeX IOP12b (sec. 2.2.3). The physical equations of the numerical model are introduced in detail. Further focuses are put on the importance of initial and boundary conditions, the ensemble forecast mode and the parameterizations of deep moist convection. Further numerical tools like the "Application of Research to Operations at Mesoscale" (AROME) western Mediterranean (WMED) model and the trajectory calculation tool Lagranto are presented. The third part of the chapter deals with several verification scores which were used to verify the output of the performed COSMO simulations with respect to measurement data and to AROME-WMED data. Beginning with traditional scores for continuous and dichotomous variables, spatial verification scores and special probabilistic verification scores are introduced.

3.1 The COSMO model

The COSMO model is a non-hydrostatic and fully compressible NWP model which was designed for weather forecasting in a limited area. The model is based on the "Lokal-Modell" (Steppeler et al., 2003), which was developed by the German Meteorological Service (DWD). For this work, COSMO was used in version 4.26, described in Schättler et al. (2012).

3.1.1 Basic prognostic equations and model grid

To predict a future atmospheric state evolved from a given atmospheric state with moist air, the seven meteorological variables of wind velocity $\vec{v} = (u, v, w)$, density ρ, pressure p, temperature T and specific humidity q have to be known. The temporal deviation

of these variables are given by five coupled partial differential equations and are based on various conservation laws. These prognostic equations, which are introduced in the following, have to be solved numerically.

Equations of motion

To predict the wind vector, the equations of motion are used. They describe the conservation of momentum in the atmosphere. With gravity acceleration $\vec{g}$, angular velocity of earth rotation Ω and stress tensor $\vec{\tau}$, the equations of motion are given by:

$$\rho \frac{\mathrm{d}\vec{v}}{\mathrm{d}t} = -\nabla p + \vec{g}\rho - 2\Omega \times (\rho\vec{v}) - \nabla\vec{\tau} \tag{3.1}$$

In the so presented notation, it follows directly that pressure gradient force, gravitational force, Coriolis force and friction forces are responsible for temporal velocity changes in the atmosphere.

Continuity equation

To describe the conservation of mass in NWP systems, the continuity equation is used. It is given by:

$$\frac{\partial \rho}{\partial t} + \nabla \cdot (\rho\vec{v}) = 0 \tag{3.2}$$

Thus, the total temporal deviation of ρ, given by the local temporal deviation plus an advection term, is zero. In the COSMO model, the continuity equation is replaced by an equation for the time dependent pressure deviation $p' = p - p_0(z)$, where $p_0(z)$ is the pressure of a reference atmosphere. More details can be found in Steppeler et al. (2003) and in Schättler et al. (2012).

Prognostic equation for temperature

To capture the thermodynamical processes, the prognostic equation for the temperature is used:

$$\frac{\partial T}{\partial t} + \vec{v} \cdot \nabla T = -\frac{p}{\rho c_{vd}} \nabla \cdot \vec{v} + Q_T \tag{3.3}$$

c_{vd} is the specific heat capacity at constant volume and Q_T describes diabatic heating through evaporation and radiation. This equation follows from the first law of thermodynamics, which describes the conservation of energy (e.g. Kalnay (2003)).

Prognostic equation for humidity

As the atmosphere consists of dry air, water vapor, liquid water and water in solid state, the prognostic equations for the humidity quantities have to be considered as well:

$$\frac{\partial q^x}{\partial t} + \vec{v} \cdot \nabla q^x = -\nabla \cdot J^x + I^x \tag{3.4}$$

with $x = (d_{(dry)}, v_{(vapor)}, l_{(liquid)}, f_{(frozen)})$. J^x denotes here the diffusion flux and I^x the sources and sinks of moisture.

Diagnostic equation of state

With a prognostic equation for pressure, the density is derived by the ideal gas law:

$$\rho = \frac{p}{R_d \left(1 + \left(\frac{R_v}{R_d} - 1\right) q^v - q^l - q^f \right) T} \tag{3.5}$$

Modification of COSMO coordinate system

To adapt the basic equations 3.1, 3.2, 3.3 and 3.4 to the geometry of the Earth, three main modifications are applied. First, the whole coordinate system is rotated so that the new model equator is centered in the model domain. With this technique, the coordinate system can be assumed to be approximately orthogonal for small model domains. For the second modification, the equations are transformed to a spherical coordinate system spanned with the geographical longitude λ, the geographical latitude φ and the distance from the Earth's center r. The last step is then to substitute r by a terrain following vertical coordinate ζ. It follows a non-orthogonal coordinate system. More details about these modifications can be found in Steppeler et al. (2003) and Schättler et al. (2012).

Discretization

The introduced equations 3.1 to 3.4 have to be solved numerically. In the COSMO model, the finite difference method (e.g. Kalnay, 2003) is applied. For the time integration, a fixed time step Δt is used. To guarantee that the numerical procedure for solving differential equations is stable, the Courant-Friedrichs-Lewy (CFL) criterion (Courant et al., 1928) has to be fulfilled. This is the case when

$$\frac{c\Delta t}{\Delta x} < 1 \tag{3.6}$$
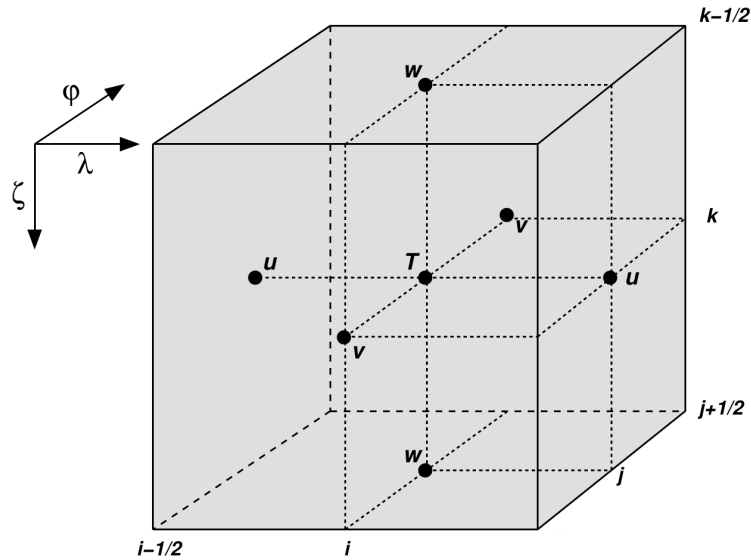
Figure 3.1: A grid box volume $\Delta V = \Delta \zeta \Delta \lambda \Delta \varphi$ showing the Arakawa-C/Lorenz staggering of the dependent model variables. Figure from Schättler et al. (2012).

c denotes here the propagation speed of atmospheric processes. Often, the wind velocity is used. The spatial resolution of the model grid is given by Δx. If the CFL criterion is not fulfilled, more mass than available can be removed from a grid box. This would lead to serious problems regarding the conservation of mass.

To discretize the differential equations, a three dimensional Arakawa-C/Lorenz grid is used. A grid box with side lengths $\Delta \lambda$, $\Delta \varphi$ and $\Delta \zeta$ and associated center coordinates (i, j, k) results. p', T and q^x are defined in the center of the grid box. The components of the wind vector are defined on the half-levels with coordinates (i, j, $k \pm \frac{1}{2}$) for the vertical wind w and ($i \pm \frac{1}{2}$, j, k), respectively (i, $j \pm \frac{1}{2}$, k), for the zonal wind components u and v. The visualization of the Arakawa-C/Lorenz grid is shown in Fig. 3.1.

3.1.2 Initial and boundary conditions

To solve the prognostic differential equations 3.1 to 3.4, a NWP model needs the initial state of the atmosphere. It is given by a set of values for $\vec{v}$, p, T, q^x and t at each grid point. If the used NWP model is a limited area model (like COSMO), the numerical integration needs values for each time step at the grid borders as well. The so called boundary conditions are retrieved from a larger model area, typically a global model.

For this work, the COSMO simulations with $\Delta x = 7\,\mathrm{km}$ were initialized and driven by initial and boundary conditions from the global model of ECMWF. The spatial horizontal resolution of the global model is given by $\Delta x = 0.25° = 27.75\,\mathrm{km}$ ("T639"). An update of the boundary conditions took place every three hours. The simulations with $\Delta x = 2.8\,\mathrm{km}$ were nested into the COSMO-7 km model area. In both cases, the horizontal resolution of the larger model area is coarser than the final simulation. Thus, the boundary conditions had to be interpolated at the grid borders.

3.1.3 Ensemble forecast mode

The simplest way to perform a NWP is to run a single deterministic model simulation. This approach follows the assumption that the future state of the atmosphere is defined explicitly by the current state of the atmosphere. It neglects the fact that the future state of the atmosphere is sensitive to small deviations in the initial conditions (Lorenz, 1963) or to the description of physical processes in the NWP model. Small-scale processes like radiation or turbulence can not always be calculated directly but have to be derived by other variables (sec. 3.1.4).

To access the uncertainties due to initial conditions and due to model physics, ensemble forecast systems are developed. Diverse approaches to derive an ensemble of different single forecasts ("members") exist. Basic concepts of ensemble forecasting can be found in Kalnay (2003), Palmer et al. (2005) and Callado et al. (2013). Perturbations of the initial conditions can be performed for example by singular vectors (e.g. Kalnay, 2003). This method is used in the ensemble prediction system (EPS) of ECMWF (e.g. Leutbecher and Palmer, 2008). A downscaling of ECMWF-EPS is used for the limited-area ensemble prediction system "COSMO-LEPS" (e.g. Marsigli et al., 2005, Marsigli et al., 2008 and Montani et al., 2011). For the ensemble forecast of heavy precipitation events, the perturbing of upper-level potential vorticity (Vich et al., 2011) or the technique of data assimilation (Homar et al., 2002, Vie et al., 2011 or Schumacher and Clark, 2014) are used. A particular approach to receive various initial conditions was presented by Homar et al. (2006b), where human generated sensitive regions were used for the prediction of severe weather. Quite common are multi-model ensembles, where a set of independent numerical model forecasts from several operational centers are used to assess both initial conditions and model physics uncertainties. Examples are given in Ebert (2001), Garcia-Moya et al. (2011) and Hally et al. (2014). The question whether a multi-model ensemble can outperform the best participating single model is addressed in Weigel et al. (2008). As these ensembles are computationally cost-free, they are also referred to as "poor man ensembles". A further possibility to design a low-cost ensemble is to analyze subsequent initialized single predictions. These time-lagged ensembles are used especially for short-range high-resolution model precipitation forecast (e.g. Mittermaier, 2007 or Barrett et al., 2015). Various approaches exist to take into account the uncertainty of model physics. Regarding the prediction of heavy rainfall amounts, variations in soil moisture (e.g. Klüpfel et al., 2011), the impact of surface turbulence parameterization (e.g. Hally et al., 2014) or the role of cloud physics (e.g. Fresnay et al., 2012 or Hally et al., 2014) were found as crucial. An approach to use stochastic perturbations in the numerical parameterization of deep moist convection is presented in Groenemeijer and Craig (2012) and Kober et al. (2015).

For this thesis, two different approaches were used to obtain various realizations of the forecast for deep moist convection. Apart from synoptic-scale perturbations in the initial conditions via ECMWF-EPS, also a stochastic parameterization scheme for cumulus convection was applied.

Ensemble setup for this work

To generate a set of numerical weather predictions for the two heavy precipitation events, introduced in section 2.2.1, two ensemble generation methods were implemented. On the one hand, perturbations in the initial conditions were applied to create an ensemble with large-scale variations. On the other hand, a stochastic parameterization scheme for deep moist convection (see section 3.1.4) caused small-scale modifications in the formation of precipitating cells. Mixed-scale perturbations were used to cover uncertainty effects on both meteorological scales. The different initial conditions as input for the used ensemble simulations, were retrieved from the ECMWF-EPS. This global ensemble consists of one control forecast and 50 perturbed members. The perturbations are based on four different methods: stochastically perturbed parameterization tendencies, stochastic kinetic energy backscatter, singular vectors and ensemble of data assimilation (Leutbecher and Palmer, 2008). For the first time step (thus in the initial conditions), only the singular vectors (e.g. Kalnay, 2003) are applied. The spatial horizontal resolution of the ECMWF-EPS data is given by $\Delta x = 0.25°$ ("T639").

Five different ensembles were developed for this thesis. For the seek of a better comparability, each ensemble consists of 16 members. This number is based on studies of the COSMO-LEPS community (e.g. Montani et al., 2011), where a mesoscale ensemble over Europe is operationally since 2002. The ensembles for this work were set up in the following manner:

- "*Ensemble 16 × 1*" with 16 different initial conditions from ECMWF-EPS and each with 1 realization with a stochastic cumulus convection scheme
  → synoptic-scale perturbations.

- "*Ensemble 8 × 2*" with 8 different initial conditions from ECMWF-EPS and each with 2 realizations with a stochastic cumulus convection scheme
  → mixed-scale perturbations.

- "*Ensemble 4 × 4*" with 4 different initial conditions from ECMWF-EPS and each with 4 realizations with a stochastic cumulus convection scheme
  → mixed-scale perturbations.

- "*Ensemble 2 × 8*" with 2 different initial conditions from ECMWF-EPS and each with 8 realizations with a stochastic cumulus convection scheme
  → mixed-scale perturbations.

- "*Ensemble 1 × 16*" with the control forecast of ECMWF-EPS as initial condition and 16 realizations with a stochastic cumulus convection scheme
  → convective-scale perturbations.

A visualization of the ensemble setup is given in Table 3.1. The detailed setup of the five ensembles is described in section 7.1.

Table 3.1: Visualization of the ensemble setup. Possible individual atmospheric states (gray dots) are represented in a two-dimensional phase space (gray rectangle). Selected representative members are highlighted (colored dots). The temporal evolution of the single ensemble members is indicated by the black arrows.
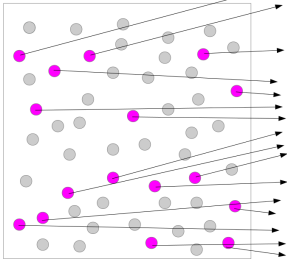
"Ensemble 16 × 1": 	16 initial conditions from ECMWF-EPS → respectively 1 COSMO simulation
"Ensemble 8 × 2": 	8 initial conditions from ECMWF-EPS → respectively 2 COSMO simulations
"Ensemble 4 × 4": 	4 initial conditions from ECMWF-EPS → respectively 4 COSMO simulations
"Ensemble 2 × 8": 	2 initial conditions from ECMWF-EPS → respectively 8 COSMO simulations
"Ensemble 1 × 16": 	1 initial condition from ECMWF-EPS → respectively 16 COSMO simulations
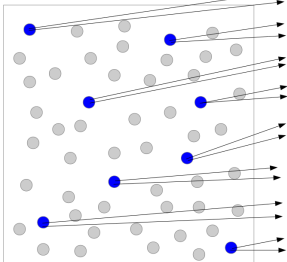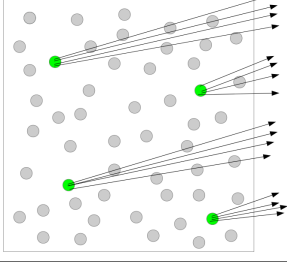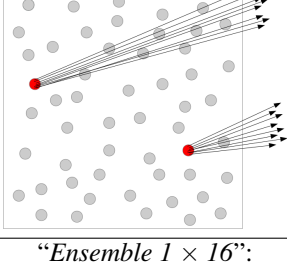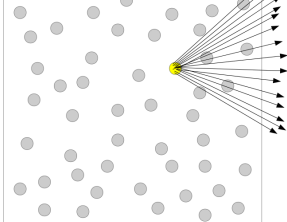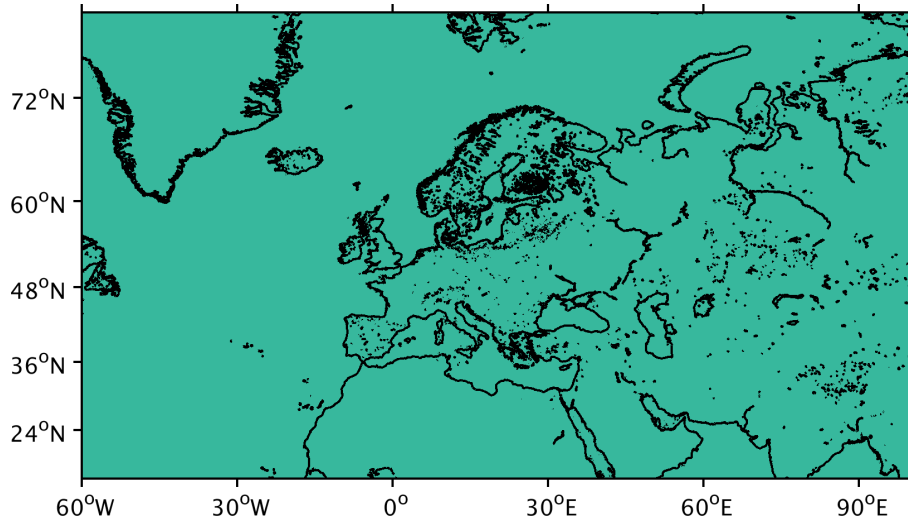
Figure 3.2: Area of the ECMWF-EPS data with the horizontal resolution $\Delta x = 0.25°$ ("T639") which were used for the clustering analysis.

Clustering technique

To establish an ensemble with a subset of the available initial conditions of ECMWF-EPS, the 51 corresponding members have to be selected. To choose the global EPS members in a proper way, a *k*-mean clustering (e.g. MacQueen, 1976) was performed for this work. To apply the *k*-mean method, the members of the global ensemble have to be characterized with specific meteorological variables. Therefore, the principal components analysis (PCA) method (e.g. Wilks, 1995 or Björnsson and Venegas, 1997) was used. This method reduces the number of dimensions and identifies patterns that allow to represent the members of the ensemble.

For the ensembles used in this thesis, the PCA technique had been applied to nine meteorological fields: geopotential height, temperature and relative humidity respectively at the levels of 500 hPa, 700 hPa and 850 hPa. The prescribed number of clusters are obtained by identifying members with the maximum inter-cluster distance over a certain area. A domain with 641×261 grid points, reaching from 60°W and 15°N (lower left corner) until 100°E and 80°N (upper right corner) is considered to identify the most different ECMWF ensemble members (Fig. 3.2). This large domain includes the main synoptic-scale systems, governing the two HyMeX heavy precipitation events under investigation. Within the generated cluster, the member closest to the centroid is selected as representative member (Molteni et al., 2001). The centroids are the points that define the center of mass of each cluster.

3.1.4 Parameterization of deep moist convection

As mentioned before, uncertainties in the weather forecast can result from the fact that some small-scale physical processes cannot be calculated directly, but have to be described by other parameters. After Nyquist (1924), processes to predict with a NWP

system have to have a spatial extent of about two times the distance between points of the model grid. Grid sizes of operationally used NWP models reach from global models with approximately 50 km over mesoscale models with approximately 7 km up to small-scale models with approximately 3 km. Large-eddy-scale (LES) simulations with a horizontal resolution of a few meters are topic of current research. The associated time steps for the discretization are limited through the CFL criterion (eq. 3.6).

Also the size of atmospheric systems differs significantly between synoptic-scale processes (e.g. Rossby waves with sizes of 10^7 m) and small-scale features (like dust devils with sizes of only 10 m in horizontal extension). Dependent on the grid spacing of the numerical model, not all small-scale processes can be resolved directly. Processes like cloud microphysics and deep moist convection can be examples for so called sub-scale processes. Experiments with an explicit description of moist convection in mesoscale models showed that a too coarse horizontal resolution delivers unrealistic too high rainfall rates due to an insufficient representation of non-hydrostatic effects (e.g. Weisman et al., 1997). Through a parameterization, the effects of these physical processes can be described and computed by variables which are explicitly resolved within the NWP model.

Here, the COSMO model is used with horizontal resolutions of 2.8 km (time step of 25 s) and 7 km (time step of 66 s). Especially for this thesis, the parameterization of deep moist convection in the 7 km simulations is an important issue. Instead of the operationally implemented parameterization scheme developed by Tiedtke (1989) a recently developed stochastic scheme, introduced by Plant and Craig (2008), is used.

The Tiedtke scheme

For this scheme, a so called bulk model (similar to Yanai et al., 1973) is used as cloud model. An ensemble of clouds in a certain area is considered as one big cloud. The idea is to represent all development states of convective clouds combined. All up- and downdrafts of the single convection cells are summarized so that only one updraft and one downdraft area in each grid cell exists. The total mass flux *M* of the resulting cloud is given by the sum of the single mass fluxes *m*:

$$M = \sum_i m_i \tag{3.7}$$

To trigger cumulus convection, an air parcel must first reach the CCL (sec. 2.1.2). If the environmental conditions are allowing the air parcel to have further buoyancy at this height, the Tiedtke scheme activates the development of deep moist convection. To estimate the mass flux at the cloud base, a closure assumption is needed. For the Tiedtke scheme, this is given by large-scale ground level moisture convergence (eq. 2.11).

The Plant-Craig scheme

The Plant-Craig scheme is a parameterization of deep convection which was developed to account for the inherent sub-scale uncertainties by means of stochastic modeling of convection effects. Observational studies indicate that a realistic framework for cumulus parameterization should be approached through a spectral cloud ensemble (e.g. Tiedtke, 1989). The Plant-Craig scheme (Plant and Craig, 2008) is based on the Kain-Fritsch parameterization (Kain and Fritsch, 1990 and Kain, 2004), which is, like the Tiedtke scheme, a mass flux scheme. The trigger mechanism for deep convection is a certain positive vertical velocity of the air parcel above the LFC. The intensity of the convection is then defined by the closure assumption. In the Kain-Fritsch scheme, 90% of the CAPE (eq. 2.5) in a grid cell has to be eliminated before convection stops.

The main idea of the Plant-Craig scheme is to reproduce the natural variability of convective clouds in a NWP model. Thus, the parameterization generates a varying number of clouds with different sizes in a certain area. For this purpose, the closure assumption does not need to be fulfilled in every single grid cell, but averaged in a larger area (e.g. several grid cells). Every time the Plant-Craig scheme is called in a NWP model, a different arrangement of stochastically generated clouds is realized in this area. This is based on a probability distribution function, given in Craig and Cohen (2006). The distribution p of mass flux m per cloud, based on a mean massflux $< m >$, is given by:

$$p(m)dm = \frac{1}{<m>}e^{\frac{-m}{<m>}}dm \qquad (3.8)$$

The probability that a cloud of diameter r is initiated in the time interval dt is given by:

$$<N> p(r)dr\frac{dt}{T} = \frac{<M>}{<m>}\frac{2r}{<r^2>}e^{\frac{-r^2}{<r^2>}}dr\frac{dt}{T} \qquad (3.9)$$

with $< ... > $ = ensemble mean, $M = \Sigma m_i$ = total massflux per grid cell, N = number of clouds per grid cell, dt = time step of convection scheme and T = life time of a cloud. The default value of T is taken as 45 min. The mean mass flux per cloud $< m >$ and the mean cloud radius $\sqrt{<r^2>}$ are held constant. $< m >$ was estimated by Cohen and Craig (2006) and modified by Groenemeijer and Craig (2012) to $< m >= 10^7 \, \mathrm{kg\,s^{-1}}$. The root mean squared cloud radius was set to $\sqrt{<r^2>} = 1200 \, \mathrm{m}$ in Groenemeijer and Craig (2012). These values are used as well for this work.
Besides idealized tests (Keane and Plant, 2012 and Keane et al., 2014), the PC scheme was implemented in the COSMO model. In Groenemeijer and Craig (2012), the internal variability of the PC scheme was contrasted with the variability of large-scale perturbations. It was found that the variability due to the stochastic cumulus convection parameterization is rather high for weakly forced synoptic situations. A positive effect on the forecast quality of such an ensemble based on the Plant-Craig scheme was affirmed by Kober et al. (2015).
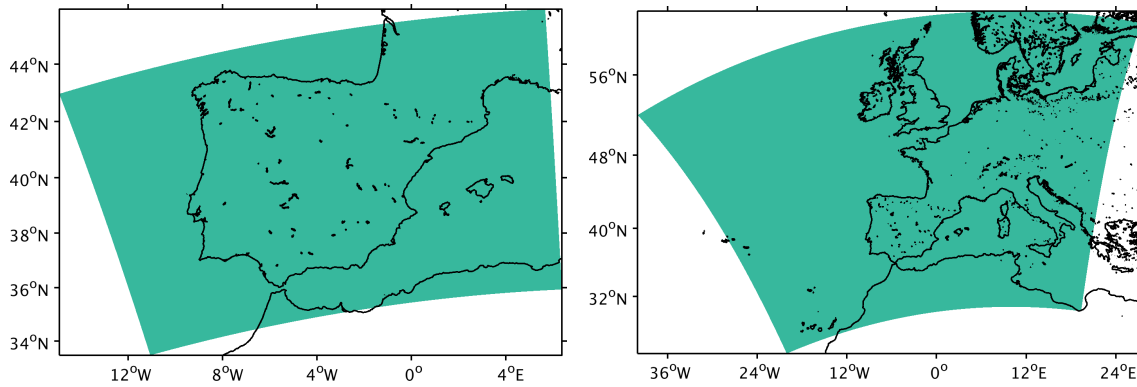
Figure 3.3: Left: Model area for the COSMO simulations with a horizontal resolution of 2.8 km. Right: Model area for the COSMO simulations with a horizontal resolution of 7 km which were used as initial and boundary conditions for the 2.8 km simulations.

3.1.5 Model domains

High resolution simulations

One aim of this work is to analyze the skill of numerical model predictions in simulating extreme precipitation that occurs in the Mediterranean region. Therefore, the 2.8 km model domain was chosen from 11.0°W and 33.5°N (lower left corner) until 5.7°E and 45.9°N (upper right corner) (Fig. 3.3, left). This means a grid size of 400×600 points. These simulations were nested in COSMO simulations with a horizontal resolution of 7 km. Based on the large-scale situation of HyMeX IOP8, the 7 km domain was chosen large enough to contain the most important synoptic features leading to the heavy precipitation event. It spans from 20.1°W and 24.8°N (lower left corner) until 28.1°E and 61.0°N (upper right corner) (Fig. 3.3, right). This area consists of 498×598 grid points. To have similar grid spacing values for all grid points, the model equator should be located in the middle of the North-South direction of the model area. For this case, a rotated North pole with latitude $NP_{lat} = 40°N$ and longitude $NP_{lon} = -170°W$ was chosen for both model domains. 50 vertical layers from 20 m to 22 km height are used for the presented study.
For the 2.8 km simulations, deep moist convection is resolved directly (Weisman et al., 1997). Shallow convection is parameterized by a reduced Tiedtke scheme. The setup for all physical parameterizations is the same as in the operational setup of COSMO-DE. For the coarser COSMO simulations with a horizontal resolution of 7 km, deep moist convection was parameterized with the Plant-Craig scheme and ECMWF analyses data with the horizontal resolution $\Delta x = 0.25°$ ("T639") served as initial and boundary conditions. An update of the boundary conditions was performed every three hours.

Furthermore, this thesis investigates the predictability of Mediterranean heavy precipitation events. To provide early enough warnings, medium-range weather forecasts are evaluated. For this reason, the COSMO model with a horizontal resolution of 7 km was used. Such a horizontal gridspacing is commonly used in mesoscale models to predict systems like e.g. mesoscale convective systems (sec. 2.1.3). The COSMO model area with 450×610 grid points reaches from 9°W and 31°N (lower left corner) until 29.0625°E and
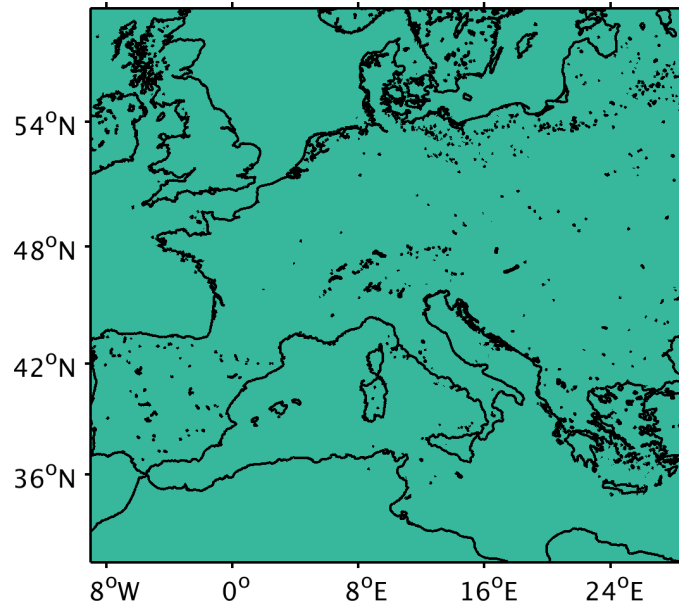
Figure 3.4: Model area for the COSMO simulations with a horizontal resolution of 7 km which were used for the predictability study.

59.0625°N (upper right corner) (Fig. 3.4). It is the same area as used by the COSMO-LEPS community (e.g. Montani et al., 2011).

3.2 Further Eulerian and Lagrangian modeling tools

3.2.1 The AROME-WMED model

The NWP model AROME-WMED is a special version of the French operationally used AROME model (Seity et al., 2011) and is operated with a horizontal resolution of 2.5 km. Cumulus and stratocumulus convection is parameterized after Turner et al. (2012). The AROME-WMED model was developed for the HyMeX project (sec. 2.2.1) to get real time predictions for the associated field campaign. The model area reaches from 8.5°W and 34.5°N (lower left corner) until 16.75°E and 47.5°N (upper right corner) (Fig. 3.5). With 521×1011 grid points, it is slightly larger than the operational model area and consists of more sea surface grid points. The initial and boundary conditions for AROME-WMED are provided by the French global model ARPEGE ("Action de Recherche Petite Echelle Grande Echelle"), described in Déqué et al. (1994).

Besides the adapted model area, an improvement was made by not only assimilating standard observations like in the operational model, but to assimilate further HyMeX measurement data like additional radiosoundings and data from pressurized boundary layer balloons. A reanalysis of AROME-WMED was produced every 3 hours from 05 September 2012 until 05 November 2012. For the 0000 UTC reanalysis of each day, a 54 h forecast was then performed. The associated dataset for the 28 September 2012 (Fourrié and Nuret, 2014) was used for this thesis.
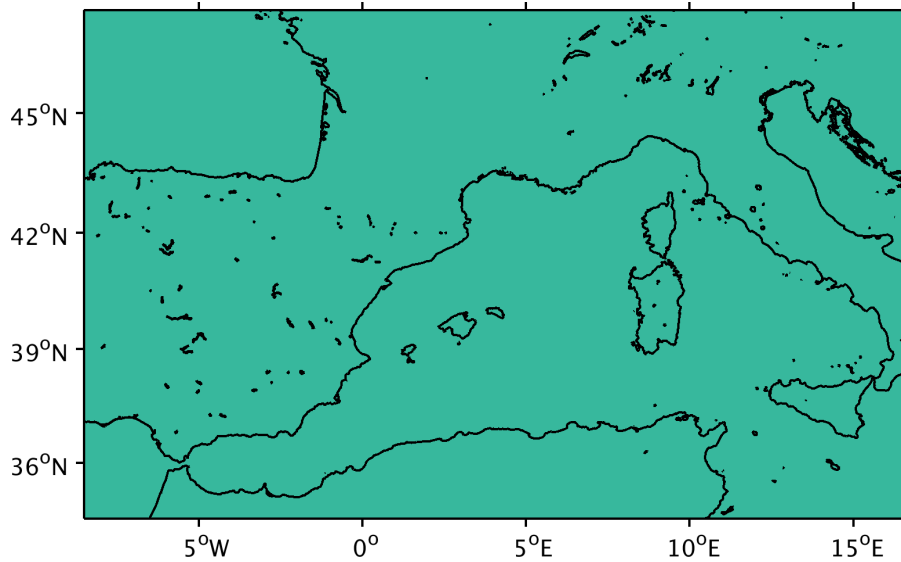
Figure 3.5: Area of the AROME-WMED model domain with a horizontal resolution of 2.5 km.

3.2.2 Lagranto - Lagrangian Analysis Tool

To examine humidity transport pathways within the synoptic systems, the Lagrangian Analysis Tool Lagranto, which calculates trajectories with the Lagrangian approach, is used. The software, developed by Wernli and Davies (1997), is publicly available as version Lagranto 2.0 (Sprenger and Wernli, 2015). Lagranto is designed for use with ECMWF and COSMO model input data. The Lagrangian trajectory calculation enables to follow an air parcel and its properties, e.g. temperature, humidity and trace gas concentration with high resolution in space and time. The calculation of trajectories is well-known and often used for example in synoptic meteorology to identify warm conveyor belts (Sprenger and Wernli, 2015), to analyze the structure of extratropical cyclones (Wernli, 1997), to investigate Saharan dust (Reiff et al., 1986), Arctic haze transports (Kahl et al., 1989) or air mass transport in the Antarctic (Kottmeier and Fay, 1998). Also pathways of water vapor are already investigated worldwide with Lagrangian trajectories, e.g. from d'Abreton and Tyson (1996) over southern Africa. A very extensive review and bibliography of the computation and usage of trajectories is given by Stohl (1998). Shaw (1903) recognized on the basis of the investigation of a winter storm event the importance of distinguishing between the pathway of an air particle in a cyclone (so called trajectory) and the distance traveled by the cyclone. In contrast to most weather prediction models, which describe the state of the atmosphere at a particular time in forecast fields (Eulerian approach), the program Lagranto uses the Lagrangian approach. The main focus is to describe the temporal evolution of the atmospheric variables along the pathway of a single air parcel.

Data basis

To calculate the humidity transport pathways, COSMO forecasts are used. The trajectory pathway depends on the forecast quality on the relevant scale. The COSMO data are used at a spatial resolution of 7 km and a temporal resolution of 1 h at 40 vertical pressure levels. The starting area for the trajectories is limited to a box from 25°W to 20°E and from 25°N to 50°N. The meteorological variables for trajectory calculation and interpretation are temperature, relative humidity, specific humidity, pressure and the three-dimensional wind vector on the model levels and the surface pressure. The model predictions used for trajectory calculations are composed from two forecast runs daily. One simulation started at 0000 UTC, the second at 1200 UTC. From the first model initialization, the hourly time steps between 0600 UTC and 1800 UTC and from the second model initialization, the hourly time steps between 1800 UTC and 0600 UTC (following day) are picked out.

Operation mode

Lagranto is based on shell scripts and was developed for the calculation of forward and backward trajectories (Sprenger and Wernli, 2015). Within the trajectory calculation, an air parcel is traced over time with changing wind conditions. This contrasts with NWP data which give for each computation step an overall picture of the atmospheric state at each grid point. With the method of the trajectory calculation, Lagrangian movement patterns from Eulerian model data are gained.

Lagranto includes several steps of calculation. The starting points of the trajectories are determined by the starting area and start time. In a next step, the meteorological variables are calculated for further time steps along the trajectories. In a final step, a chosen selection criterion is used, which limits the number of calculated trajectories and focuses on the essential parts of the flow patterns.

For this work a suitable selection criterion is to overcome a certain pressure difference along the calculated trajectories. Here, an ascent of the air parcels of at least 600 hPa is chosen. Depending on vertical motion of the air parcels, this serves on the large scale to identify "Warm Conveyor Belts" (Wernli, 1997) or deep moist convection on the convective scale. Also should be noted that all trajectories that get below the earth surface, are lifted by 10 hPa to stay in the trajectory ensemble (Sprenger and Wernli, 2015). Trajectories are not started in parts of the investigation area if the orography is higher than the starting level of the trajectories.

3.3 Forecast verification

In order to test to what extent the model simulation reproduces the observed weather, several methods exist to compare the NWP output with meteorological measurement data. For a quick overview whether model and measurements fit together, the so called "eyeball" method can be used. With this method, observations and model output are compared subjectively. In this way, structures in meteorological fields and the intensity of occurring

values can be roughly contrasted with each other.

To quantify how well model and observations fit together, an objective verification method should be used. Objective methods have the advantage that a score - which quantitatively measures the quality - results at the end of the investigation. Different situations with different resulting score values can then be compared objectively with each other. If a climatology or another objective reference is available to compare with a meteorological field, a "skill score" can be calculated.

In this section, different objective verification methods are introduced. Starting with traditional scores for continuous as well as for dichotomous variables, a recently developed spatial verification score is presented as well. Here, the shape of a meteorological field is taken into account. Using this novel approach, double penalty errors, e.g. resulting from a shift of variable fields between model and observations can be eliminated. Due to a relatively simple definition of the limits of a precipitation field, this spatial score is often used for the verification of rain events. The last part of this section is focusing on verification scores for probabilistic datasets. To verify meteorological ensemble forecasts and to quantify the quality of various ensembles, several probabilistic verification methods are used.

3.3.1 Interpolation

Before two datasets can be compared which each other, it often happens that the geographical overlap between both datasets is not totally identical. If both datasets are covered with a large density of data, it may be sufficient to compare always nearest data points with each other. In that case, it is assumed that the environmental conditions are similar for both treated points. If the ambient conditions are unresembling, more than one surrounding data point has to be considered for the comparison between the two datasets. Usually one dataset is then interpolated on the grid of the other dataset or both datasets are interpolated onto a reference one.

After the nearest neighbor comparison, the second simplest interpolation method is the so called linear interpolation. Here, the value $f(x)$ at the point x is determined by two surrounding data points x_a and x_b via:

$$f(x) = f(x_a)\frac{x_b - x}{x_b - x_a} + f(x_b)\frac{x - x_a}{x_b - x_a}$$ (3.10)

So, the slope between x_a and x is to be assumed the same as between x_a and x_b.

A generalization of the linear interpolation can be achieved by a polynomial interpolation. The polynomial $p(x)$ of degree n is given by:

$$p_n(x) = \sum_{k=0}^{n} a_k \cdot x^k$$ (3.11)

In this work, two interpolation methods were applied. For a comparison between the COSMO and the AROME-WMED model results, the linear interpolation method (eq. 3.10) was used. This was possible due to a very similar horizontal grid spacing of both models. The comparison of COSMO output with measurement data in chapters 4, 5 and 7 was performed via a cubic interpolation method (eq. 3.11 with $n = 3$).

3.3.2 Traditional verification scores for continuous variables

To verify an area with several observation points against a NWP output field or to compare a time series of measurement data of e.g. one meteorological station against the forecast time series on the same point, verification scores for continuous variables (e.g. Wilks, 1995 or Jolliffe and Stephenson, 2012) can be applied. After an interpolation between two datasets, a "point-wise" verification can be performed.

Mean error

Gaining a picture whether an offset (a "bias") exists between measurement data and model output, the mean error is one of the simplest scores to calculate. For N pairs of measurement data O and model output data F, the mean error (ME) is given by:

$$\mathrm{ME} = \frac{1}{N} \sum_{i=1}^{N} (F_i - O_i) \tag{3.12}$$

For the global dataset, the average difference between forecast and observation is calculated. If $\mathrm{ME} > 0$, the model is overestimating the forecast, if $\mathrm{ME} < 0$, the model is underestimating the forecast for the selected points. The perfect case is given by $\mathrm{ME} = 0$. But this case does not implicit that model and observation field are identically. It can happen that areas with negative ME are balanced by areas with positive ME and vice versa. This challenge can be overcome e.g. by the correlation coefficient (eq. 3.14).

Root mean square error

For a rough estimation whether the NWP has large discrepancies in comparison to the observations, the root mean square error RMSE is a suitable verification score. It is given by:

$$\mathrm{RMSE} = \sqrt{\frac{1}{N} \sum_{i=1}^{N} (F_i - O_i)^2} \tag{3.13}$$

Due to the squared difference of forecast and observation, large differences between both outcomes are strongly penalized with this measure.

Table 3.2: Contingency table.

	Observation YES	**Observation NO**
Forecast YES	Hit	False alarm
Forecast NO	Miss	Correct negative

Correlation coefficient

If the interest of a verification lies in the investigation of different structures in the fields of model and observation output, the correlation coefficient COR can be applied. It is given by:

$$\text{COR} = \frac{\sum_{i=1}^{N}\left[(F_i - \overline{F_i})(O_i - \overline{O_i})\right]}{\sqrt{\sum_{i=1}^{N}\left[(F_i - \overline{F_i})^2\right]}\sqrt{\sum_{i=1}^{N}\left[(O_i - \overline{O_i})^2\right]}} \qquad (3.14)$$

Resulting values are located between -1 and 1, where 1 means a perfect correlation and -1 a perfect anti-correlation of forecast and observation.
The correlation is insensitive to bias (eq. 3.12). Even if large offset exists between the two variable fields, high correlations can result between the fields. A graphical visualization of the correlation coefficient is given by a scatter plot.

3.3.3 Traditional verification scores for dichotomous variables

If the forecaster's interest is driven by the question if a certain threshold value (e.g. of precipitation) has been over- or undershooted, verification scores being able to distinguish between a "yes" or a "no" case are employed. After e.g. Wilks (1995) and Jolliffe and Stephenson (2012), the "yes" and "no" events can be summarized into a contingency table (Tab. 3.2).
If a "yes" event is occurring in the forecast and in the observation, this case is named "hit". If the forecast predicted an event which did not occurred in reality, this is called a "false alarm". If an event was not forecast, but measured, a "miss" is the used expression. When both, forecast and observation, had no pre-defined event, a "correct negative" arose. Based on the contingency table, several verification scores can be defined. In the following the scores used in this work are presented.

Probability of detection

To answer the question how many real occurring events were forecast, the probability of detection (POD) can be used. The POD is given by:

$$\text{POD} = \frac{\text{hits}}{\text{hits} + \text{misses}} \qquad (3.15)$$
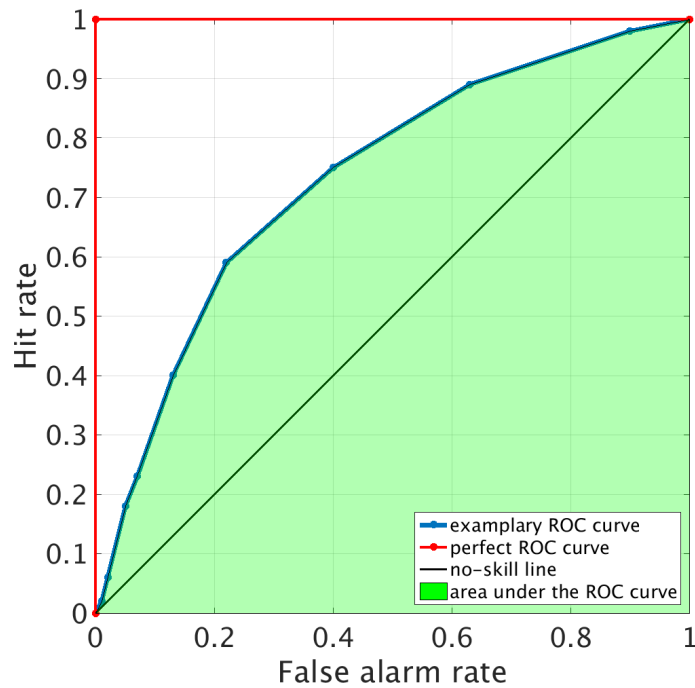
Figure 3.6: Example of a ROC curve (blue line). Additionally, the perfect ROC curve (red line), the no-skill line (black line) and the area under the ROC curve (green area) are indicated.

and is also called hit rate (HIT). It indicates the ratio of correct forecasts with respect to total observations. POD can reach values between 0 and 1. In the perfect case of POD $= 1$, all measured events were forecast correctly.

Probability of false detection

As the POD does not take into account how many false alarms exists, the probability of false detection (POFD) should be used additionally. It is given by:

$$\text{POFD} = \frac{\text{false alarms}}{\text{false alarms + correct negatives}} \tag{3.16}$$

and is also called false alarm rate (FAR). Values of POFD can be located between 0 and 1. In the perfect case of POFD $= 0$, no false alarms were produced by the model.

Relative operating characteristic

One verification score which includes the two already introduced scores, is the relative operating characteristic (ROC). The graphical representation of this score consists of the HIT (eq. 3.15) on the y-axis and the FAR (eq. 3.16) on the x-axis. To construct a so

called ROC curve, various combinations of HIT and FAR are calculated for *n* different threshold values of a meteorological variable. The results are linked with a line which begins at the artificial point (0,0) and ends at the artificial point (1,1). A perfect ROC would be represented by a curve traveling from the bottom left (0,0) over the top left (0,1) of diagram to the top right (1,1) of the diagram (Fig. 3.6, red line). Then, it would be POD = 1 and POFD = 0 for the whole verification dataset. A sketch of an exemplary ROC curve is shown in Fig. 3.6 (blue line).

Calculating the area under the ROC-curve (AUC) (Fig. 3.6, green area) leads to a number to quantify the verification skill. The integral can be approximated by (Jolliffe and Stephenson, 2012):

$$\text{AUC} = -\sum_{n=1}^{n} \text{HIT}(n) \cdot [\text{FAR}(n) - \text{FAR}(n-1)] \qquad (3.17)$$

Values for AUC are located between 0 (worst case) to 1 (perfect case). An AUC of 0.5 means that no identified skill (beyond the hits by chance) exists for the forecasts to predict the observations. This is indicated with the "no skill" line in the diagram (Fig. 3.6, black line).

The ROC-curve can also be constructed for the verification of probabilistic forecasts. The detailed description is given in section 3.3.5.

3.3.4 Spatial verification score

One challenge in numerical weather forecast is the fact that predicting the occurrence of rain is easier than predicting the amount of rain in any specific location (Doswell et al., 1996). As mentioned above, traditional verification methods can have the problem that a spatial shift between forecast and observed meteorological field can lead to a double penalty error. If, for example, a precipitation area was forecast at location *x* but was measured at location $x + \Delta x$ where $x + \Delta x$ is relatively close to *x*, then, a false alarm would be produced at location $x + \Delta x$ and additionally a miss would be produced at location *x*. The shift of the precipitation area in the forecast is thus punished twice in this case.

To avoid this double penalty problem, spatial verification methods were developed. These object-based verification methods try to link objects in a forecast field with similar objects in the measurement data. These linkage which can be often seen easily in the "eyeball" method is tried to be transformed in an objective detection code. Examples for spatial verification methods are "SAL" (Wernli et al., 2008 and Wernli et al., 2009), "MODE" (The Method for Object-Based Diagnostic Evaluation) (Davis et al., 2006a, Davis et al., 2006b and Davis et al., 2009) and "DAS" (Displacement and Amplitude Score) (Keil and Craig, 2009). An overview and comparison of these and further spatial verification methods is given in Ahijevych et al. (2009) and Gilleland et al. (2009).

For this work, the SAL verification technique, developed by Wernli et al. (2008), was used for precipitation validation. The method is introduced in the following.
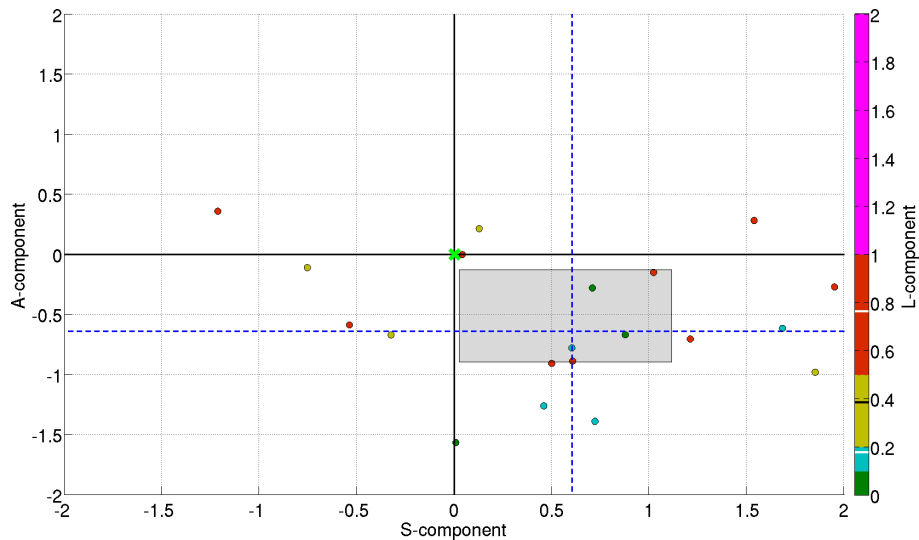
Figure 3.7: Example of a SAL plot. The S-component is represented through the x-axis, the A-component through the y-axis and the L-component is marked with a colorbar. The interquartile range, i.e. the difference of the 75th and the 25th percentile, of the single SAL components is represented through the grey rectangle (for S and A) and through the bold white bars in the colorbar (for L). The median values for all SAL components are shown by the blue dashed lines (for S and A) and by the bold black bar in the colorbar (for L). The increments of the colorbar are taken from Zimmer and Wernli (2011).

SAL-method

The SAL method aims to compare features in meteorological fields in structure (S-component), amplitude (A-component) and location (L-component). Typically, a field with model data is validated with observational data. Both fields must have the same horizontal grid spacing and have to be available in the same area. In this work, the method was employed for precipitation and radar reflectivity verification. The following description of SAL is constructed exemplarily on the meteorological variable of precipitation.

To calculate the S- and the L-component, single precipitation patterns in the area of interest have to be carved out. To define those patterns, a threshold value R has to be defined. As suggested in Wernli et al. (2009), R is given for the respective precipitation field by 1/15 of the 95th percentile of all grid point values in the precipitation field for values greater than 0.1 mm. Based on R, a Boolean matrix is constructed. "0" stands for precipitation values smaller than R and "1" for precipitation values equal or greater than R. With a clustering algorithm, the single precipitation patterns can be defined.

The size (number of grid points), the integrated precipitation amount (precipitation sum) and a scaled volume (precipitation sum devided by the maximum precipitation) are calculated for each pattern with more than three grid points. Additionally, the center of mass of each pattern as well as the total mass center of both precipitation fields, x, are determined. With the weighted averaged distance r between the individual mass centers and the total mass center, the L-component can be derived.

38

The S-component, which provides information of the accordance in size and shape of both precipitation fields, is then derived via the weighted means of all patterns' scaled volumes V_{mod} and V_{obs} for the two respective modeled and observed precipitation fields. The orientation of a pattern is not taken into account (Wernli et al., 2009). It results for the S-component:

$$S = \frac{2 \cdot (V_{mod} - V_{obs})}{V_{mod} + V_{obs}} \tag{3.18}$$

The A-component delivers the information whether one precipitation field over- or underestimates the domain averaged precipitation D of the other precipitation field. Is follows:

$$A = \frac{2 \cdot (D_{mod} - D_{obs})}{D_{mod} + D_{obs}} \tag{3.19}$$

Finally, the location component, which helps to gain a picture about the location of the single precipitation patterns, consists of the upper introduced x and r values and of the largest distance d within the precipitation fields. The first part is given by:

$$L_1 = \frac{\sqrt{(x_{mod})^2 + (x_{obs})^2}}{d}$$

and the second part by:

$$L_2 = \frac{2 \cdot |(r_{mod})^2 + (r_{obs})^2|}{d}$$

The location component is then defined as:

$$L = L_1 + L_2 \tag{3.20}$$

More details about the calculation of the three components can be found in Wernli et al. (2008).

S- and A-components are adjusted so that the range of the resulting values are within -2 and 2, whereas the values of the L-component range between 0 and 2. A perfect match between both precipitation fields would be if all three components were zero. If $S < 0$ ($S > 0$), the precipitation patterns in the modeled field are smaller (larger) than in the observed field. If $A < 0$ ($A > 0$), the precipitation patterns in the modeled field are weaker (stronger) than in the observed field. The larger L, the more the dispersion of the precipitation patterns in the modeled field differs from the observed one.

To visualize the calculated SAL components, they can be inserted in a SAL plot. In an artificial example (Fig. 3.7), most of the points are situated in the quadrant where $S > 0$ and $A < 0$. This situation would be characterized by an underestimation of the precipitation amount and a coexisting overestimation of the size of the precipitation areas. More examples and interpretations of several SAL studies can be found in chapter 5.

3.3.5 Probabilistic verification scores

To assess the performance of an ensemble forecast, special verification scores were designed to best describe the main characteristics of a probabilistic forecast. In contrary to

deterministic simulations, which produce meteorological parameters directly, an ensemble finally produces probabilities, which must be verified like that. In this section, several of these scores are introduced.

Ensemble spread

The so called ensemble spread corresponds to the ensemble variance and is a measure of the dispersion in the ensemble. It is no verification score, but a characteristic parameter of an ensemble. It can be given by the sample standard deviation:

$$\sigma = \sqrt{\frac{1}{N-1} \sum_{i=1}^{N} (F_i - \overline{F})^2} \qquad (3.21)$$

But also other measures of spread, like anomaly correlation (Scherrer et al., 2004) or interquartile range, are used. In a well calibrated system, the spread of the ensemble mean should be equal to the error of the ensemble mean (e.g. Palmer and Tibaldi, 1988 or Palmer et al., 2005). This is also known as the spread-skill relationship (Whitaker and Loughe, 1998).

Rank histogram

With rank histograms, the quality of the ensemble spread (eq. 3.21) can be estimated. To create a rank histogram, the predicted values of all ensemble members N are compared with the associated measurement value at a certain location. First, the output of the ensemble members is sorted with increasing height. Afterwards, the measurement value is sorted into the ensemble results and so the rank of the observation is defined. If the measurement value is larger than all ensemble members, the rank is set to $N+1$. If the observational result is equal to some of the ensemble members, the rank is chosen as a random number between those matches. The rank is only calculated for locations where a measurement is available.

After the ranks are calculated at several locations or at one location for a certain number of time steps, a rank histogram can be generated. Therefore, the frequency of how often a rank occurred is plotted against the possible ranks between 1 and $N+1$. The shape of the rank histogram gives an indication of how well the ensemble spread is representing the variability of the observations. After e.g. Jolliffe and Stephenson (2012), a rank histogram for reliable ensemble output would have a close to flat structure (Fig. 3.8, top) where each rank is equally distributed. If the spread of the ensemble is too small (underdispersiveness) or too large (overdispersiveness) this would lead in an U-shaped (Fig. 3.8, middle left) or dome-shaped (Fig. 3.8, middle right) rank histogram. A biased ensemble will lead to an asymmetric structure (Fig. 3.8, bottom) of the rank histogram. Further interpretation information about the interpretation of rank histograms can be found in Hamill (2001).
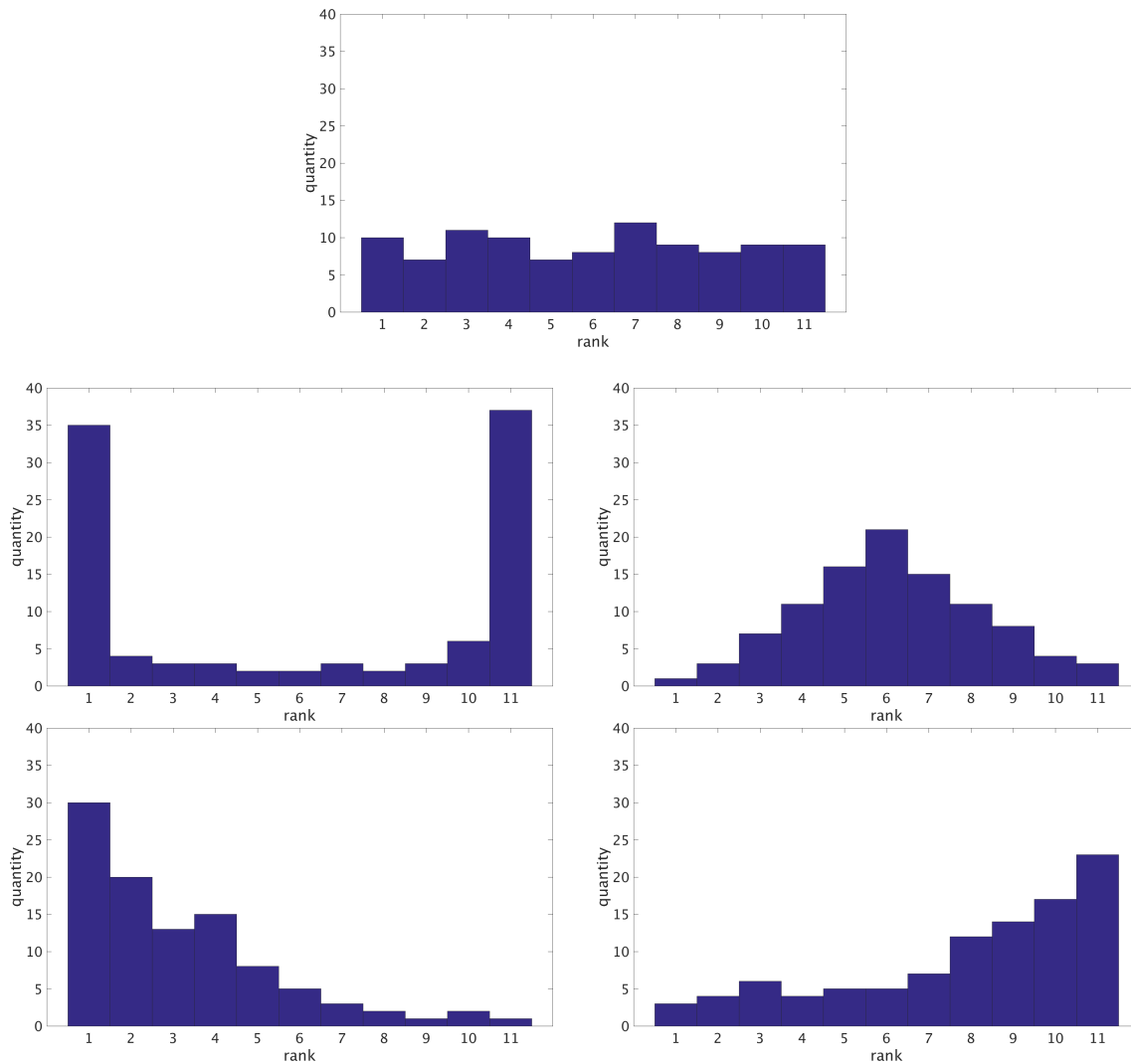
Figure 3.8: Examples of rank histograms. Top: reliable ensemble (flat rank histogram). Middle left: underdispersive ensemble (U-shaped rank histogram). Middle right: overdispersive ensemble (dome-shaped rank histogram). Bottom: biased ensembles (asymmetric rank histograms).

Relative operating characteristic

In section 3.3.3 the ROC was already introduced for the verification of traditional dichotomous variables. But also for probabilistic forecasts, the ROC and the associated AUC (eq. 3.17) is a widely-used verification score. For ensemble predictions, the contingency table (Tab. 3.2) is now build up based on a probabilistic threshold (and not on a threshold value of a meteorological variable). What is answered here, is whether a certain pre-defined meteorological event was observed and/or forecast with a certain probability. Likewise as before, hit rate (eq. 3.15) and false alarm rate (eq. 3.16) can then be plotted against each other. A perfect ROC curve travels in the ROC diagram from the bottom left to the top left and then across to the top right of diagram (see Fig. 3.6).

4 Analysis of preconditions for deep convection

This thesis focuses on the better understanding of the physical processes which lead to the initiation and the development of a heavy precipitation event in the western Mediterranean. This is done by a detailed diagnostic study of HyMeX IOP8 in the following three chapters.

In section 2.1, the three main processes for the initiation of deep convection were introduced: sufficient low-level moisture, potential instability and triggering mechanisms. To study how, where and when the ingredients for deep convection (Doswell et al., 1996) were fulfilled during HyMeX IOP8, this event is studied by means of HyMeX measurement data and numerical simulations with the COSMO model.

Observational data from the HyMeX campaign and results from a COSMO simulation are used to first present the available amount of moisture for the whole area of interest. Then, the evolution of instability at several distinct points is analyzed. Furthermore, plausible trigger mechanisms for deep convection are evaluated. All measurement data are contrasted with a spatially high resolved COSMO simulation ($\Delta x = 2.8\,\text{km}$). The initialization time of the simulation was set to 0600 UTC on 28 September 2012, thus very close to the occurrence of the heaviest precipitation, measured around 1200 UTC. This little time span allows only small error growth between the initial conditions and the outcome of the first intense rainfalls.

In the subsequent two chapters, follow-up studies are presented. Resulting from the above mentioned basic preconditions, intense precipitation occurred at specific places during specific time steps. In chapter 5, the COSMO model is analyzed regarding its ability to predict such a heavy rainfall event. Chapter 6 focuses on continuative numerical model studies of HyMeX IOP8. The atmospheric stability and trigger mechanisms for the heavy precipitation event are investigated in more detail. Processes over the Mediterranean Sea as well as orographic effects over land are emphasized. Furthermore, Lagrangian trajectories are used to study the significant moisture sources for HyMeX IOP8.

4.1 Moisture and heat availability

After the Archimedes' principle, air parcels with a density lower than the surrounding environment experience a positive vertical upward force, called buoyancy (e.g. Emanuel, 1994). Air density is dependent on temperature and moisture. The warmer the air, the
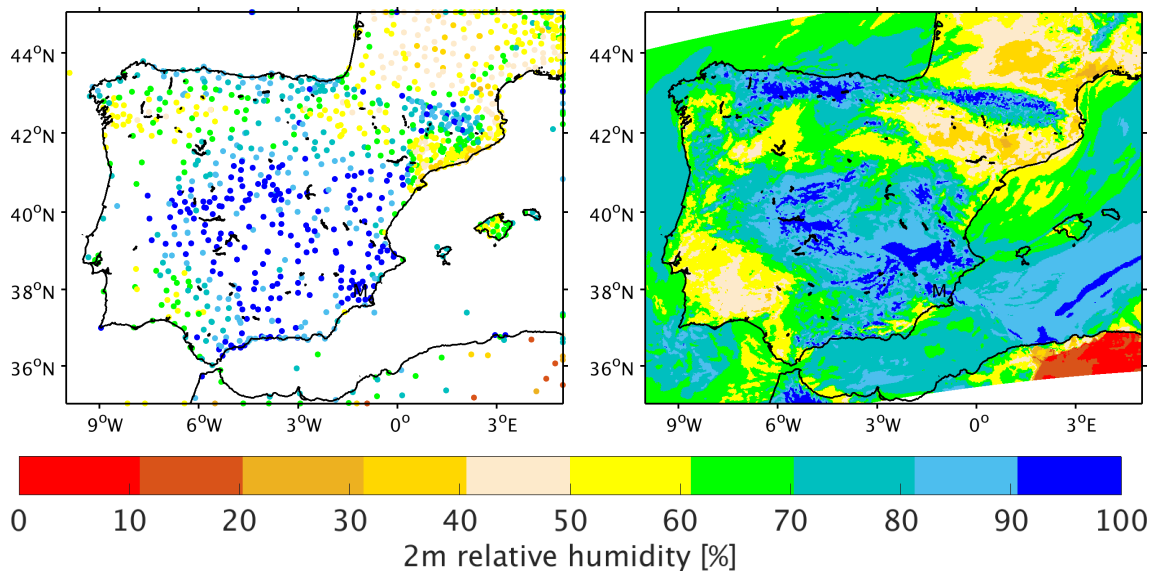
Figure 4.1: Relative humidity [%] in 2 m height on 28 September 2012, 1500 UTC. Murcia is indicated by an "M". Left: measurement data from the surface stations in the area of interest. Right: corresponding simulated COSMO values.

lighter it is due to its thermal expansion. A higher moisture content also leads to a reduced density. This is caused through a displacement of N_2 and O_2 molecules by lighter H_2O molecules. The atmospheric stability is defined by the availability of buoyancy. The release of buoyant instability, thus the release of potential energy, is then called convection (Sherwood, 2000).

Moisture and temperature are thus the two parameters that determine stability in the atmosphere. As instability is a precondition for convection, these two parameters are studied in the following. First, near surface air moisture is studied. It is a necessary ingredient for the efficient generation of intense rainfall rates. Without moisture, only dry convection could occur. Within the western Mediterranean area, the primary source of low-level atmospheric moisture results from the Mediterranean Sea itself (see references in section 2.2). The moisture content over the sea surface is insufficiently represented by meteorological measurements, like surface stations. Thus, the information of the available observations over land is combined in the following with the information of the COSMO model output.

The surface weather stations during HyMeX IOP8 show high relative humidity values above 90% on 28 September, 1500 UTC, in the region around Murcia (Fig. 4.1, left). In this area, highest precipitation values were measured at this time. So, the probability that the heavy precipitation was fed by humid ground-level airmasses in this region, is obvious. Around Palma, the relative humidity ranged up to only 60%. Even drier is the situation near Barcelona, where values of only 30% to 40% of relative humidity were measured.

Regarding the associated COSMO simulated values (Fig. 4.1, right), a strong correspondence between numerical model output and surface station measurements can be seen. The widespread moist airmass over central Spain is very well represented in the model. Also the surrounding drier regions in Portugal and the Ebro valley (south of the Pyrenees)
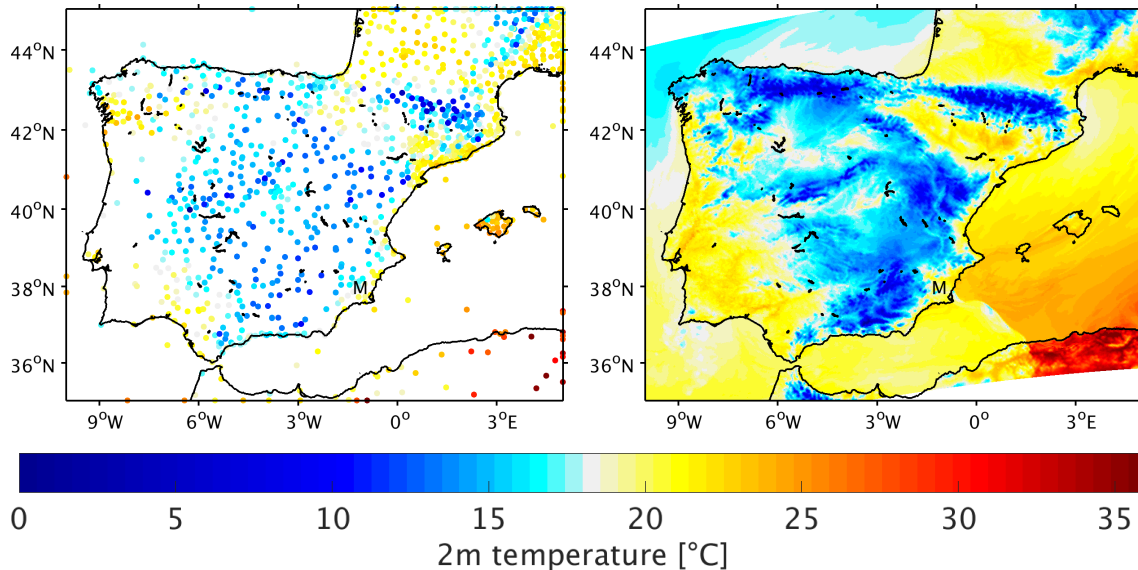
Figure 4.2: Temperature [°C] in 2 m height on 28 September 2012, 1500 UTC. Murcia is indicated by an "M". Left: measurement data from the surface stations in the area of interest. Right: corresponding simulated COSMO values.

are captured satisfactorily. With this investigation, the assumption is dared that the good agreement of measurements and numerical model over land can conclude to a similar good correspondence over the Mediterranean Sea. Then, it can be seen that the moist airmass is extended over the sea surface and covers a large region between the Balearic Islands and the Algerian coast. A relatively sharp boundary between moist and drier air, reaching from Murcia towards the Algerian coast, can be detected. This line, associated with the cold front of the present surface low-pressure system (Fig. 2.2, top, white iso-lines), will be investigated also in the following sections.

Warmer air can contain more water vapor than colder air and thus more latent heat release can occur from condensation. Therefore, also surface temperatures are of interest. At 1500 UTC, at the same time shown for the relative humidity (Fig. 4.1), surface temperature values at the Mediterranean coastlines as well as in southern France, range up to 23 °C (Fig. 4.2, left). Stations at the Balearic Islands even measured temperature values of more than 25 °C. In the inland of Spain considerable cooler temperature values of around 15 °C were reported due to the elevated orography in this part of the country. The numerical simulation with COSMO (Fig. 4.2, right) shows a very similar surface temperature field. The simulated temperature field over the Mediterranean Sea is thus taken as representative for the meteorological conditions over sea. Also for near surface temperatures, the already above mentioned frontal character can be seen clearly. Temperature values are substantially higher in the North-East of the frontal line than in the South-West. As this observance is based on a snapshot in time, a further study of wind fields will reveal more details about this frontal zone in section 4.3.

A meteorological variable that contains both temperature and moisture is the equivalent potential temperature Θ_e (eq. 2.8). High Θ_e values indicate warm and humid air, lower
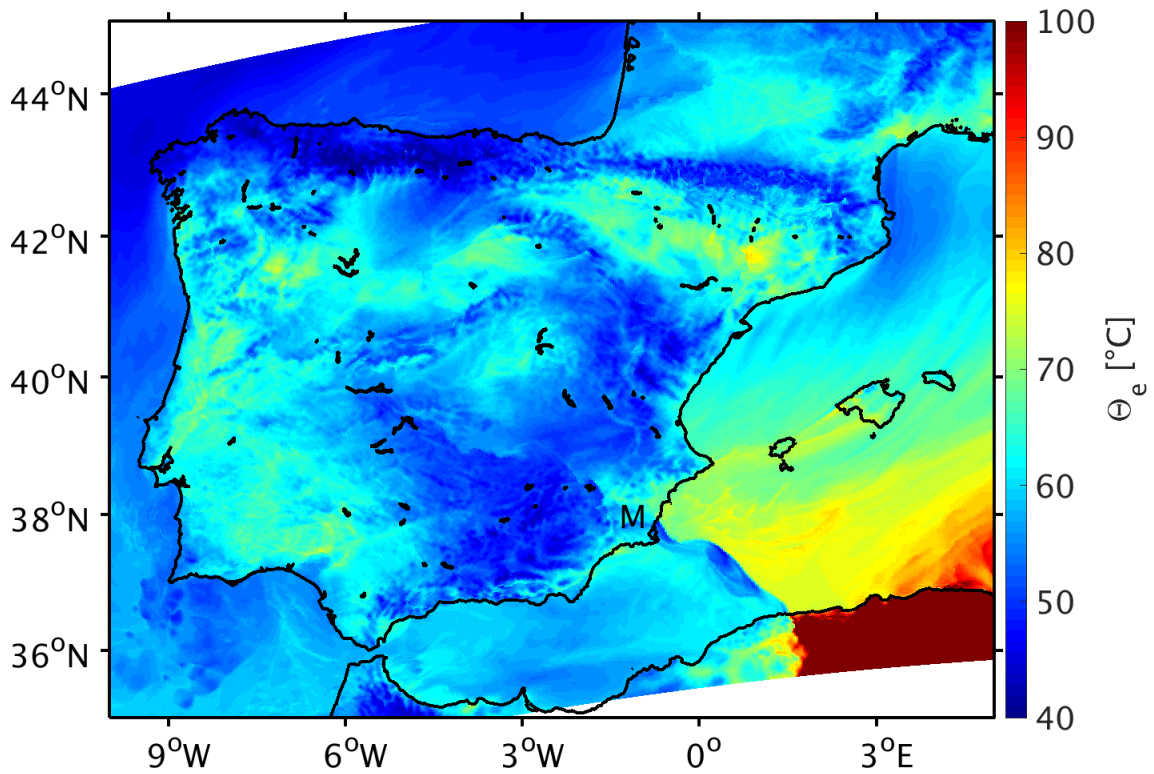
Figure 4.3: COSMO simulated surface equivalent potential temperature Θ_e [°C] on 28 September, 1500 UTC. Murcia is indicated by an "M".

Θ_e characterizes cooler and drier air. In the COSMO simulated horizontal Θ_e field of 28 September, 1500 UTC, the above mentioned frontal zone can be seen very clearly (Fig. 4.3). Warm and moist airmasses northeast of Murcia are indicating with Θ_e values of more than 75 °C a region with high potential instability. In the subsequent colder and drier air, southwest of the boundary line, potential for deep moist convection is consequently less pronounced. The strong horizontal moisture gradient of the frontal zone indicates a main characteristic of a "dryline" (e.g. Markowski and Richardson, 2010). Severe convection is often related to such systems (e.g. Ziegler and Rasmussen, 1998 or Roebber et al., 2002).

After the analysis of the spatial distribution of near-surface-level relative humidity and temperature, favorable zones for deep moist convection were detected. It can be concluded that suitable conditions with enough low-level moisture content and ability for latent heat release are given at the Spanish Mediterranean coastline in the region between Murcia and Valencia and from there outreaching over the Mediterranean Sea. In the following two sections, it is investigated how large the instability of the atmosphere is in these regions and where trigger mechanisms for the release of convection are available.
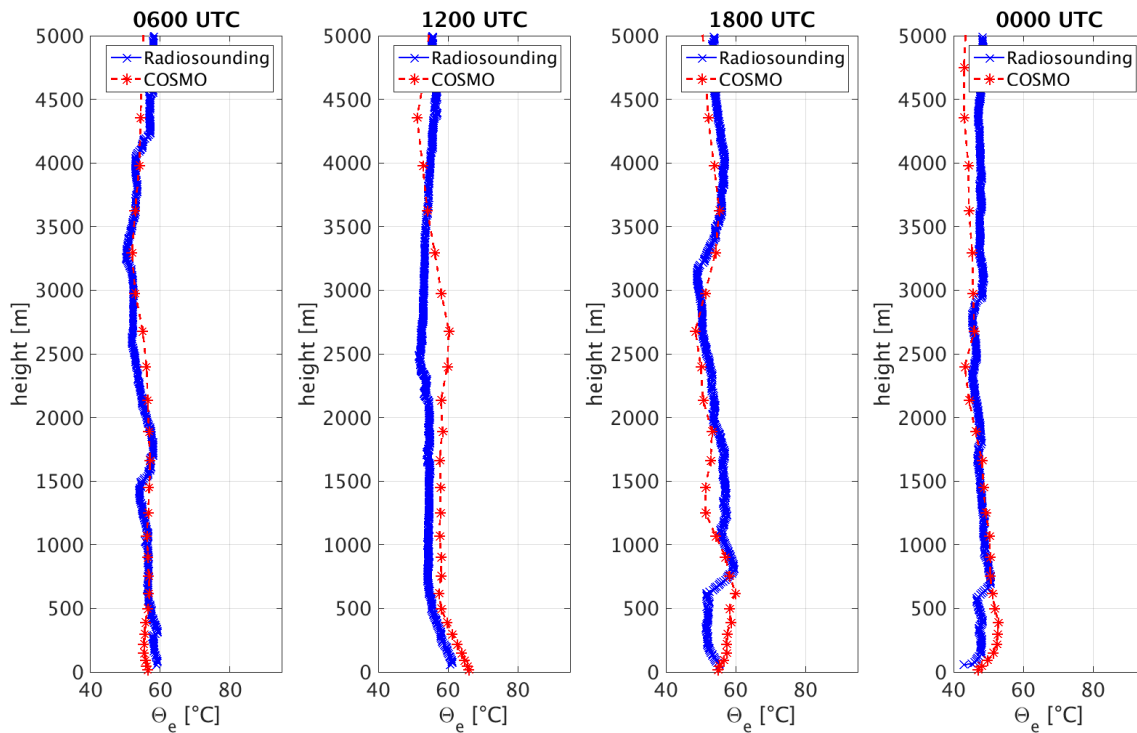
Figure 4.4: Θ_e profiles in Murcia derived from radiosounding data and from COSMO simulations. Profiles for 28 September at 0600 UTC, 1200 UTC, 1800 UTC and for 29 September at 0000 UTC are shown.

4.2 Atmospheric instability

Several measures exist for the description of instability. Convective indices, like convective available potential energy (eq. 2.5), the convective inhibition or the lifted index are widely used (e.g. Kunz, 2007). Here, vertical profiles of the equivalent potential temperature Θ_e (eq. 2.8), are used. For regions with $\frac{\mathrm{d}\Theta_e}{\mathrm{d}z} < 0$, instability is available. When the situation is - due to a certain barrier (e.g. an inversion layer) - only potentially unstable, convection has to be released by a trigger mechanism. To calculate the equivalent potential temperature at one point, values for temperature, pressure and relative humidity are necessary. For vertical profiles, these variables can be received from radiosoundings. In the area of interest, radiosoundings from Murcia, Palma de Mallorca and Barcelona were available every six hours. This high measurement frequency is a particularity of the HyMeX field campaign. For HyMeX IOP8, a total of 44 extra radiosondes were launched (Jansà et al., 2014a). The normal case is a time step of 12 h between two radiosoundings. As the interest of this work is driven by heavy precipitation events, only regions with potential for deep moist convection are studied in the following. Based on the results that sufficient low-level moisture is available in the regions around Murcia and Palma de Mallorca, several vertical Θ_e profiles were calculated from radiosounding data of those two stations (Figs. 4.4 and 4.5). In comparison to the radiosounding data, the profiles of the nearest gridpoints of the COSMO simulation are presented as well. For the following analysis, also associated raingauges measurements (Fig. 4.6) were taken into account.
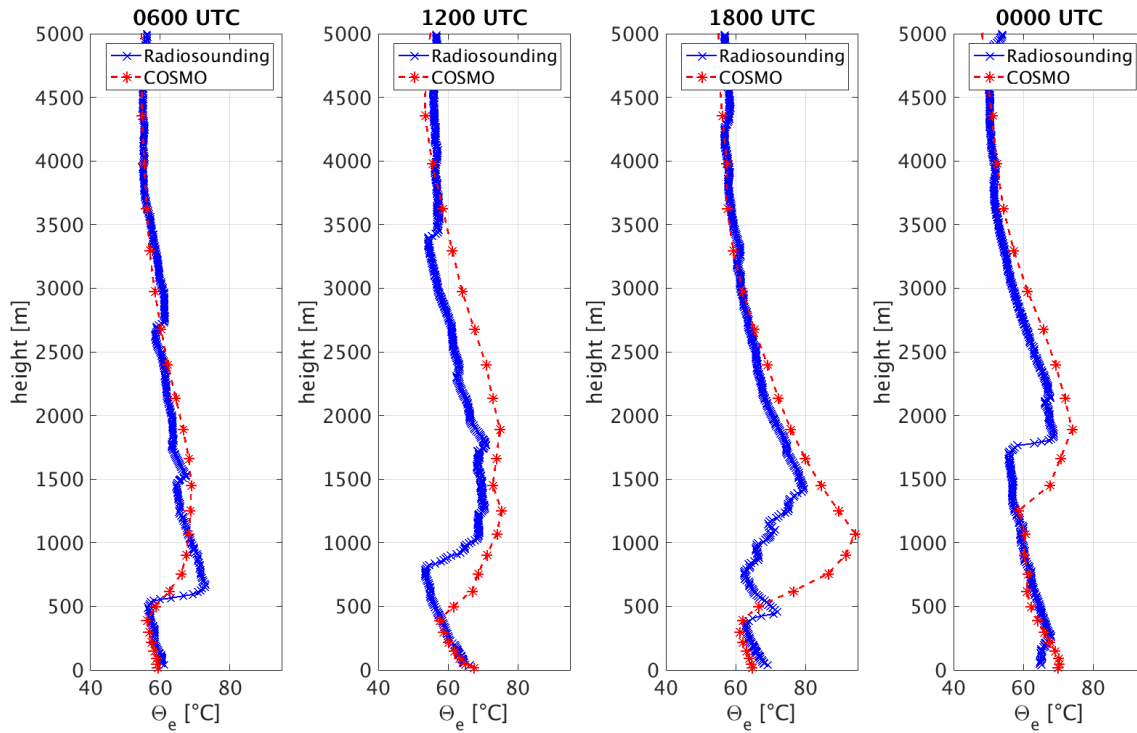
Figure 4.5: Θ_e profiles in Palma de Mallorca derived from radiosounding data and from COSMO simulations. Profiles for 28 September at 0600 UTC, 1200 UTC, 1800 UTC and for 29 September at 0000 UTC are shown.

The raingauges are located in the vicinity of the points where the radiosoundings were launched. In Murcia, the distance is approximately 100 m, in Palma approximately 8 km.

In Murcia, which is the most southern investigated location, measured and simulated Θ_e values reached 60 °C at 0600 UTC and at 1200 UTC at lowest level (Fig. 4.4, two left panels). In the course of these six hours, a slight low-level instability is created in both datasets. Above approximately 600 m, the relatively constant profiles indicate a neutral (up to approximately 2300 m) atmosphere. The Θ_e profiles at 1800 UTC (Fig. 4.4, third panel) shows a decrease of surface Θ_e values to around 55 °C and a no longer existent potential instability (except for lowest levels in the radiosounding data). Regarding the measured heavy rainfall amount of about 64 mm during these six hours (Fig. 4.6, blue bars), the cooling of the lower atmosphere can be explained through evaporation. A similar argumentation can be used for the COSMO simulated precipitation sum of about 23 mm in this time span (Fig. 4.6, cyan bars). The strong reduction of the atmospheric instability between 1200 UTC and 1800 UTC could be caused by various processes. If the rainfall resulted from convective activity, it can be assumed that the present instability at 1200 UTC was strengthened and then dissolved by a trigger mechanism. The released energy could result in deep convection and thus cause heavy rain. Due to the relatively steep orography west of Murcia (Fig. 2.1), it is supposed that deep moist convection and the resulting heavy precipitation could have been triggered by orographic lifting. But also lifting at the cold front of the surface low seems to be likely. Both hypotheses are inves-
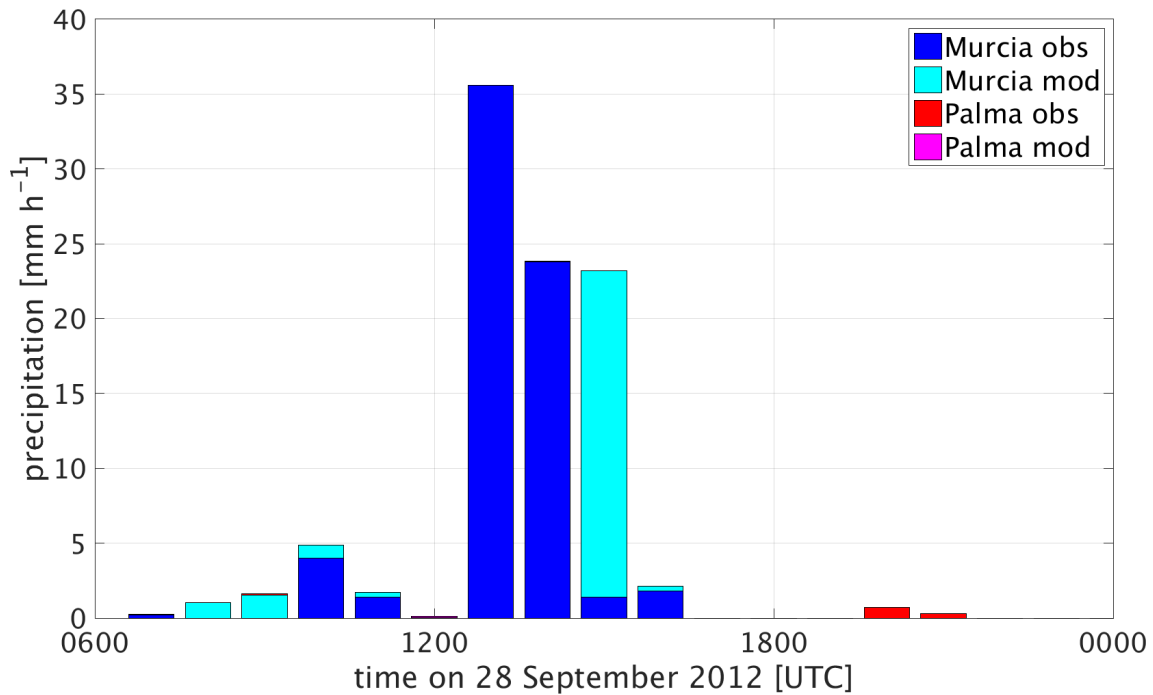
Figure 4.6: Measured and simulated 1 h accumulated precipitation sums in Murcia (blue and cyan) and Palma de Mallorca (red and magenta) from 28 September, 0600 UTC until 29 September, 0000 UTC.

tigated in more detail in sections 4.3 and 6.3. During the following evening hours, Θ_e values at low levels decreased down to near 40 °C in both datasets (Fig. 4.4, right). No further potential instability was created during this day.

Over Palma de Mallorca, where sufficient low-level moisture was available as well, the Θ_e profiles (Fig. 4.5) show much more variability compared to the situation in Murcia. Surface values at 0600 UTC (Fig. 4.5, left panel) reached 60 °C, but over a slightly unstable atmosphere, a strong inversion occurs in the 500 m up to 600 m layer. Here, Θ_e values increase up to almost 75 °C. Due to the inversion, the release of convection is prohibited for this timestep in this geographical region. Until the next time step at 1200 UTC (Fig. 4.5, second panel), surface Θ_e values increased to about 65 °C. The instability at lower levels extended up to approximately 800 m and was strengthened as well. Measured Θ_e values decrease with almost 1.25 °C per 100 m. Above, the inversion layer is still present. It reaches from 800 m up to 1000 m height and separates the strong potential instability at lower levels from a neutral atmosphere above. The COSMO simulated inversion zone is existent, but is located much lower than the measured one. Anyhow, the release of deep convection is inhibited for both datasets. This fact is also visible regarding the relatively weak large-scale vertical wind velocities over Palma at 1200 UTC (Fig. 2.2, middle left). Six hours later (Fig. 4.5, third panel), the ground level warmed up by another 5 °C. The unstable layer in lower levels is disturbed by a second inversion which is located in the radiosounding data at around 500 m height. Presumably it developed due to the sea breeze. The higher inversion layer is now more elongated and has a weaker

vertical gradient. The COSMO model misses this double inversion structure, but keeps and strengthens the already before existent vertical increase of Θ_e. Higher atmospheric layers between approximately 1500 m and 3000 m show an increased instability in both datasets. Until 0000 UTC on 29 September, the variability of the Θ_e profiles was reduced (Fig. 4.5, right panel). At lowest levels, the potential instability was transformed into a stable atmosphere. A possible mechanism for this development could have been the cold and dry land breeze. The prior low-level inversion was resolved. Above, the measured strong inversion layer is still present at around 1800 m. COSMO starts this inversion already at around 1300 m. Thus, deep convection is still inhibited for both datasets. Shallow convection could have been one reason for the 2 mm of rain, measured in Palma between 1900 UTC and 2200 UTC (Fig. 4.6, red bars).

In summary, the study of the atmospheric instability at two distinct radiosounding stations revealed strong differences within the area of interest. Enormous precipitation amounts in Murcia were correlated with a slightly unstable atmosphere. Hypotheses for involved trigger mechanisms are studied in the next section. Around Palma de Mallorca, relatively strong negative vertical gradients of Θ_e were capped by an inversion layer in 500 m to 1800 m height. Thus, the stimulation of heavy precipitation was inhibited in this region. Based on numerical studies, a more general investigation of the atmospheric stability is given in section 6.2.

4.3 Predominant lifting mechanisms

When enough moisture is available in the lower troposphere and in the presence of potential instability, a trigger mechanism can lift an air parcel above the level of free convection (sec. 2.1) and moist convection can occur. This can be conducted by e.g. orographic lifting or smaller-scale processes, like horizontal wind convergences. Favorable for the release of potential instability and deep convection are mesoscale lifting processes embedded in a zone with large-scale lifting.

One possibility to visualize the large-scale environment is to use numerical model analysis data, in which measurements are assimilated. As described in section 2.2.1, the combination of the cut-off low over Portugal together with a corresponding surface low led to significant synoptic-scale uplift. After the ω-equation (eq. 2.1), one part of the upward motion resulted here from the positive vorticity advection in front of the cut-off low in higher levels (Fig. 2.2, top). The other part is due to warm air advection in lower levels (Fig. 2.2, middle right), triggered by the surface low. Especially at its frontal zones, the baroclinic character led to significant synoptic uplift in the order of more than $40 \, hPa \, h^{-1}$ (Fig. 2.2, middle left), thus of approximately 2500 m in 6 h. Therefore, the large-scale environment already offered suitable thermodynamical conditions for an intense convective activity.
Embedded lifting in small- or mesoscale regions can take place for example at mountainous regions. In the area of interest, the topography of the western Mediterranean region is pronounced especially at the coastlines (Fig. 2.1). Hill slopes and terraces between 400 m
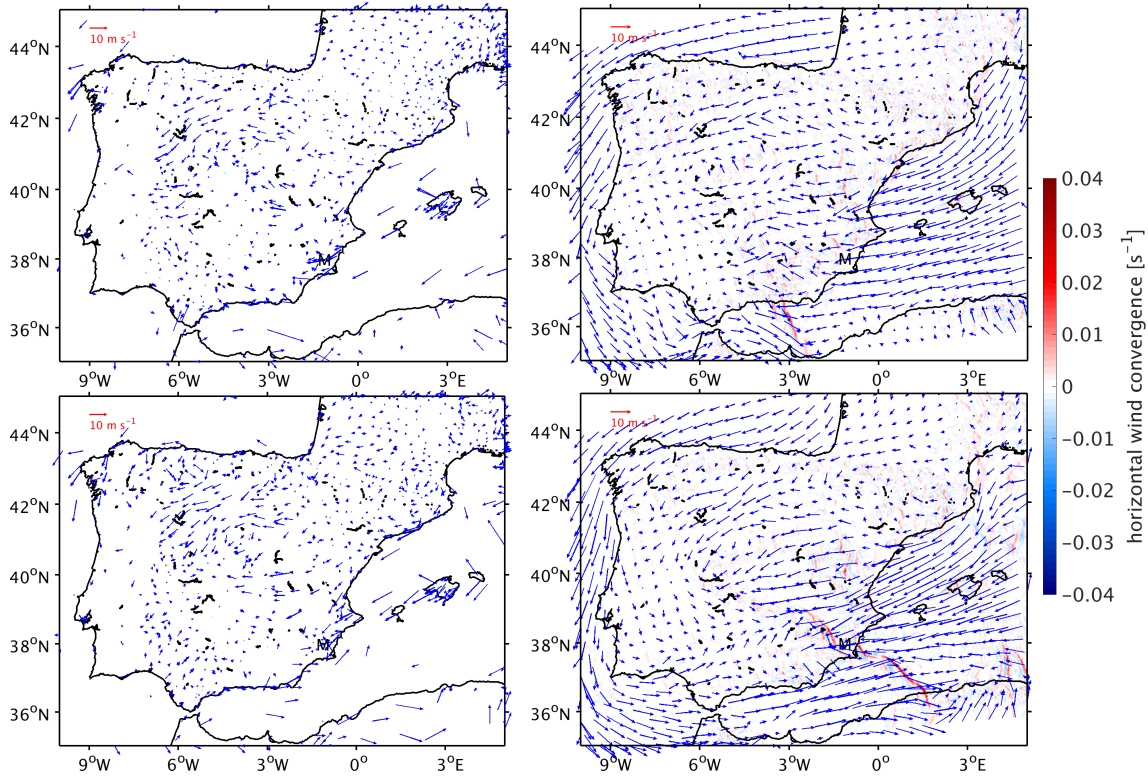
Figure 4.7: Horizontal wind fields in 10 m height on 28 September 2012, 0900 UTC (top) and on 28 September 2012, 1500 UTC (bottom). Murcia is indicated by an "M". Left: observed wind at surface stations. Right: simulated COSMO wind field (arrows) and simulated COSMO horizontal wind convergence (colored).

and 1000 m height exist at large parts along the Spanish Mediterranean coast. Large orographic contrasts between the sea and the surrounding topography are not rare. Most interesting for the triggering of deep convection near Murcia is the "Sistema Penibetico". This mountain range is aligned in a southwestern to northeastern direction and reaches from the southern tip of the Iberian Peninsula towards Valencia (Fig. 2.1). Murcia, where enormous precipitation amounts were measured (Fig. 4.6), is located in an area favorable for orographic lifting. If a supercritical inflow (eq. 2.9) arrives from the Mediterranean Sea, the air is blocked by the Sistema Penibetico and has to rise. As the horizontal wind velocity of the incoming flow is decelerated by this process, the lifting area can be located reasonably near Murcia.

To study the predominant wind conditions during HyMeX IOP8, the wind field, measured by synoptic stations in the area, is investigated at two distinct time steps (Fig. 4.7, left). Isochronically with the situation at 0900 UTC (Fig. 4.7, top), a first precipitation peak occurred at the station in Murcia (Fig. 4.6, blue bars). The wind field in the environment of the station is governed mainly by easterly (maritime) wind directions. Within this situation, warm and moist air from the Mediterranean Sea is brought towards the above mentioned Sistema Penibetico, where it has to rise. Thus, the wind field together with the surrounding topography indicates classical orographic lifting in this area. Also the COSMO simulation supports this hypothesis (Fig. 4.7, right). At the second time step at 1500 UTC (Fig. 4.7, bottom right), the wind directions near Murcia are still affected by

easterly winds. But also wind directions from west were measured in the vicinity. The converging of two different air masses can be supposed.

In section 2.1.3, the lifting through a horizontal wind convergence was introduced. If this was the case here, a superposition of three lifting mechanisms took place: large-scale lifting and embedded orographic lifting as well as additionally lifting through a low-level horizontal wind convergence. This hypothesis of the interaction of various processes is also supported by the COSMO simulation. Additional to the wind field, also the horizontal wind convergence was calculated with COSMO. Very obvious at 1500 UTC is a line of horizontal wind convergence reaching from northwest of Murcia over the Mediterranean Sea towards the Algerian coast (Fig. 4.7, bottom right). At this line, westerly winds coming from the Strait of Gibraltar are converging with easterly winds, coming from the Mediterranean Sea. Both airmasses were passing over the warm sea surface of the Mediterranean Sea, evaporation took place and thus a large amount of latent heat is transferred to the lower atmosphere. Regarding the time step at 0900 UTC (Fig. 4.7, top right), the convergence line was already existing in the morning hours. Then, the line was reaching from east of Malaga towards the coast of Morocco. A displacement velocity of about $60\,\mathrm{km\,h^{-1}}$ can be estimated. Regarding the 24 h accumulated precipitation sum of 28 September 2012 (Fig. 2.2, bottom left), this convergence line could thus also explain the large precipitation amounts at the southern Spanish Mediterranean coast.

Summary

Within this chapter, the preconditions for the deep moist convection during HyMeX IOP8 were studied. Based on observational data from the HyMeX measurement campaign and on simulated data from the numerical weather prediction model COSMO, surface moisture and temperature, data from vertical radiosoundings and low-level horizontal wind fields were analyzed. Especially at the Spanish Mediterranean coast and from there outreaching over the Mediterranean Sea, large regions with warm and moist airmasses, indicating high low-level potential instability, were present. Regarding the upper levels, the synoptic conditions favored large-scale lifting through an approaching cut-off low with positive vorticity advection and through a surface low with warm air advection ahead. Whereas potential instability could be released in Murcia, the conditionally unstable situation in Palma de Mallorca was blocked by a strong inversion zone in the mid-troposphere. Concerning the heavy precipitation, measured and simulated at Murcia, two different trigger mechanisms were found to be likely. On the one hand, a horizontal moisture convergence line was detected in the surface level. On the other hand, the relatively steep orography in the surrounding is allegedly interacting with the horizontal low-level flow, arriving from the moist and warm Mediterranean Sea.

The precise role of those two lifting mechanisms are studied more detailed by means of numerical simulations in chapter 6.

5 Evaluation of precipitation and radar reflectivity fields

In the previous chapter, the preconditions for deep convection during HyMeX IOP8 were investigated at distinct points and at specific time steps in the area of interest. Here, the focus lies on the resulting precipitation rates, which are available on spatially and temporally high resolved fields. Studies for the fields in the complete area of interest and for continuative time periods are performed.

Three available precipitation data sets for HyMeX IOP8 are investigated in the first part of this chapter: surface raingauges measurements, satellite derived precipitation data and the precipitation output of the French AROME-WMED model (sec. 3.2.1). The raingauge data, which intend to have the smallest measurement errors, are available only over land and only for distinct point. In contrast, the satellite derived precipitation, which tends to have a higher degree of uncertainty, is available as well over the Mediterranean Sea. The AROME-WMED data are the output of a numerical model, which was designed specifically for the HyMeX project and for which extra measurement data from the field campaign were assimilated. The fine horizontal resolution and the complete coverage over the whole area of interest, are the two main advantages of this dataset.

The second part of this chapter analyzes measured radar reflectivity, which is linked to the measured precipitation. With a large radar data availability over the Mediterranean Sea, a statement about the heavy precipitation areas during HyMeX IOP8 can be deduced for the whole area of investigation.

The analysis of the introduced data sets is compared with the COSMO simulation used already in chapter 4. For the evaluation of the results gained with the spatial verification measure SAL (sec. 3.3.4), an earlier initialized COSMO simulation was additionally taken into account. The earlier initial conditions led to a different development of the resulting precipitation fields. Regarding the longer forecast duration of this second COSMO simulation, the representativeness of the heavy precipitation is expected worse than in the reference simulation.

5.1 Precipitation

The most important prediction variable for a heavy rainfall event is - naturally - the precipitation. This meteorological quantity is a consequence of specific atmospheric conditions, which were addressed in chapter 4. Here, the resulting precipitation fields during
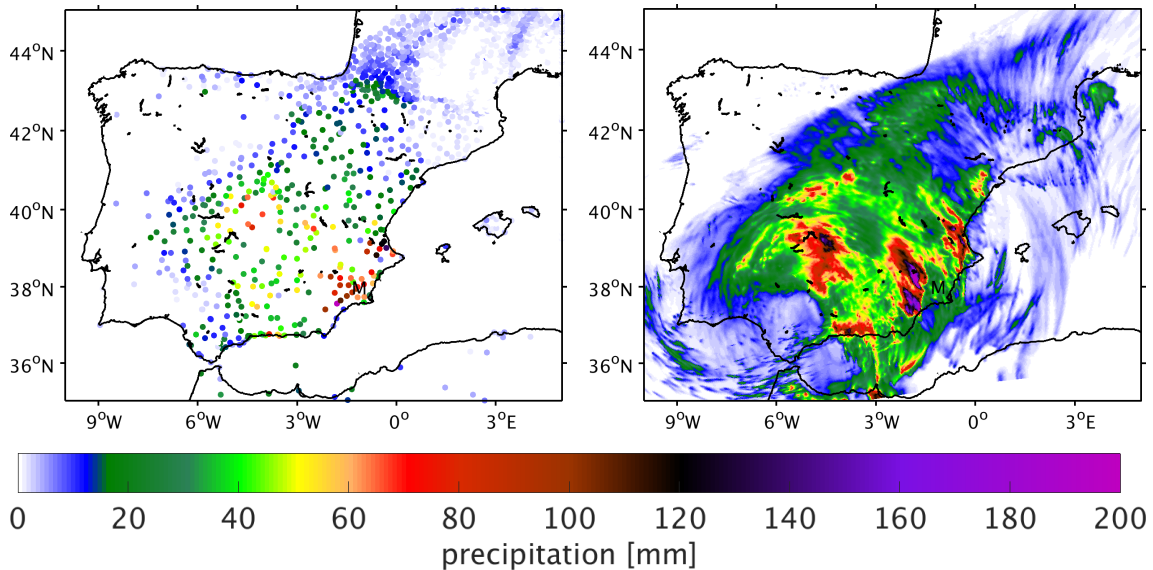
Figure 5.1: Left: Observed 24-hourly rainfall amount from 28 September at 0600 UTC to 29 September at 0600 UTC. Murcia is indicated by an "M". Right: Simulated COSMO 24-hourly rainfall amount from 28 September at 0600 UTC to 29 September at 0600 UTC.

HyMeX IOP8 are investigated. Therefore, three data sets for the precipitation are studied. Beginning with raingauge measurements from surface stations, also satellite derived precipitation data and the result of a numerical model are analyzed in the following.

5.1.1 Raingauges

With the raingauge network, considerable rainfall amounts of $40\,\mathrm{mm}\,24\mathrm{h}^{-1}$ to $70\,\mathrm{mm}\,24\mathrm{h}^{-1}$ were measured between 28 September, 0600 UTC and 29 September, 0600 UTC in Central Spain (Fig. 5.1, left). Along the Spanish Mediterranean coast even higher values were registered. Especially the regions around Murcia and Valencia show heavy precipitation values with several measurements above $120\,\mathrm{mm}\,24\mathrm{h}^{-1}$. The highest rainfall amount with approximately $200\,\mathrm{mm}\,24\mathrm{h}^{-1}$ was measured southwesterly of Murcia. These observations reflect the results which were obtained in chapter 4. In the region around Murcia, where enough atmospheric moisture was available, heavy precipitation occurred presumably due to significant upward motion through the interaction of orographic lifting and a horizontal wind convergence line. Despite available potential instability at Palma de Mallorca, this area remained almost dry, due to a missing trigger mechanism.

As for the previous chapter, the numerical output of a COSMO simulation, which was initialized on 28 September, 0600 UTC, is compared to the surface station measurements. An overall good agreement of simulated 24 h accumulated precipitation amount with the measurements of raingauges can be observed (Fig. 5.1, right). The highest precipitation sums can be remarked around Valencia, Murcia and in the center of Spain in both datasets. Magnitudes range up to $200\,\mathrm{mm}\,24\mathrm{h}^{-1}$ in the similar areas and the extension of the precipitation area covers similar geographical regions. The rainfall amounts at the
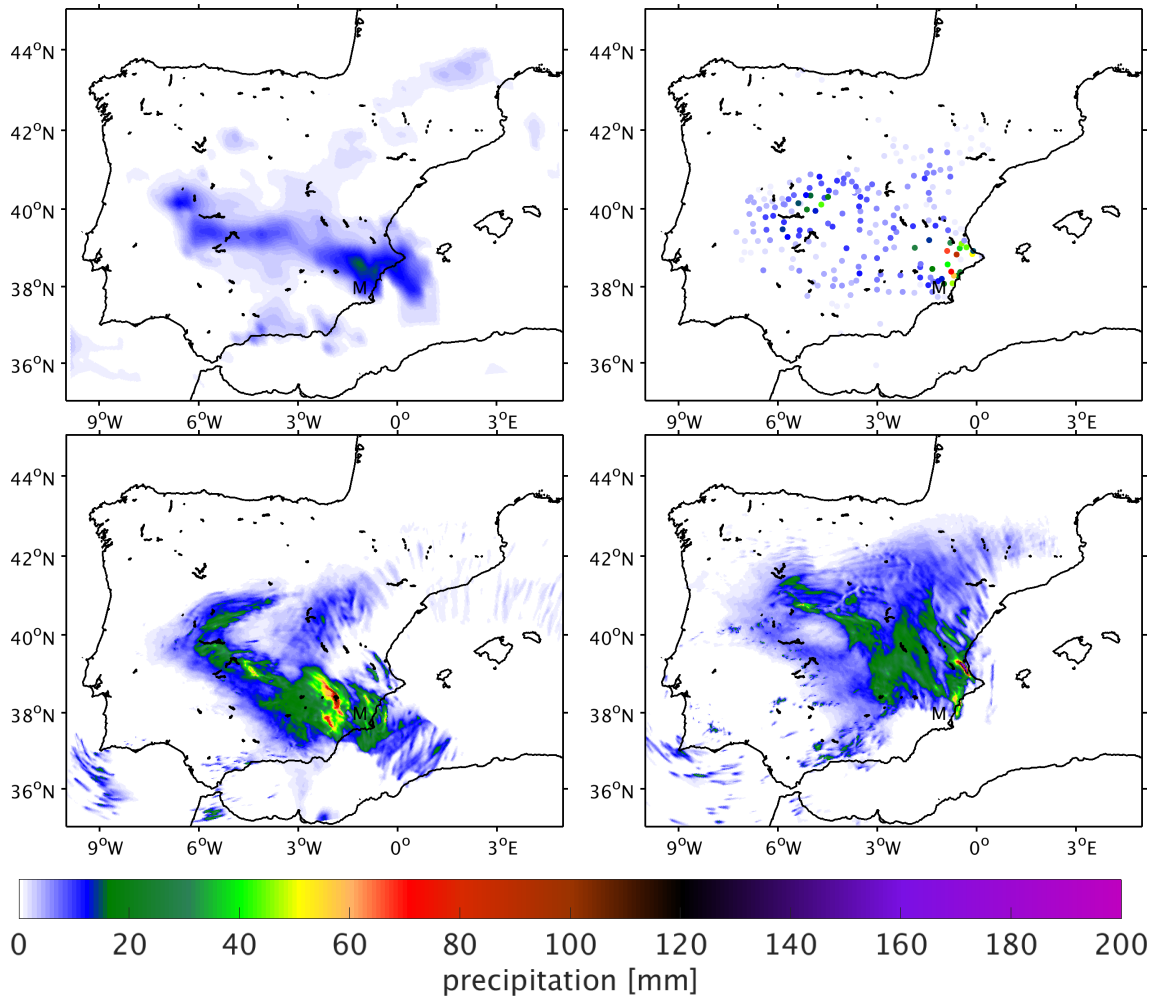
Figure 5.2: Top left: TRMM 3-hourly rainfall amount from 28 September at 1330 UTC to 1630 UTC. Top right: Raingauges derived 3-hourly rainfall amount from 28 September at 1400 UTC to 1700 UTC. Bottom: Simulated COSMO 3-hourly rainfall amount from 28 September at 1400 UTC to 1700 UTC initialized on 28 September 2012, 0600 UTC (left) and on 27 September 2012, 1200 UTC (right). Murcia is indicated by an "M".

southern Mediterranean coast are higher in the model than given by the measurements of the raingauge stations. Around Murcia, the area of simulated heavy precipitation is shifted westwards compared to the measurements. Overall it is assumed that the chosen COSMO simulation may be a suitable representation to describe the heavy precipitation occurred during HyMeX IOP8.

5.1.2 Satellite derived precipitation

One disadvantage of the above discussed surface stations is the absence of measurements over the Mediterranean Sea. An extrapolation of raingauge data on the whole model grid would be a theoretical method to overcome the empty spaces between the stations. To
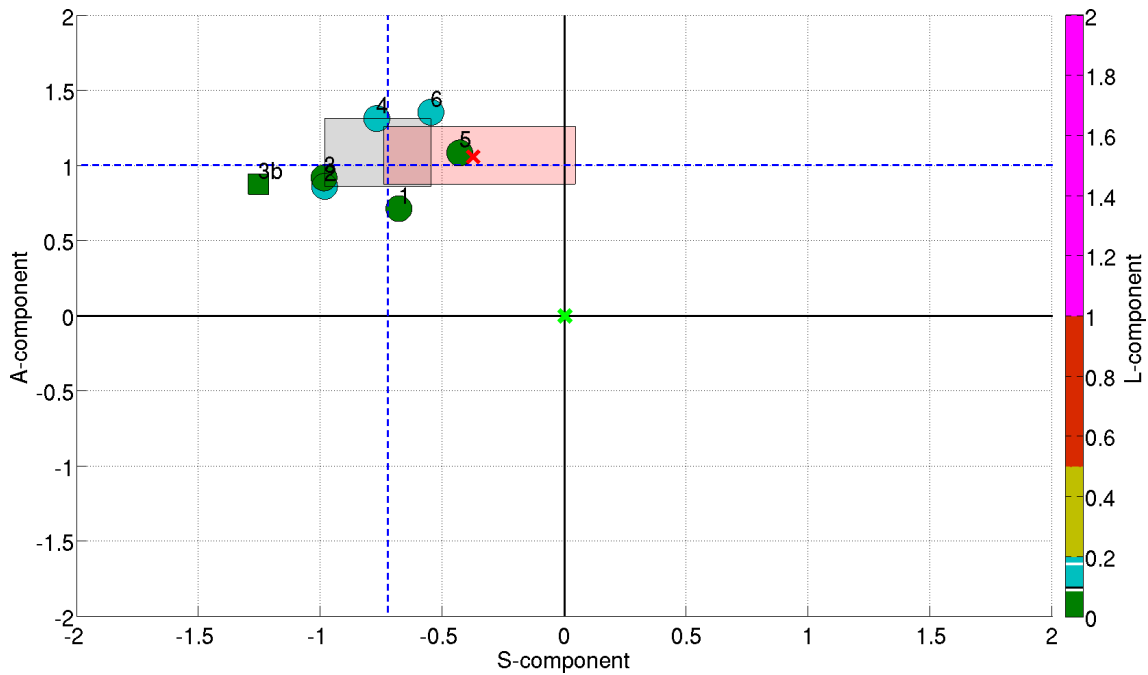
Figure 5.3: SAL plot for the intercomparison of the observed TRMM precipitation amount with the simulated values from the COSMO run initialized on 28 September at 0600 UTC. The six 3-hourly starting times of 28 September 2012 from 0730 UTC (respectively 0800 UTC) until 2230 UTC (respectively 2300 UTC) are shown. The spatial comparison between a COSMO simulation, initialized on 27 September 1200 UTC, and the satellite derived precipitation field is represented by the intersection point of the associated median values of S and A (red cross) and interquartile ranges (light red rectangle). The specific spatial comparison between 1400 UTC and 1700 UTC for the earlier initialized COSMO simulation is marked with the green square.

apply this method, the station density has to be large enough to sample the spatial variability of the field. For the case of precipitation, this spatial variability is high, and so the required density is high. Over the Spanish mainland, the distribution of the raingauges could be dense enough for such a calculation. But over the Mediterranean Sea, large artifacts would occur. Due to the extrapolation of land measurements over the sea, the precipitation field would be blurred in an unrealistic way. So, it is not useful to employ such an extrapolation method for the verification of model data regarding precipitation over the Mediterranean Sea.

Another possibility to obtain precipitation data over the Sea are satellite derived precipitation estimates. Therefore, data from the "Tropical Rainfall Measuring Mission" (TRMM) were used here. This satellite mission was first proposed by Simpson et al. (1988) and was launched end of 1997. The TRMM rain product "3B42", used here, is based on multiple satellite microwave and infrared measurements (Mehta and Yang, 2008). The spatial resolution of those data is given by $\Delta x = \Delta y \approx 0.25°$. As the name already indicates, the focus of the satellite mission lies in tropical regions. Nevertheless, TRMM data were used also in other studies for the western Mediterranean area, with latitudes higher than $26°$ N (e.g. Khodayar et al., 2015). TRMM derived precipitation intensity in higher latitudes is generally underestimated (Kidd et al., 2012). This feature of TRMM data can be seen

clearly for the peak of the heavy precipitation event of HyMeX IOP8 (Fig. 5.2, top left). While precipitation sums over 80 mm in three hours were measured at the raingauge stations, TRMM data reach only values of around 20 mm in the similar time period. At least, the structure of the precipitation area has a similar shape in the remote sensing and the in-situ measurement setting. Highest precipitation values were measured in both cases near the coast between Murcia and Valencia. Lighter rain occurred at central Spain between approximately $7°$ W and $0°$ W and between $37°$ N and $41°$ N, respectively.

Like in the previous section, the numerical simulation with COSMO (Fig. 5.2, bottom left) is used for a comparison with the observed TRMM and raingauges data (Fig. 5.2, top). As expected, the 3-hourly rainfall accumulation between 1400 UTC and 1700 UTC is generally much higher than in the TRMM-data, but almost agrees with the intensity of the precipitation maxima measured by the raingauge stations. Regarding the shape of the precipitation area, COSMO seems to capture the output of the TRMM-data well. As well as the spatial extension over land, even the prolongation over the Mediterranean Sea is existent in those two data sets.

To investigate this good correlation in more detail, the spatial verification method SAL (section 3.3.4) was deployed. For that, the TRMM data were interpolated to the model grid of the COSMO simulation. Afterwards, the SAL method was used for six different 3-hourly time periods. Regarding the TRMM data, the first period started on 28 September 2012 at 0730 UTC, the last one at 2230 UTC. As the output for the COSMO simulation is only available at every full hour, the associated starting times for the time periods lie for this data set between 0800 UTC and 2300 UTC. In Figure 5.3, the SAL plot (reference Figure 3.7) for this comparison is shown. Overall speaking, the median S-value (eq. 3.18) is given by -0.73. This value indicates smaller precipitation patterns in the COSMO simulation than in the TRMM dataset. Presumably this is due to the finer scale structure in the COSMO simulation. Due to a ten times smaller horizontal gridspacing of $0.025°$, more small-scale precipitation areas are found in the COSMO data. In contrast, the TRMM dataset consists of less but larger precipitation patterns. Regarding the A-component (eq. 3.19), its median value is given by 1.00. That means that higher precipitation amounts were simulated by COSMO than derived by the satellite data. This result is consistent with the above mentioned characteristic of TRMM data in high latitudes. Regarding the interquartile ranges of S- and A-components, they are given by 0.44 and 0.45 (Fig. 5.3, gray rectangle). This description is generally valid for all investigated time periods (single dots in Fig. 5.3). The median of the location component (eq. 3.20) is 0.10. With the colorbar, defined by Zimmer and Wernli (2011), as basis, this value lies between the first and the second (from five) quality step and implicates thus a very good skill. The spatial comparison of simulated 3 hourly precipitation amount between 1400 UTC and 1700 UTC with the associated TRMM data (Fig. 5.2, left panels), is shown by the dot with the number "3" in Figure 5.3.

To better understand the discussed SAL-components, the satellite derived precipitation was not only compared to the above used COSMO run, but also to a second simulation. Almost all settings for the numerical simulation were chosen equally to the prior presented simulation. The only difference is the initialization time, which was now set on 27 September 2012, 1200 UTC. The offset of 18 h between the two simulations provides the possibility to investigate a simulation with longer lead time with respect to the peak of
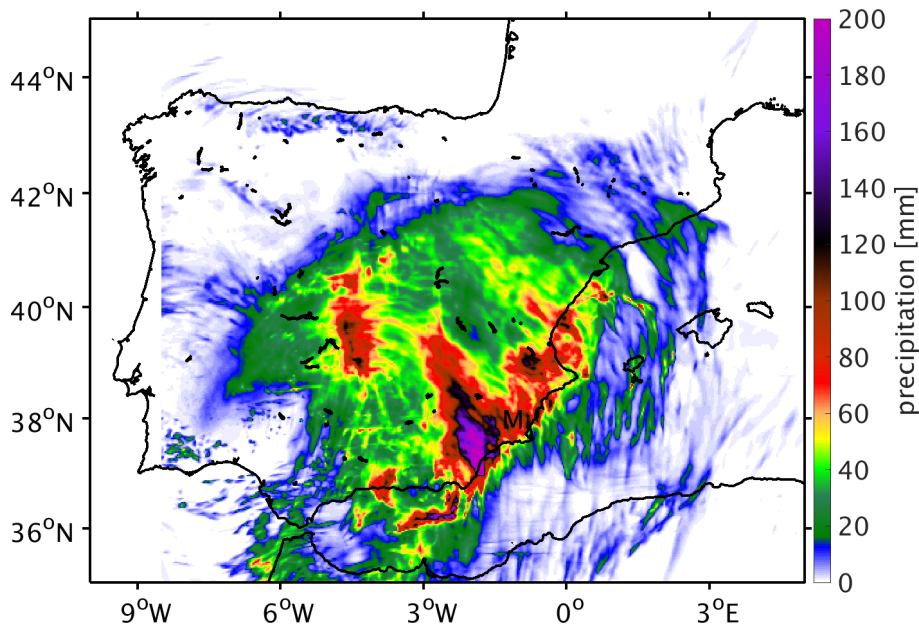
Figure 5.4: AROME-WMED simulated 24-hourly rainfall amount from 28 September at 0600 UTC to 29 September at 0600 UTC. Murcia is indicated by an "M".

the heavy precipitation event. Thus, a varied precipitation field results (Fig. 5.2, bottom right). For the shown time period, the maximum intensities of the raingauge measurements are captured, but most of them are simulated further north. The overall structure of the precipitation field compared to the TRMM output appears too broad. In addition, no extension of the precipitation over the sea surface can be seen. Especially the convergence line, indicated by a slope precipitation pattern over the sea in the COSMO simulation with shorter lead time, is not captured in this simulation. This leads to the assumption that the S-component for this time span has to be much larger in this case. The A-component should not differ too much from the comparison with the later initialized COSMO simulation. Both hypothesis are fulfilled: The values for S and A are -1.26 (compared to -0.99) and 0.88 (compared to 0.92) (Fig. 5.3, square with the number "3b"). The overall spatial comparison of six 3 hourly time periods between the earlier initialized COSMO simulation and the satellite derived precipitation field seem to result in a better (values closer to zero) score for the earlier initialized simulation (Fig. 5.3, red cross and light red rectangle). But the relatively "good" median S-value is qualified by the fact that the spread of S of the earlier initialized run is, with an interquartile range of 0.79, much higher compared to the value of the later initialized simulation. Thus, a higher variability exists regarding the single-hour quality of the structure component.

5.1.3 AROME-WMED precipitation

In the two sections before, precipitation fields derived from raingauges and from satellite measurements were discussed and compared with COSMO simulations. Both methods have their own advantages and disadvantages. Whereas the surface stations provide high
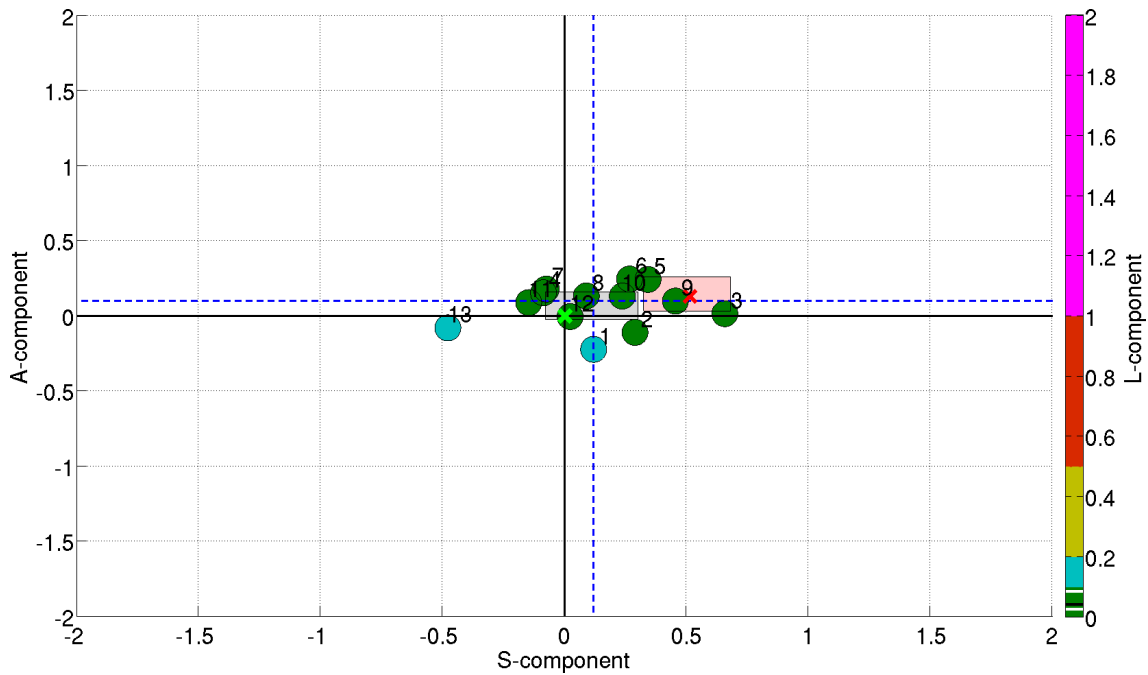
Figure 5.5: SAL plot for the intercomparison of AROME-WMED precipitation fields with the associated fields from the COSMO run. Both models are initialized on 28 September at 0600 UTC. The hourly time steps of 28 September 2012 from 0800 UTC until 2000 UTC are shown. The spatial comparison between the earlier initialized COSMO simulation and the AROME-WMED precipitation field is represented by the intersection point of the associated median values of S and A (red cross) and interquartile ranges (light red rectangle).

resolution data over land only, the coarser resolved and too less intensive TRMM data allows also an investigation over the Mediterranean Sea. A numerical model can combine the benefits of both methods. To get an impression how well COSMO represents the rainfall amount in the whole area of investigation, the simulation output is compared with a second NWP model. Therefore, the French AROME-WMED model (section 3.2.1) is used. It was developed in the scope of the HyMeX project (section 2.2.1) and provides the assimilation of several additional observations from the associated field campaign. The AROME-WMED model area is overlapping the COSMO model area over central Spain and a part of the western Mediterranean Sea (Fig. 3.3 left and Fig. 3.5). To validate the two NWP models spatially against each other, the AROME-WMED model, which has a horizontal grid spacing of $\Delta x = 2.5\,\mathrm{km}$, was interpolated to the COSMO grid, which has a horizontal resolution of $\Delta x \approx 2.8\,\mathrm{km}$. Due to the similar horizontal grid spacing, only small interpolation errors occur.

Compared to the associated surface station measurements (Fig. 5.1, left), the overall structure of the simulated 24-hourly accumulated precipitation field from 28 September, 0600 UTC to 29 September, 0600 UTC, provided by AROME-WMED (Fig. 5.4) is similar. Even if AROME-WMED simulated higher rainfall maxima than measured by the raingauges, they are located in the same region around Murcia. The local maxima near Valencia, at the southern coast and in the Spanish mainland are represented as well in the
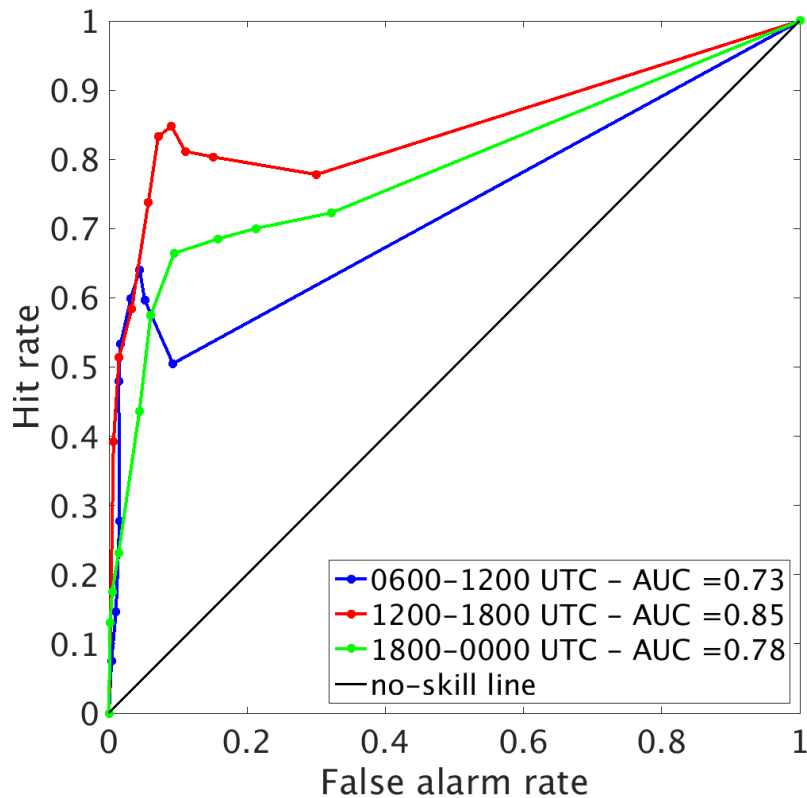
Figure 5.6: ROC curves for the intercomparison of AROME-WMED precipitation fields with the associated fields from the COSMO run. Both models are initialized on 28 September at 0600 UTC. The 6-hourly starting times of 28 September 2012 from 0600 UTC to 1800 UTC are shown. Precipitation thresholds for 6 hourly accumulated precipitation were chosen as 0.1 mm, 1 mm, 2 mm, 5 mm, 10 mm, 15 mm, 25 mm, 35 mm and 50 mm.

model output. A more objective comparison can be achieved via the calculation of basic verification scores (sec. 3.3.2) between the COSMO and the AROME-WMED model field. For the 24 h accumulated rainfall amount, a mean error (eq. 3.12) of $-0.9\,\mathrm{mm}\,24\mathrm{h}^{-1}$ indicates a slightly more intense mean precipitation in the AROME-WMED dataset. The associated RMSE (eq. 3.13) is given by $15.7\,\mathrm{mm}\,24\mathrm{h}^{-1}$. Regarding the agreement of the structure of both precipitation fields, a correlation coefficient (eq. 3.14) of 0.7 indicates a good accordance. With those interpretations, the precipitation output of the AROME-WMED model is taken as suitable for a spatial verification with the associated output of the COSMO model.

To perform a spatial verification of both numerical models, the SAL method (section 3.3.4) was used again. Resulting from an hourly comparison of the simulated precipitation fields between 0800 UTC and 2000 UTC from the two models, median values of the structure and the amplitude components are slightly positive (0.12 and 0.10) (Fig. 5.5). This means that COSMO simulated on average slightly larger and stronger precipitation patterns than AROME-WMED. The median value of the location component is almost zero and indicates only small differences in the dispersion of the two simulated precipi-

tation fields. To better evaluate those scores, the prediction of AROME-WMED is also compared against an earlier initialized COSMO run. With the simulation initialized on 27 September, 1200 UTC, a worse SAL score results. The corresponding median value of S (0.51) is significantly larger than for the before analyzed simulation and shows again that the earlier initialized COSMO run produces broader precipitation fields (Fig. 5.5, red cross). The median value of the A-component (0.13) does not differ significantly from the value of the later initialized simulation. With an almost equally broad interquartile range of structure and amplitude components (Fig. 5.5, light red rectangle), it is concluded that only the single values of the structure component are shifted towards larger values for the earlier initialized simulation.

A further verification method which is applied here, is the analysis of ROC curves (section 3.3.3). For each grid point of the simulated COSMO and AROME-WMED precipitation fields, hit rate (eq. 3.15) and false alarm rate (3.16) are calculated for a pre-defined rainfall threshold value. The larger the area under the resulting curve (AUC: eq. 3.17) is, the more hits and the less false alarms were produced.
Between 0600 UTC and 1200 UTC on 28 September 2012, a value of AUC $= 0.73$ results (Fig. 5.6, blue curve). This index is increasing to 0.85 for the following next six hours (Fig. 5.6, red curve). There, hit rates of more than 83% and false alarm rates of less than 10% were reached for all precipitation amounts $>= 10\,\mathrm{mm}\,6\mathrm{h}^{-1}$. This result is very satisfying as the highest rainfall amount was measured during this time period. For the next six hours, the AUC decreases slightly to 0.78, but still describes a suitable accordance between COSMO and AROME-WMED model results (Fig. 5.6, green curve).

5.2 Radar Reflectivity

A meteorological variable which is strongly linked to precipitation is the radar reflectivity Z. Dependent on the type of precipitation, a relationship can be estimated between Z and the rate of rainfall R. A frequently applied relationship is:

$$Z = a \cdot R^b \tag{5.1}$$

where the parameters a and b have to be determined with measurements. Thus, this equation is empirical and very variable. Errors can occur due to ground clutter effects and the measurement height. Depending on the particle size, different parameters a and b result. After Marshall and Palmer (1948), it is for stratiform rain events: $Z = 296 \cdot R^{1.47}$. For convective events, the relation $Z = 300 \cdot R^{1.35}$ (Sekhon and Srivastava, 1971) can be used. Values of Z are usually given in the logarithmic unit dBZ. It is: $\mathrm{dBZ} = 10\log Z$ with the radar reflectivity given in $\mathrm{mm}^6\,\mathrm{m}^{-3}$ (e.g. Houze, 1993). In moderate to heavy rain, values typically reach 30 dBZ to 60 dBZ. Huge advantages of radar systems are their high spatial resolution and their wide range of $> 100\,\mathrm{km}$. Thus, a coastal radar station can receive data from over the Sea surface, where no surface stations are available. By a combination
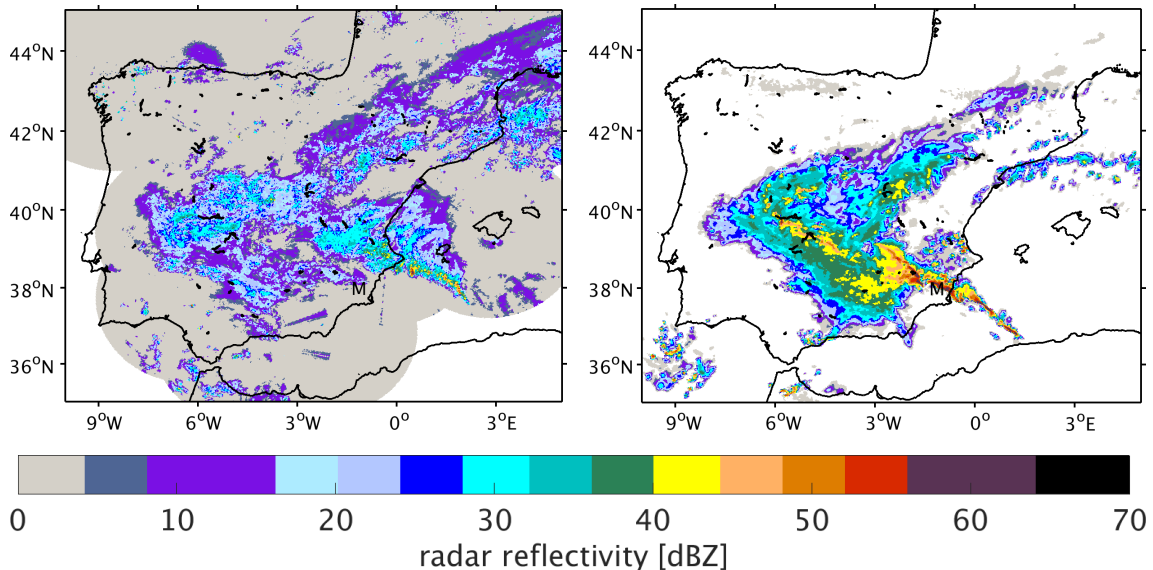
Figure 5.7: Radar reflectivity on 28 September 2012, 1500 UTC. Murcia is indicated by an "M". Left: Observed values. Right: COSMO simulated values. The model was initialized at 28 September 2012, 0600 UTC.

of radar estimated precipitation and measurements from raingauges, a combined dataset can be gained (e.g. Wüest et al., 2010). For this work, the pure radar reflectivity is used in comparison to the COSMO model simulated reflectivity.

For the western Mediterranean, several radar systems are available. Summarized in an European composite, a large coverage of measurement data results also over parts of the Mediterranean Sea. During HyMeX IOP8, highest radar reflectivity values were measured on 28 September, 1500 UTC (Fig. 5.7, left). This is the time step where the surface convergence line, studied in chapter 4, was most pronounced (Figs. 4.1, 4.2 and 4.7, bottom). Similar to the precipitation fields, described in section 5.1, reflectivity was detected in large parts of the Spanish mainland as well as concentrated at some locations at the Mediterranean coast. In the offshore region between Murcia and Valencia, values up to 60 dBZ were measured. Prominent is again the linear structure, perpendicular to the coast, reaching from coastal areas towards the Algerian coast. Similar to the measurements, a line with high reflectivity values (partly over the sea) can be found in the COSMO simulated reflectivity (Fig. 5.7, right). By the radar systems, this line was measured further north. A displacement error of approximately 100 km can be quantified. Aside from this aspect, a large agreement exists in the overall structure of both, measured and simulated, reflectivity fields. Regarding the mean reflectivity of the whole area, the COSMO simulation seems to have a positive bias in comparison to the field derived from the radar systems. This is confirmed for the studied time step by a positive mean error (eq. 3.12) of 9 dBZ.

As mentioned, radar reflectivity data were available in large parts over the Mediterranean Sea during HyMeX IOP8. Regarding the horizontal resolution of the observational dataset, it is $\Delta x \approx 1.4$ km and $\Delta y \approx 1.8$ km. These two facts make the reflectivity data suitable for a spatial intercomparison with the simulated reflectivity data. Therefore,
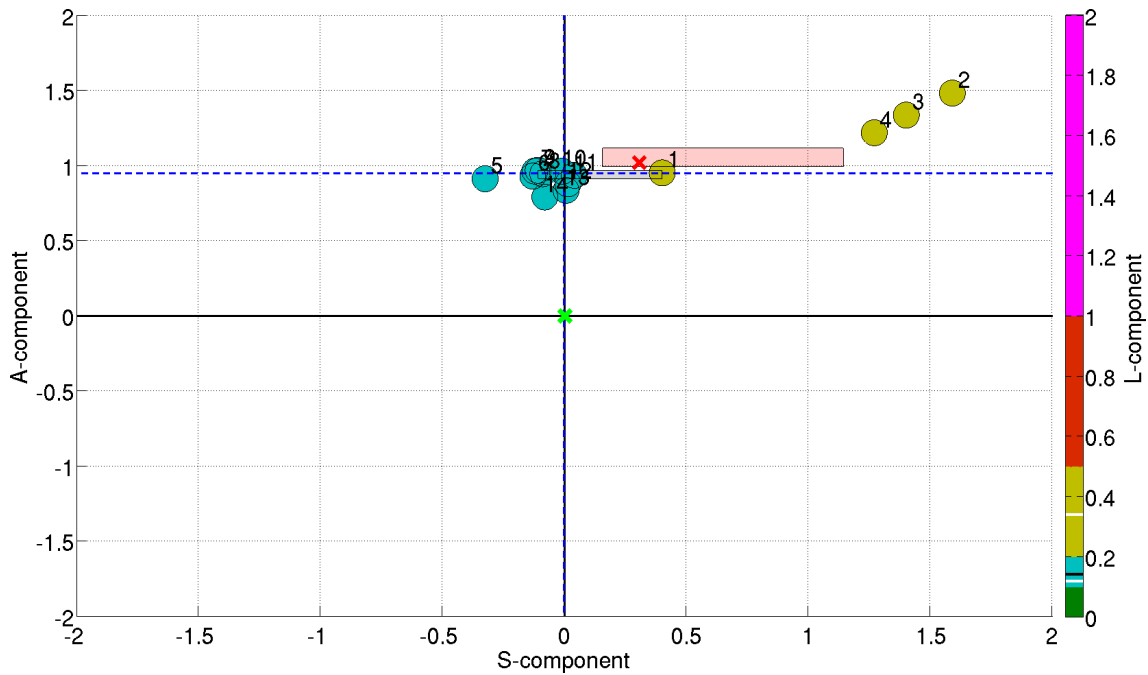
Figure 5.8: SAL plot for the intercomparison of the observed radar reflectivity with the simulated values from the COSMO run initialized on 28 September at 0600 UTC. The hourly timesteps of 28 September 2012 from 0700 UTC until 2000 UTC are shown.

the SAL method was deployed once more. The only difference compared to the spatial precipitation verification is the threshold value R, which was here calculated based on the 95th percentile of all grid point values greater than 5 dBZ. This was chosen as a barrier over which the radar reflectivity is large enough to be considered as evaluable.

To calculate the three components S, A and L, the measured reflectivity field was interpolated to the COSMO horizontal grid. As the COSMO data output is available every hour, the associated temporally nearest radar data were used. For the intercomparison of the observed radar reflectivity from 0700 UTC until 2000 UTC with the corresponding simulated values from the COSMO run, the median of the S-component resulted to almost zero (Fig. 5.8). Thus, the structure of the reflectivity patterns are almost equal in the observed and in the simulated fields. The median of the amplitude component is positive (0.95). That implicates higher reflectivity values in the COSMO simulation and is thus consistent with the calculated mean error. The median value for the L-component is 0.14 for this case. This value lies in the middle of the second (from five) quality step in the colorbar and implicates thus still a good skill. Regarding the single hourly intercomparison values, it turns out that from 0700 UTC until 1000 UTC, the agreement between both datasets is worst. Too large and too strong reflectivity fields were predicted for those time steps (Fig. 5.8, dots "1" to "4"). This is due to a lack of observational data for this time period. Unfortunately, not all radar systems in the western Mediterranean area were working for the whole period of interest. At least, the radar coverage was almost complete for the following hours. The best accordance exists between 1200 UTC and 2000 UTC. As these are the time steps where the measured reflectivity values were highest, this result is very satisfying.

To discuss the calculated SAL components in a wider context, they were calculated as well for the earlier initialized COSMO simulation. With the intersection point between the median of the S- and the A-component located in the upper right quadrant, the overall reflectivity values were calculated higher in this COSMO run than measured by the radar systems and the structure of the reflectivity patterns is larger in the output of the numerical simulation (Fig. 5.8, red cross). The broad interquartile range for the S-component is once again disturbed by the missing radar observations in the first hours and the involved outliers in the SAL-diagram (Fig. 5.8, light red rectangle).

With the investigations presented in this section, a further indication for the representativeness of the COSMO simulation, initialized on 28 September, 0600 UTC, is given for the overall situation of the heavy precipitation event HyMeX IOP8.

Summary

Several studies of precipitation and radar reflectivity fields during HyMeX IOP8 were conducted in this chapter. As the precipitation is the quantity which is directly responsible for socio-economic impacts like flooding events, a high-resolution COSMO simulation was investigated regarding its ability to reproduce the measured rainfall quantities. Over land, a satisfying agreement was found between raingauges and the output of the numerical simulation. Heaviest daily precipitation amounts occurred near Murcia and Valencia in both datasets. Concerning the precipitation over the Mediterranean Sea, satellite derived precipitation estimates were used as comparison dataset for the COSMO simulations. Focusing on the structure of a 3 hourly precipitation area, both datasets showed a good correlation within the spatial verification score SAL. A further comparison was performed with the AROME-WMED model. Compared with these data, in which several HyMeX measurements were assimilated, COSMO revealed very good scores, i.e. values near zero, for all component of SAL and satisfying ROC area values, overall larger than 0.7. Especially the heavy precipitation between 1200 UTC and 1800 UTC was reproduced very similar in both numerical models. With the measured radar reflectivity, a spatially highly resolved meteorological field, with data availability also over the Mediterranean Sea, the COSMO calculated radar reflectivity could be evaluated. A very high spatial agreement (median of S = 0) resulted between both datasets. Particularly the structure of the measured reflectivity was reflected almost perfectly by the COSMO model. Based on the findings of this and the previous chapter, the highly resolved COSMO simulation is used in the next chapter for an advanced investigation of the meteorological processes involved in the heavy precipitation event of HyMeX IOP8.

6 Numerical investigation of lifting mechanisms and moisture sources[*]

A spatially and temporarily higher resolved analysis of the physical processes which led to the heavy precipitation values of HyMeX IOP8 is performed here. First, the horizontal moist convergence line, detected in chapter 4, is studied regarding its temporal evolution and its effect on triggering deep moist convection in a potentially unstable atmosphere. Differences of the atmospheric stability are analyzed for several representative locations over land and over the Mediterranean Sea. Next, the role of orographic lifting for the initiation on deep convection is investigated. Therefore, a sensitivity study in which the topography of the western Mediterranean area was flattened is evaluated. Furthermore, dominant upslope winds are studied in detail. As an additional tool to visualize the atmospheric pathway of airparcels, Lagrangian moisture trajectories are used.

6.1 Moisture flux convergence

Based on surface station measurements and the COSMO simulations, a horizontal wind convergence line (Fig. 4.7) was supposed as one determinant triggering mechanism for the heavy precipitation measured during HyMeX IOP8. The convergence line established in the morning of 28 September 2012 and reached from Malaga to the African coast. In the course of the following hours, the convergence line moved northeastwards, always reaching from the Spanish Mediterranean coast towards the Mediterranean Sea and vanished on 30 September 2012. Figure 6.1 illustrates the movement of the COSMO simulated convergence line between 0800 UTC and 2000 UTC on 28 September 2012. Westerly winds from the Strait of Gibraltar and easterly winds from the Mediterranean Sea are converging especially over the sea surface. But also over the Spanish Mediterranean coast, the effect of the convergence line is visible. Driven by the cut-off low in upper levels (Fig. 2.2), the convergence line is moving northeastwards. This occurs almost continuously with a displacement velocity of about $60\,\mathrm{km}\,\mathrm{h}^{-1}$. Regarding the absolute values, the convergence was most pronounced at 1500 UTC while passing over Murcia.

Near ground wind velocities at $10\,\mathrm{m}$ height and surface specific humidity at $2\,\mathrm{m}$ height were used to calculate the moisture flux convergence (eq. 2.11). On 28 September 2012, 1500 UTC, positive moisture flux convergence values exceed $6 \cdot 10^{-4}\,\mathrm{kg}\,\mathrm{kg}^{-1}\,\mathrm{s}^{-1}$ (Figure

---

[*]Results of this chapter are partly included in Röhner et al. (2016).
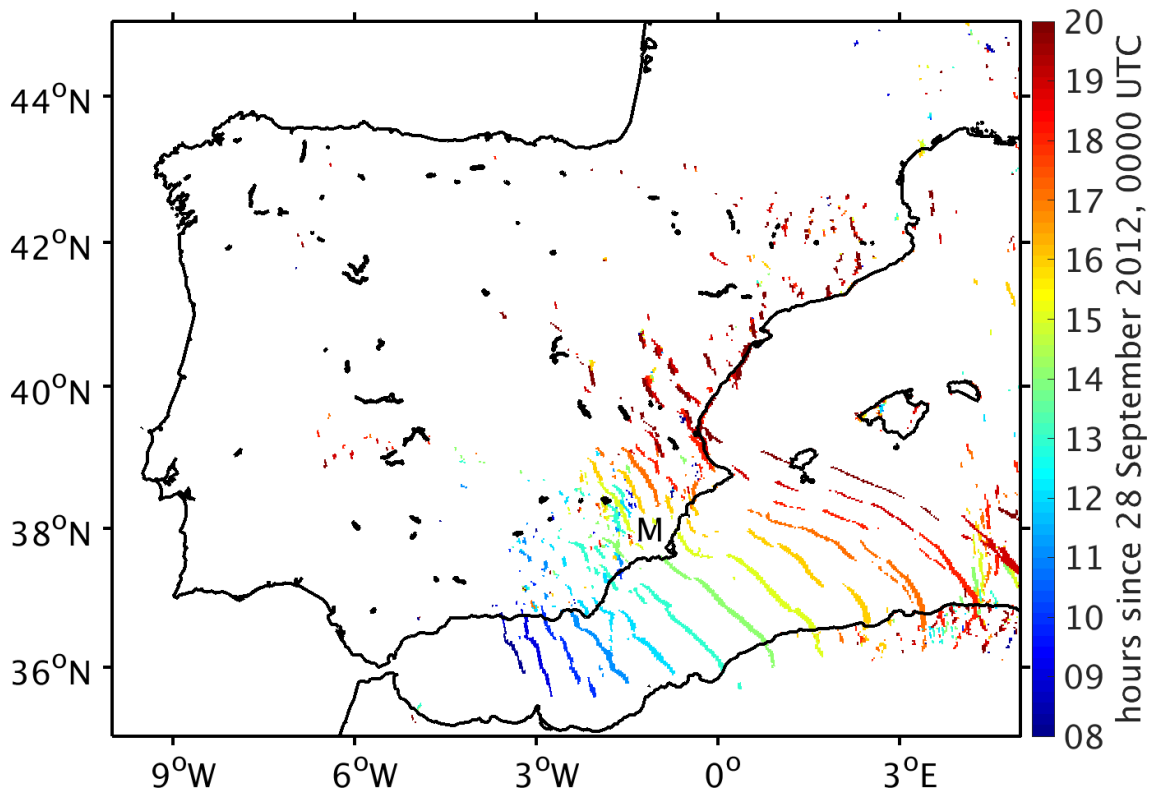
Figure 6.1: Temporal evolution of the COSMO simulated horizontal convergence line between 0800 UTC and 2000 UTC on 28 September 2012. Horizontal wind convergence values of more than $0.008\,\mathrm{s}^{-1}$ are shown for each time step.

6.2). Clearly visible at this time step is the convergence area reaching from Murcia over the Mediterranean Sea towards Algiers. Whether the moist convergence line served as trigger mechanism for deep moist convection and thus for heavy precipitation is investigated in the next section.

6.2 Stability of the atmosphere

To investigate whether the horizontal moist convergence line was responsible for the release of potential instability and so for the triggering of heavy rain, the atmospheric stability has to be studied in detail. For this reason, several temporarily subsequent vertical profiles of the equivalent potential temperature Θ_e (eq. 2.8) were calculated at several selected grid points of the model area over land and over the Mediterranean Sea (Fig. 6.2, green and magenta crosses). While the convergence line is passing at about 1500 UTC over all selected points over land and over the Mediterranean Sea, the time steps before (1200 UTC) and after (1800 UTC) show the atmospheric stability in a calmer situation. The mean vertical Θ_e profile over land (resulting from the single profiles denoted by the the green crosses in Fig. 6.2) has a surface value of around $62\,^{\circ}\mathrm{C}$ at 1200 UTC (Fig. 6.3, top left). In lower levels, the profile shows a slightly unstable atmosphere: Θ_e is decreasing to around $57\,^{\circ}\mathrm{C}$ at $600\,\mathrm{m}$ height. This slight instability goes along with weak

66
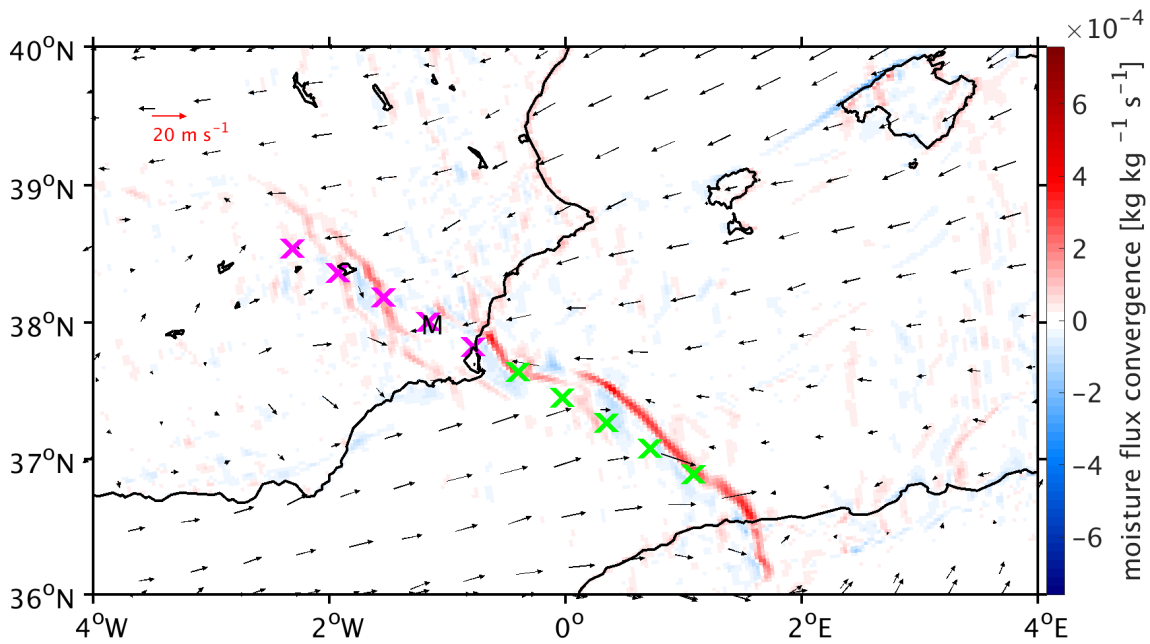
Figure 6.2: Near ground moisture flux convergence (colored) and horizontal wind field at 10 m height on 28 September 2012, 1500 UTC. At the locations of the green (magenta) crosses, vertical Θ_e profiles were calculated over the Mediterranean Sea (over land).

CAPE values, ranging below $200 \, \mathrm{J \, kg^{-1}}$ (Fig. 6.3, bottom left). During the passing of the convergence line at around 1500 UTC, the mean profile shows a neutral atmospheric environment. The standard deviation at this time step is quite large. This can be linked on the one hand to the heterogeneous terrain over land and the involved different thermodynamical conditions. On the other hand, the convergence line passed isochronically over all chosen locations. Thus, not all points are located on the same side of the convergence line at 1500 UTC. Though, the mean surface Θ_e value decreases to around $55\,^{\circ}\mathrm{C}$. This leads to the assumption that potential instability was released and convection occurred. The release of energy can be seen in the time series of CAPE: almost no CAPE remains after 1500 UTC. The simulated precipitation at 1500 UTC shows an hourly accumulated sum up to almost $25 \, \mathrm{mm \, h^{-1}}$ (Fig. 6.3, bottom left). At 1800 UTC, the mean profile indicates a stable lower atmosphere.

Over the Mediterranean Sea, the situation is different. With CAPE values exceeding $1000 \, \mathrm{J \, kg^{-1}}$, only a small maximum mean precipitation amount of about $12.5 \, \mathrm{mm \, h^{-1}}$ was simulated (Fig. 6.3, bottom right). The triggering of the convection for the associated grid points (denoted by the magenta crosses in Fig. 6.2) is temporally linked to the passing of the horizontal moisture flux convergence line. Investigating the connected Θ_e profiles (Fig. 6.3, top right), a large potential instability was present at 1200 UTC in heights until approximately 1100 m. At the passing of the convergence line at around 1500 UTC, mean surface Θ_e values are decreasing abruptly from around $72\,^{\circ}\mathrm{C}$ to approximately $60\,^{\circ}\mathrm{C}$. Through triggered convection, the instability as well as the upper inversion layer are dissolved and a mean stable atmosphere results. This can also be seen by the mean CAPE values which also decrease very fast to almost $0 \, \mathrm{J \, kg^{-1}}$. During the following hours until 1800 UTC, a new destabilization is created at low levels. Also CAPE
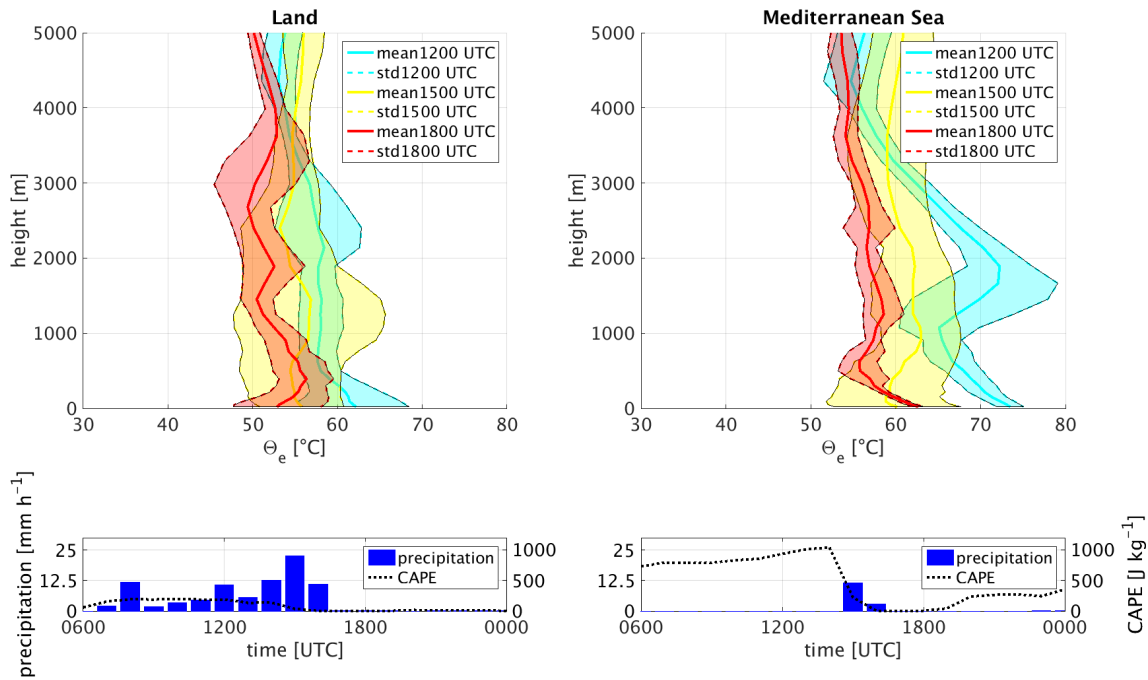
Figure 6.3: Top: Mean vertical Θ_e profiles and their standard deviations from surface until 5 km height for 28 September at 1200 UTC, 1500 UTC and 1800 UTC. Left, the profiles over land (magenta crosses in Fig. 6.2) and right, the profiles over the Mediterranean Sea (green crosses in Fig. 6.2) are shown. Bottom: Mean precipitation and mean CAPE over time.

values recuperate slightly. As no further triggering mechanism appeared after the convergence line, this potential instability is not released anymore and no further precipitation occurred.

As the simulated precipitation over the Mediterranean Sea is temporarily perfectly correlated with the passing of the horizontal moist convergence line (Fig. 6.2), it is assumed that also a high causality exits between both mechanisms. This leads to the hypothesis that the strength of the convergence line can be expressed by its ability to provide enough moisture for approximately $10 \, \mathrm{mm \, h^{-1}}$ of precipitation. Regarding the significantly higher simulated and measured precipitation values over land, it is supposed that the convergence line could not be responsible alone for the necessary moisture inflow. Thus, the hypothesis is stated that a further trigger mechanism was present.

6.3 Orographic effects

As found in the section before, only slight potential instability and low CAPE values were analyzed for selected grid points over the Spanish mainland. According to high simulated precipitation rates in these regions, it is supposed that the horizontal moisture flux convergence may not have been the only mechanism for the transport of moist airmasses in upper levels. The hypothesis for the existence of a second lifting mechanism is stated. Another hint for this hypothesis are precipitation areas which cannot be linked
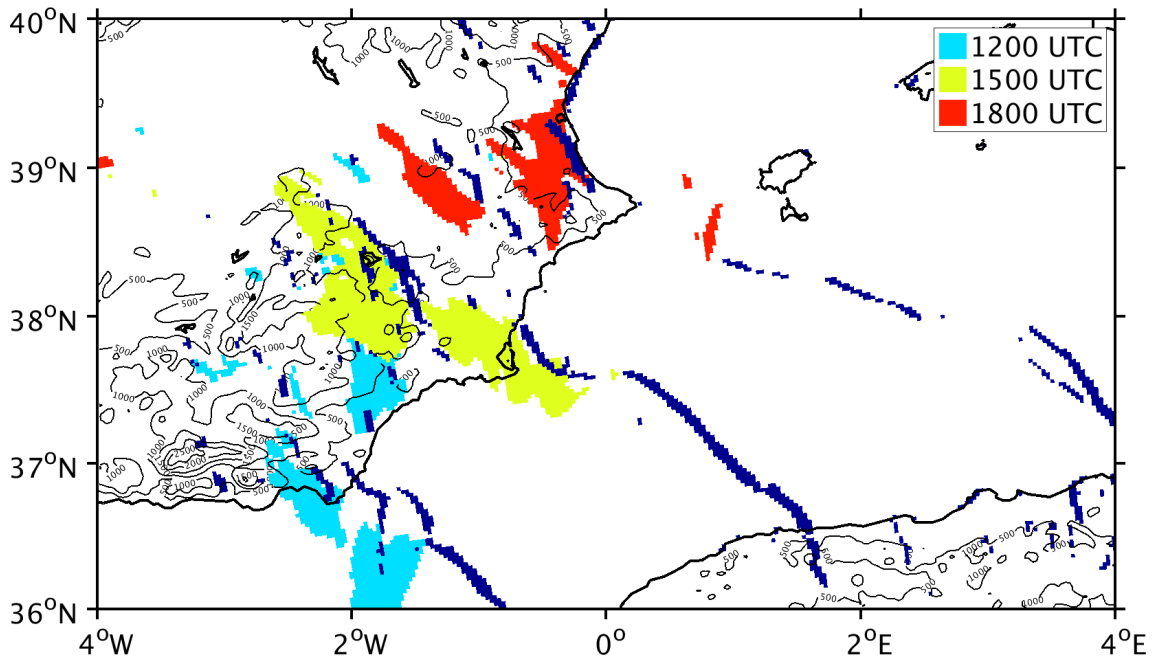
Figure 6.4: COSMO simulated horizontal wind convergence (threshold value as given in Fig. 6.1) at 1200 UTC, 1500 UTC and 1800 UTC on 28 September 2012 (dark blue lines) together with the associated hourly precipitation fields with more than $15\,\mathrm{mm\,h^{-1}}$ (light blue, yellow and red areas).

chronologically to the passing of the convergence line. Most precipitation areas formed southwesterly of - so temporally behind - the convergence line (Fig. 6.4). For these cases, it is concluded that the simulated precipitation could have been directly triggered by the horizontal moist convergence. But in contrary there also exist areas where precipitation was simulated independently of the convergence line. Especially at 1200 UTC, heavy precipitation was simulated southwest from Murcia, where the convergence line passed at around 1300 UTC. This leads to the hypothesis that a further trigger mechanism was responsible for the hourly accumulated precipitation before 1200 UTC near Murcia. Regarding the topography in this region (Fig. 2.1), orographic lifting effects are supposed as likely.

To test this hypothesis, a sensitivity study was performed with COSMO. The control simulation is the one used before. As a sensitivity experiment, a simulation with a flat orography was calculated. All elevations higher than $10\,\mathrm{m}$ were capped to this height. This procedure is based on the factor separation technique, presented in Stein and Alpert (1993) and is used also in other studies investigating orographic effects in the western Mediterranean area (e.g. Barthlott and Kirshbaum, 2013). Within the non-orography experiment, the flat orography leads to perturbed wind fields and thus to a different precipitation pattern. As the mesoscale flow is disturbed increasingly with growing forecast time, the orographic effect seem to be representative in the first few hours only. In this interval, the atmospheric conditions are still forced by the unperturbed initial and boundary conditions. With a relatively short lead time of approximately $6\,\mathrm{h}$ between simulation initialization and occurring of the heavy rainfall event, it is supposed that the perturbed
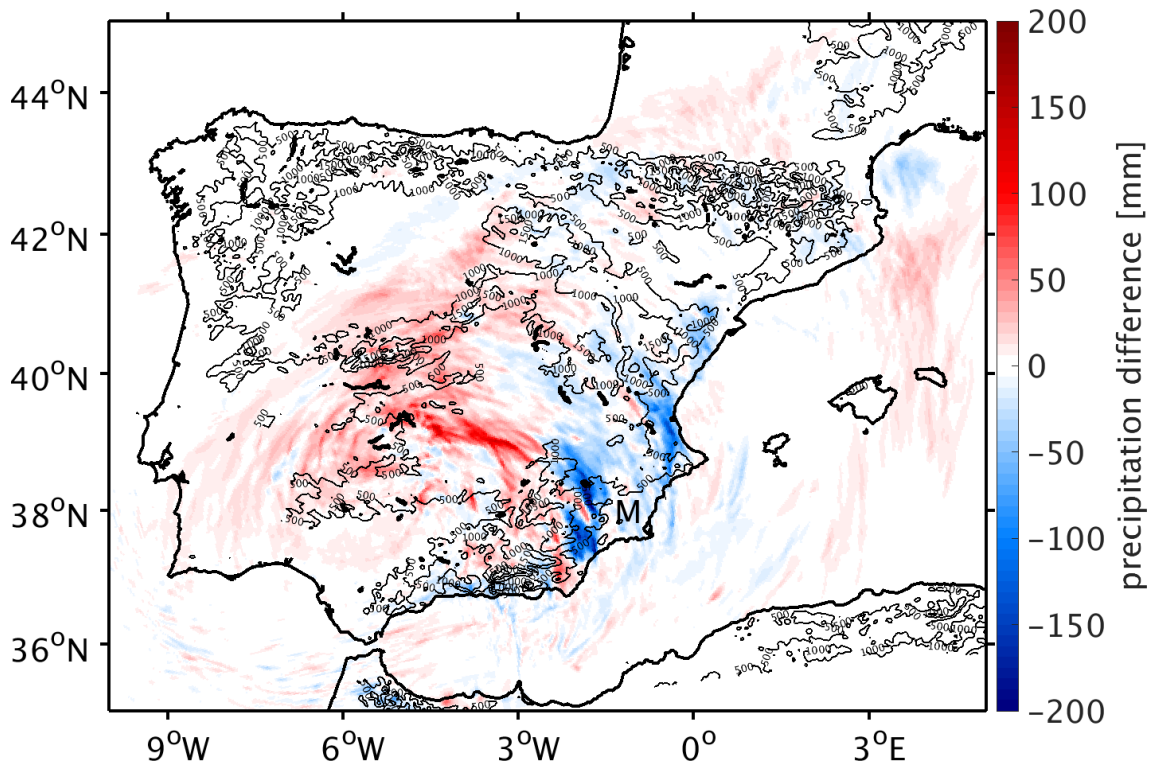
Figure 6.5: Difference of the 24 h accumulated COSMO simulated precipitation amount without orography minus the 24 h accumulated precipitation amount with orography (28 September 0600 UTC to 29 September 2012, 0600 UTC).

precipitation can be still linked to the different orographic conditions.

As expected, different precipitation structures were obtained by calculating the 24 h accumulated precipitation amounts of both simulations from 28 September 0600 UTC until 29 September 0600 UTC. The effect of the orography is presented by means of the differential field of the precipitation sum without orography minus the precipitation sum with orography (Fig. 6.5). The first important point is the large change of the precipitation amount over land. Over the Mediterranean Sea almost no differences were obtained for this accumulation period. This is an indicator that the mesoscale flow did not change significantly and that other trigger mechanisms for deep convection were existent over the sea surface. The second point concerns the above mentioned region southwest of Murcia, which was affected by heavy precipitation at around 1500 UTC (Fig. 6.4). Here, much less precipitation occurred in the non-orographic experiment with flat orography. So, it is concluded that the prominent difference of around $200 \, \text{mm} \, 24 \text{h}^{-1}$ can be related to the orographic role of the mountainous "Sistema Penibetico" with heights over 3000 m in this area. The increase of rain in central Spain in the simulation without orography can presumably be traced back to a deformed mesoscale flow pattern. The winds coming from the east to the Spanish Mediterranean coast are no longer blocked by the mountainous area and converge with the western air masses over the Spanish landmass.
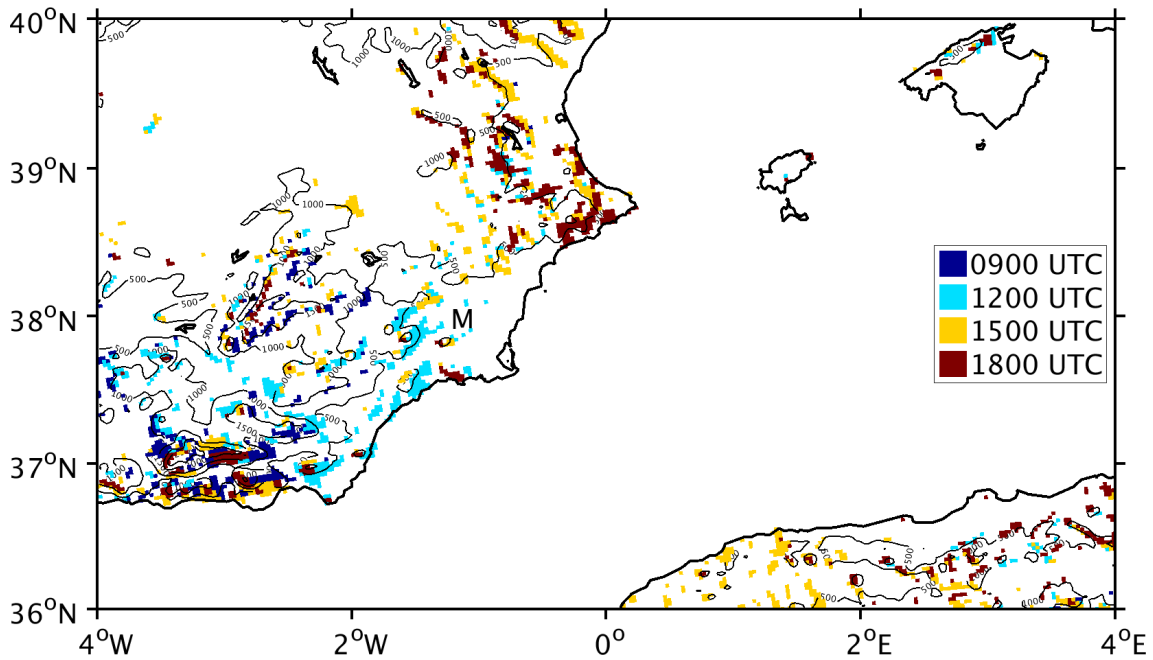
Figure 6.6: COSMO simulated upslope wind larger than $0.2\,\mathrm{m\,s^{-1}}$ at 0900 UTC, 1200 UTC, 1500 UTC and 1800 UTC on 28 September 2012.

To underline the hypothesis that the orography was the main reason for the triggering of deep convection over land, a further study was performed. Therefore, the upslope wind w_{oro} (e.g. Houze, 1993, Lin et al., 2001 or Neiman et al., 2002) was used. It is given by

$$w_{oro} = \vec{v}_h \cdot \nabla z \qquad (6.1)$$

with the horizontal wind velocity v_h and the orographic height z. During HyMeX IOP8, significant upslope wind was present in various regions at different locations (Fig. 6.6). Generally, a northeastwards displacement of upslope wind areas can be remarked between 0900 UTC and 1800 UTC. In the region southwest from Murcia, easterly winds coming from the Mediterranean Sea rise up at 1200 UTC. As the air is saturated with a high amount of moisture, deep moist convection with resulting heavy rainfall can be triggered here. This is consistent with the findings of the studies before and thus emphasizes the importance of orographically induced deep convection in this area.

In summary, it can be stated that besides the convergence line, orographic effects were important for the occurrence of heavy precipitation during HyMeX IOP8. Two examinations pointed to relevant orographic effects. On the one hand, a sensitivity study with removed orography showed significant precipitation differences to the control simulation. On the other hand, significant upslope winds at the Spanish Mediterranean coast underlined the strong orographic component for triggering precipitation in the area of interest.

6.4 Lagrangian trajectories

Now, the moisture advection for the heavy precipitation event of HyMeX IOP8 is discussed. Therefore Lagrangian trajectories (sec. 3.2.2) are investigated. In contrary to the previous sections, COSMO was used here with a spatial horizontal resolution of $\Delta x \approx 7\,\text{km}$. This resolution is sufficient to identify the structures of interest, i.e. mesoscale convective structures and embedded convection. Trajectories based on a higher resolved COSMO simulation ($\Delta x \approx 2.8\,\text{km}$) are superimposed by "noise" due to variability in trajectory pathways, which makes it very difficult to identify the larger governing structures.

On the one hand, specific humidity values along the trajectories are analyzed. With this study, various moisture uptake regions can be linked to precipitation areas. On the other hand, the vertical velocity values are discussed. Here, the processes of deep convection taking place during HyMeX IOP8 are highlighted.

Trajectories were initialized every 6 min at each model grid point at 980 hPa in an area reaching from 20°W to 15°E and from 30°N to 45°N. The horizontally moving air parcels, loaded with humidity, demonstrate the importance of the sea surface as moisture source.

For trajectories started on 27 September 2012 at 1200 UTC, bundles of moist trajectories from the East Atlantic and bundles of moist trajectories from the region between the Balearic Islands and Sardinia can be singled out (Fig. 6.7, top). They converge and thus build up the wind and moisture convergence near the ground. Regarding the specific humidity, values near to $0\,\text{g}\,\text{kg}^{-1}$ occur at the end of the ascent, just below the tropopause. This represents a large difference compared to values of $13\,\text{g}\,\text{kg}^{-1}$ to $14\,\text{g}\,\text{kg}^{-1}$ near the ground. Some of the trajectories originating in the Gulf of Cadiz and the Gulf of Lion, first collect moisture on their way. At the beginning of their track, the specific humidity is about $8\,\text{g}\,\text{kg}^{-1}$ and reaches values of $15\,\text{g}\,\text{kg}^{-1}$ at southern Spain before starting the ascent. Air masses from the Mediterranean are leading to the convective precipitation in coastal areas and over the Mediterranean Sea. This is clearly indicated by the rapid ascent of the trajectories over south-eastern Spain with mean vertical model velocities around $1\,\text{m}\,\text{s}^{-1}$ on grid scale (Fig. 6.8, top). Some of the trajectories already ascended significantly within the first 6 hours (Fig. 6.9, top, region A). Local strong uplift at the coastal orography triggered deep convection. Trajectories with a pathway leading from the south to the north of Spain are supposed to be at least partly responsible for the precipitation from stratiform clouds inland of Spain. The associated ascent to heights over more than 7000 m occurred within 6 to 12 hours. The trajectories from the Mediterranean arrived after approximately 18 hours in the same uplift area (Fig. 6.9, top, region B). East of Murcia, they propagated vertically and favored a triggering of new convection cells (Fig. 6.9, top, green arrow). The ascent took place within less than 6 hours and is a bit faster, but temporarily later, than the ascent of the trajectories started in the region near Gibraltar. The trajectories now ascended up to 10000 m which is a clear indicator of deep convection. The vertical velocity of approximately $1\,\text{m}\,\text{s}^{-1}$ along the trajectories (Fig. 6.8, top) is a further hint for deep convection. Some of the discussed trajectories pursue an anticyclonic track towards the end of their ascent (Fig. 6.7, top, red arrow). There, they enter

an area under an upper-level weak ridge (Fig. 2.2, top).

One day later, the number of trajectories coming from the Atlantic Ocean decreased significantly. Thus, less moisture from the Atlantic Ocean was now involved in the associated precipitation systems. The origins of most trajectories started on 28 September 2012 at 1200 UTC are located within a 100 km radius around their ascent region (Fig. 6.7, bottom). The day before, the catchment area was much larger (Fig. 6.7, top). Now, a convergence line is located approximately from Valencia to Palma. Linked to the convergence line is a strong uplift area, obvious by the vertical velocity values of $1\,\mathrm{m\,s^{-1}}$ in several trajectory bundles (Fig. 6.8, bottom). Trajectories reached significant heights in less than 6 h (Fig. 6.9, bottom). The corresponding air parcels were thus responsible for the heavy precipitation around Murcia (e.g. Fig. 4.6, blue bars). The trajectories initialized on 28 September 2012 at 1200 UTC rose up to around 8000 m and turned then in a cyclonic path below the tropopause. This is a result of the change of the flow in this height due to the approaching cut-off low (Fig. 2.2, top).

Starting the trajectories at 900 hPa (Fig. 6.10, top) or 850 hPa (Fig. 6.10, bottom), the specific humidity of the air parcels have ground-level values of only $8\,\mathrm{g\,kg^{-1}}$ to $11\,\mathrm{g\,kg^{-1}}$. A comparison between the three starting levels 980 hPa, 900 hPa and 850 hPa shows that the catchment area around the region of ascent is getting smaller with increasing starting height of the trajectories. Both points indicate that the main moisture uptake for HyMeX IOP8 took place in lower levels very near to the sea surface. The moisture is concentrated in rather narrow uplift channels.

In summary it can be concluded that the heavy precipitation event HyMeX IOP8 is well captured by the trajectories initialized between 27 September 2012 at 1200 UTC and 28 September 2012 at 1200 UTC. Highest vertical velocity values occurred in the area just over the regions where highest precipitation values were measured.
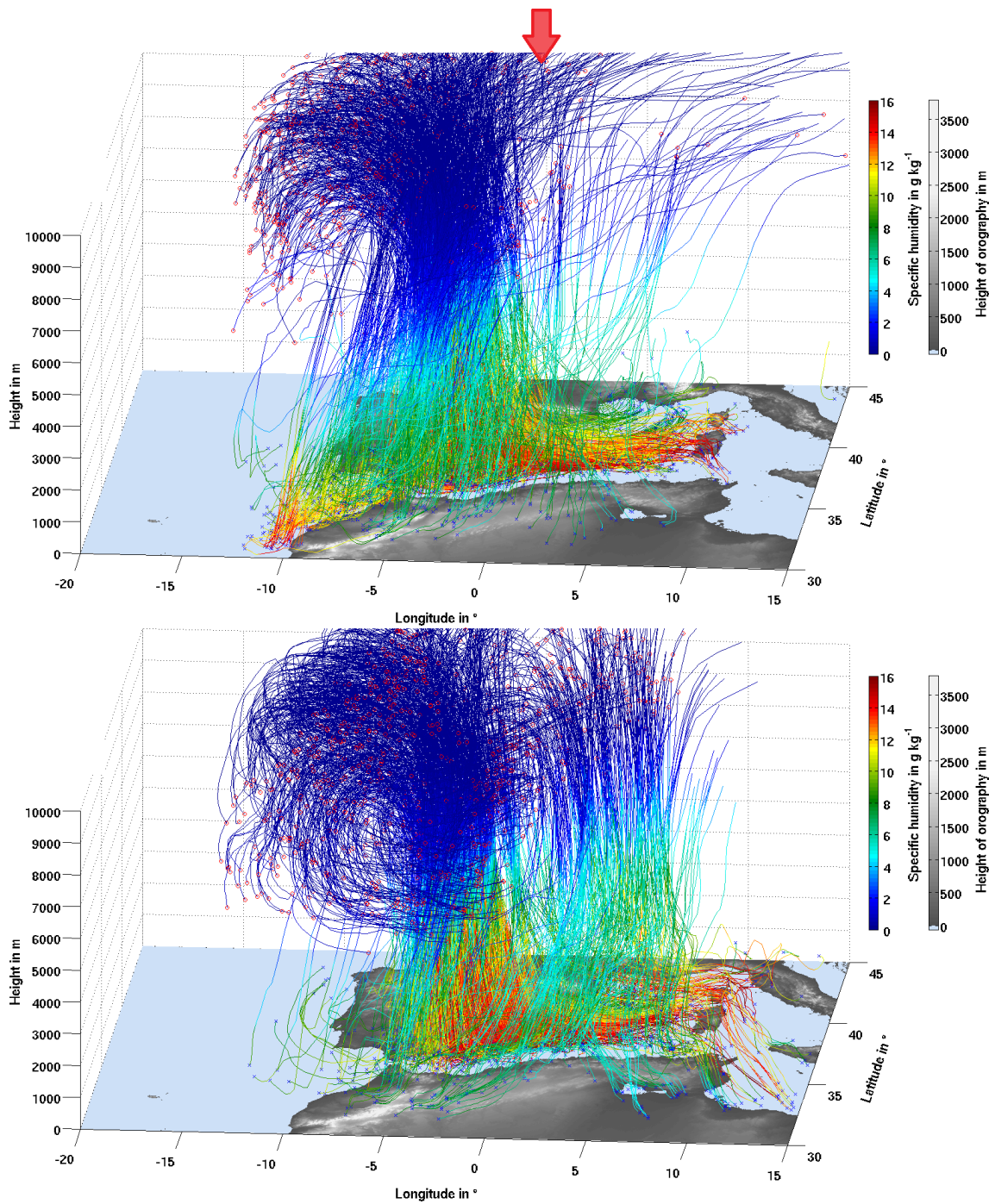
Figure 6.7: Forward trajectories calculated for the following 36 hours with specific humidity in g kg^{-1} (colored) and orography in m (gray shaded) for the starting times: 27 September 2012, 1200 UTC (top) and 28 September 2012, 1200 UTC (bottom). Trajectories that rise more than 600 hPa within a 36 hours forward calculation are shown. For a better visibility of the main trajectory bundles, only each twentieth calculated trajectory is shown.
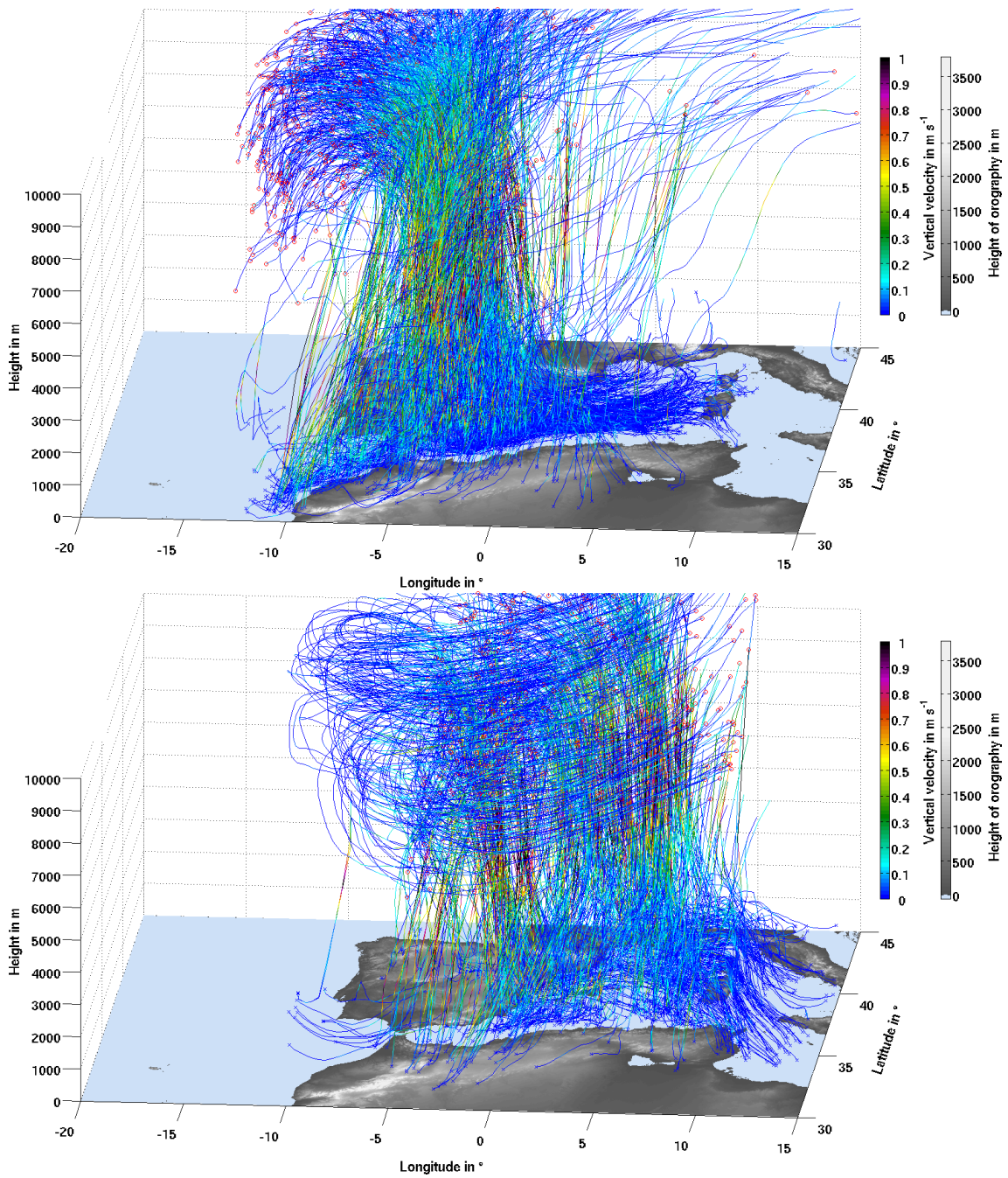
Figure 6.8: Forward trajectories for vertical velocity in m s^{-1} started on 27 September 2012 at 1200 UTC (top) and on 28 September 2012 at 1200 UTC (bottom).
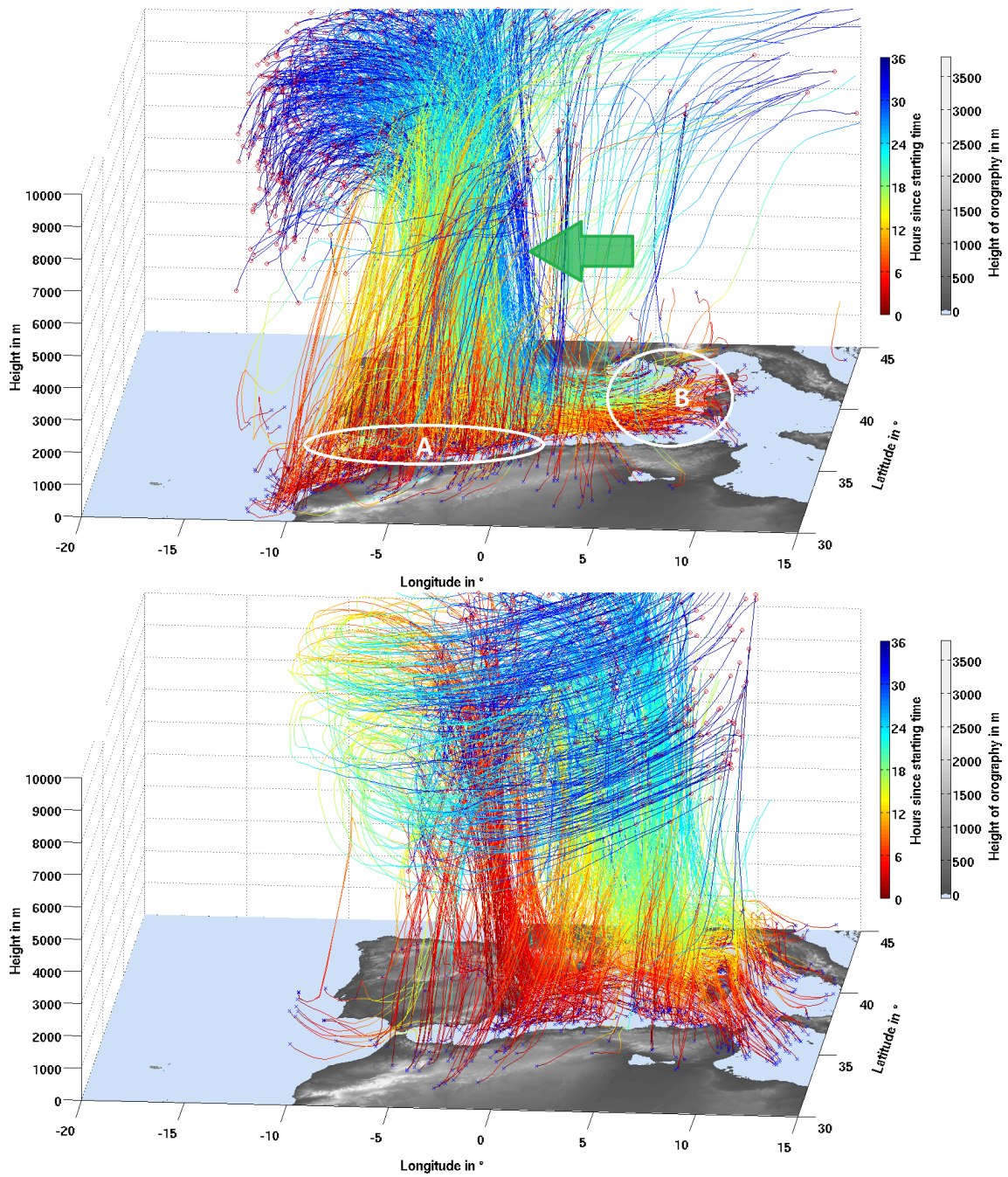
Figure 6.9: Forward trajectories for hours since trajectory start started on 27 September 2012 at 1200 UTC (top) and on 28 September 2012 at 1200 UTC (bottom).
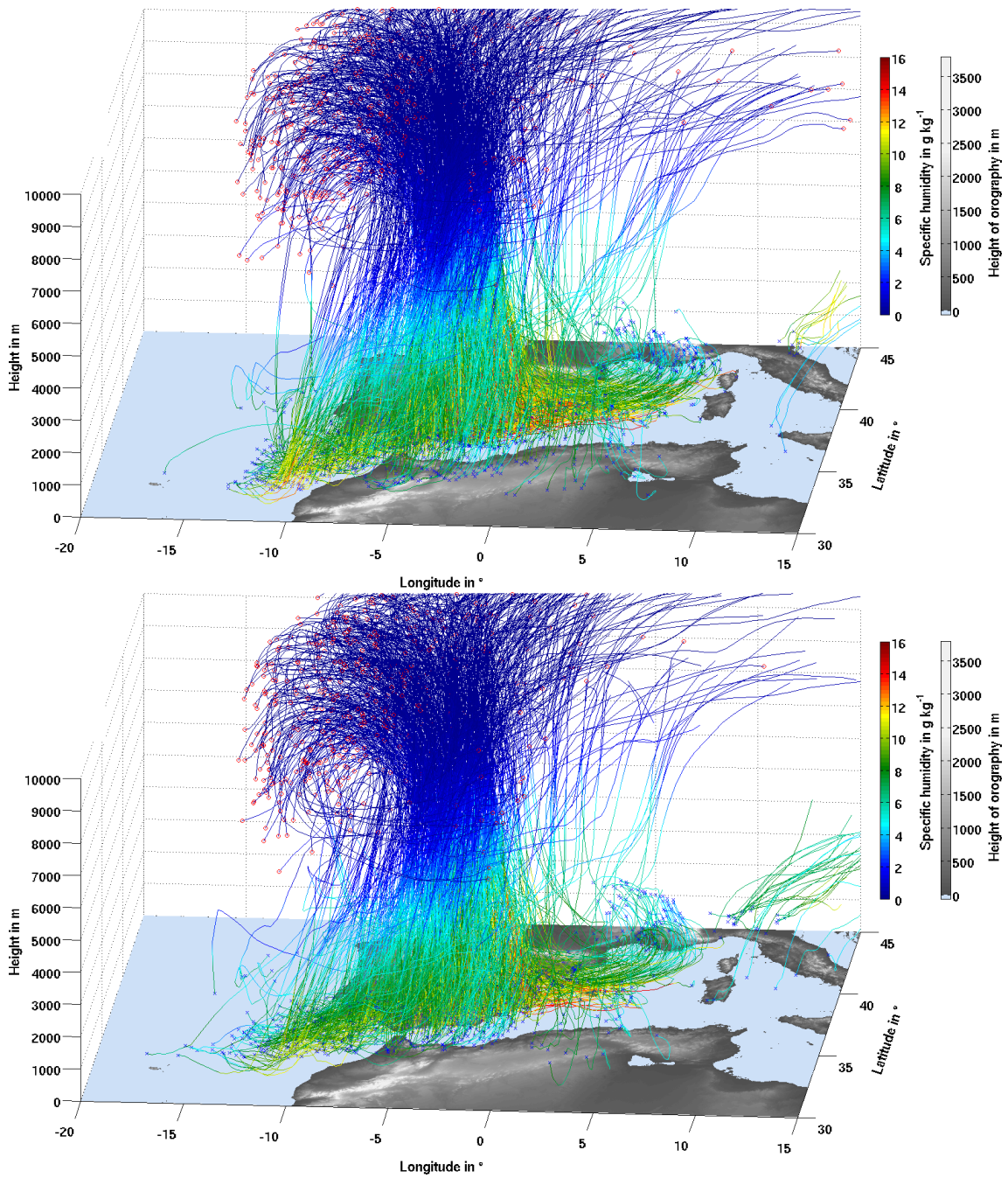
Figure 6.10: Trajectories for specific humidity started at 1200 UTC on 27 September 2012 at 900 hPa (top) and 850 hPa (bottom).

Summary

After the study of observation-based meteorological fields in chapters 4 and 5, numerical simulations were investigated in this chapter. With high spatial and temporal resolutions of the model output, the development of physical processes could be evaluated in a three-dimensional box over the area of interest. The first parts of this chapter focused on the initiation and the development of deep moist convection during HyMeX IOP8. Vertical profiles of the equivalent potential temperature Θ_e revealed different conditions regarding the atmospheric stability over land and over the Mediterranean Sea. Whereas strong potential instability was present over the warm and moist sea surface, a significantly weaker unstable atmosphere dominated the situation over land. Between 0800 UTC and 2000 UTC on 28 September 2012, a strong horizontal moist convergence line was detected over the Mediterranean Sea. With an orientation almost perpendicular to the coast, it moved northeastwards during the day. Regarding the simulated precipitation amount over the sea, a high correlation with the passage of the convergence line was found. Over land, orographic effects resulted as additional trigger mechanisms for deep moist convection. Especially the region southwest of Murcia was affected strongly by orographically induced heavy precipitation. Prominent upslope winds were present around 1200 UTC, when strongest rainfall occurred. Concerning the daily precipitation amount, a sensitivity experiment with flattened topography resulted in a significant decrease of precipitation for this case in the area near Murcia. The last part of this chapter addressed the moisture sources for the heavy precipitation during HyMeX IOP8. By the analysis of Lagrangian forward trajectories, pathways of airparcels were followed from their origin until their leaving of the box of investigation. Two main moisture origins were found for the investigated case study. Whereas moisture from the Atlantic Ocean led to precipitation in southern Spain, the heavy rainfall events between Murcia and Valencia were fed by low-level moisture from the Mediterranean itself.

7 Predictability studies for heavy precipitation events

As a heavy precipitation event like HyMeX IOP8 can lead to massive socio-economic problems, it is desirable to forecast such an event with sufficient lead time for warnings and safety precautions. A single deterministic forecast as investigated in chapters 4, 5 and 6 does not carry information about the quality of the forecast with respect to the uncertainty of the occurrence of such an event. Ensemble prediction systems are currently used to sample the distribution of plausible atmospheric states, compatible with all sources of available information, and thus account for the uncertainties and allow to produce probability estimates of the quality of the forecast. By means of ensemble forecasts, the predictability of two heavy precipitation events is studied. One event (HyMeX IOP8) is a synoptically strongly forced case, whereas the second case (HyMeX IOP12b (sec. 2.2.3)) is driven by a weakly forced synoptic situation. Five different ensemble systems were set up for both events (sec. 3.1.3). Each ensemble consists of a different percentage of large-scale and small-scale variability. Large-scale uncertainty is gained by using various initial condition derived from ECMWF-EPS. Small-scale variability results from the stochastic cumulus parameterization scheme Plant-Craig (sec. 3.1.4). Dependent on the strength of the large-scale forcing it is desired to provide a guideline which combination of synoptic- and convective-scale uncertainty is favorable for a suitable ensemble prediction of the expected heavy precipitation.

A similar ensemble approach to study different sources of uncertainty for differently forced heavy precipitation events was applied by Groenemeijer and Craig (2012) and Kober et al. (2015). In these studies, a 10×10 member ensemble was created due to 10 initial conditions from ECMWF-EPS and each time 10 realizations with the Plant-Craig scheme. Groenemeijer and Craig (2012) found that the stochastic parameterization scheme is an important source for precipitation variability in cases of weak large-scale flow but with high convective activity. In Kober et al. (2015), the same 100-member ensemble was compared to a 10-member ensemble, designed with the deterministic Tiedtke scheme (sec. 3.1.4). It was found that the large ensemble based on the stochastic parameterization was superior in a weakly forced heavy precipitation event. Also a separation of both scales of uncertainty was studied. On the one hand, a 10×1 member ensemble with only large-scale uncertainty was selected. On the other hand, a 1×10 member ensemble with only stochastic variability was evaluated. For two cases with different strengths of synoptic forcing, more spread was generated each time by the ensemble created via various initial and boundary conditions. Nevertheless, the contribution from the stochastic sub-ensemble to the overall variability was found to be more important in the weaker forced event.

Compared to the presented two studies, the ensemble setting of this thesis allows to go one step further. A novel approach to further investigate mixed-scale perturbations, is introduced. For two well analyzed and well understood HyMeX IOPs with significant rainfall amounts, the five applied ensembles are investigated regarding their ability to encompass the natural variability of convective precipitation and regarding their ability to discriminate between extreme events and non-events. For the strongly forced case, it is supposed that most of the small-scale phenomena depend on the large-scale forcing and so synoptic-scale uncertainties produce large variations in the forecast. In order to get a reliable representation of the possible forecasts compatible with the known information of initial and boundary conditions and physical parameterizations, the large-scale must then necessarily be taken into account. As the large-scale driving forces are very influential on the impacts of the event, it is thus hypothesized that the ensembles with more large-scale variability will lead to a better ensemble prediction (sec. 3.3.5) for HyMeX IOP8. For the weaker forced heavy precipitation event it is assumed that the final impact, which is estimated here by the precipitation and radar reflectivity fields, is not substantially dependent on the large-scale situations. To not produce an overconfident forecast by sampling large-scale uncertainty, computational resources may be spend at sampling the small-scale uncertainty and thus hopefully get a better representation of the distribution of possible forecasts.

After an overview of the experimental design of the ensembles, rank histograms and ROC curves are used as probabilistic verification scores to investigate and to interpret the performance and quality of each of the five ensembles for both heavy precipitation events. Internal ensemble spread and its accordance with the variability of meteorological observations is studied for both heavy precipitation events.

7.1 Setup of the ensemble study

To study the predictability of both HyMeX heavy precipitation events, different ensemble forecasts were performed. As a comparison of ensembles with different sizes would favor the ensemble with more members (e.g. Callado et al., 2013), one common characteristic of the here applied ensembles is the same number of members in each ensemble. Further equally chosen settings are the horizontal resolution, the forecast duration and the domain (Fig. 3.4) of the ensemble simulations. Each ensemble consists of 16 members and was computed on a grid with a spatial horizontal resolution of $0.0625° \approx 7\,\mathrm{km}$. The ensemble simulations for HyMeX IOP8 were started on 27 September 2012 at 0000 UTC. The initialization time for HyMeX IOP12b was on 11 October 2012, 0000 UTC. All numerical simulations ran for 48 hours. The maximum precipitation occurred after approximately 36 h in both cases.

For each case study, five different ensembles were calculated. Perturbations were made on the one hand by different initial conditions and on the other hand by the parameterization of deep moist convection in the numerical weather prediction system COSMO.

The first ensemble, called "*Ensemble 16 × 1*", is characterized mainly by synoptic-scale perturbations in the initial conditions. To gain the most distant synoptic conditions for

the use as initial conditions, a clustering of the 51 members of the ECMWF-EPS (e.g. Leutbecher and Palmer, 2008) was made (sec. 3.1.3). With the choice of 16 clusters, one representative member resulted for each cluster and so 16 different initial conditions could be used to drive the mesoscale COSMO ensemble. The Plant-Craig scheme (sec. 3.1.4) was used to parameterize the deep moist convection in the COSMO model.

"*Ensemble 1 × 16*" is constructed via only small-scale perturbations. As initial condition, the control forecast of the ECMWF-EPS is used for every single member of this ensemble. It is hypothesized that the control run is representative for all members of ECMWF-EPS. To obtain 16 different small-scale situations, the stochastic cumulus convection scheme Plant-Craig is deployed again.

To sample both large- and small-scale uncertainties, a design of intermediate combinations of *Ensemble 16 × 1* and *Ensemble 1 × 16* was established. For further ensembles with 16 members, clusterings of the ECMWF-EPS with 8, 4 and 2 resulting representative members were made. Where the 8 (or 4 or 2) most distant synoptic situations were computed, 2 (or 4 or 8) realizations with the stochastic Plant-Craig scheme led to the sampling of small-scale uncertainty. The intermediate ensembles are called "*Ensemble 8 × 2*", "*Ensemble 4 × 4*" and "*Ensemble 2 × 8*" in the following.

Table 7.1 highlights the selected members of ECMWF-EPS for all five ensembles for Hy-MeX IOP8 and HyMeX IOP12b. A graphical visualization of the ensemble setup is given in Table 3.1.

Table 7.1: Representative members of the ECMWF-EPS (derived by a clustering method, described in sec. 3.1.3), which were used as initial and boundary conditions for the five ensembles to investigate HyMeX IOP8 and IOP12b. The first number of the ensemble name (e.g. "8 × 2") indicates the number of initial condition perturbations, the second number represents the realizations with the Plant-Craig scheme.

	IOP8					IOP12b				
	16×1	8×2	4×4	2×8	1×16	16×1	8×2	4×4	2×8	1×16
cf					🟨					🟨
1										
2										
3										
4						🟥		🟩		
5	🟥	🟦				🟥		🟩		
6	🟥									
7						🟥	🟦			
8						🟥				
9	🟥					🟥				
10										
11							🟦			
12										
13						🟥				
14										
15										
16										
17							🟦			

Figure 7.1: Areas for the evaluation of the ensembles. The whole region is used for the verification of radar reflectivity. The blue area is used for the precipitation verification of HyMeX IOP8; the green box indicates the associated area used for HyMeX IOP12b.

7.2 Ensemble performance

In this section, the performance of the five different ensembles to predict precipitation and radar reflectivity of either HyMeX IOP8 or HyMeX IOP12b is evaluated. The ensemble output was compared with measurement data in the area of interest. Whereas precipitation is the output of direct interest, the radar reflectivity has the advantage to be available continuously over larger areas on land and over the Mediterranean Sea. Several different sized areas were considered for the verification of the ensembles (Fig. 7.1). The largest area is studied for both cases and reaches from $9°$W to $5°$E and from $35°$N to $45°$N. To evaluate the accordance with measurement data, a zoom in the areas of interest was performed. For HyMeX IOP8, the specific area of investigation was defined from $7.5°$W to $1°$E and from $36°$N to $41°$N (Fig. 7.1, blue box). For HyMeX IOP12b the borders of the smaller area are defined from $1.5°$W to $4.5°$E and from $38°$N to $42°$N (Fig. 7.1, green box).

To make a statement about the quality of each ensemble, various statistical scores, described in section 3.3.5, were calculated. After an overview about the different general ensemble verification indices, rank histograms are interpreted concerning the ensemble spread. To highlight the relationship between hit rates and false alarm rates of the ensembles, ROC curves are also discussed.

7.2.1 Ensemble spread

Sensitive forecast areas

Before focusing on the verification of each of the 10 experimental ensemble forecasts, the ensembles themselves are investigated regarding their internal variability. Therefore, the 90% percentile of the 24 h accumulated precipitation field and the ensemble interquartile range is analyzed. As predictor for the verification analysis, 24 h accumulated precipitation fields are chosen. For HyMeX IOP8, the rainfall accumulation was calculated from 28 September 2012, 0000 UTC until 29 September 2012, 0000 UTC. For HyMeX IOP12b, the time period between 12 October 2012, 0000 UTC and 13 October 2012, 0000 UTC is studied. To visualize the ensemble spread, the interquartile range of 40 mm is used to highlight regions with large uncertainty in the precipitation forecast (Figs. 7.2 and 7.3).

Regarding the precipitation fields, it can be stated that the domain averaged precipitation of *Ensemble 16 × 1* is for both case studies much higher than the associated one of *Ensemble 1 × 16*. Due to more large-scale realizations in *Ensemble 16 × 1*, larger parts in the area of interest are covered by simulated precipitation of at least one ensemble member. The effect is slightly more pronounced for HyMeX IOP8, where the stronger synoptic forcing leads to approximately 25% more average precipitation in *Ensemble 16 × 1*. For HyMeX IOP12b, the resulting impact on the area affected by precipitation is weaker. The smaller variations in the phase space of the initial conditions is resulting in a smaller geographical area over the model domain.

An interquartile range of 40 mm was chosen to identify areas with prominent ensemble spread. For both case studies, areas with significant ensemble spread are large for ensembles with more synoptic-scale uncertainty, where higher variability is introduced by the diversity introduced at the large synoptic-scale of the predictor fields. The surrounded regions are thus spatially smallest for *Ensemble 1 × 16*. But it is also remarkable that even the small-scale variability introduced by the Plant-Craig scheme is in some regions larger than 40 mm.

Overall it can be seen that generally the ensemble spread is larger the more synoptic-scale members were used to set-up the ensemble. It has to be analyzed for both cases of heavy precipitation, HyMeX IOP8 and HyMeX IOP12b, which combination of large-scale and small-scale uncertainty is best compared to the spread of the meteorological observations.
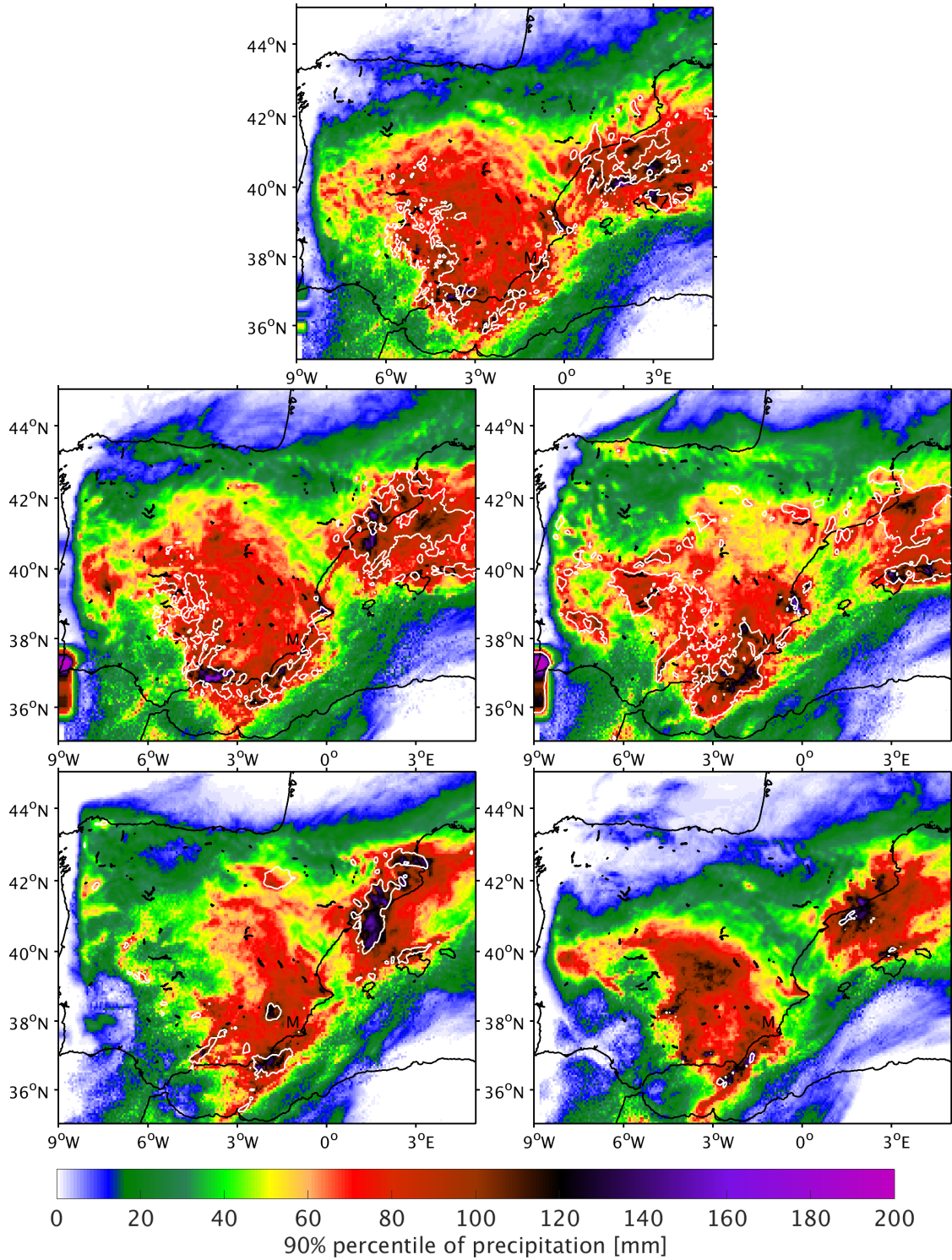
Figure 7.2: 90% percentiles of the 24 h accumulated precipitation fields (colored) from 28 September 2012, 0000 UTC and 40 mm of ensemble interquartile range (white isolines). All ensemble settings are shown in the order "*Ensemble 16 × 1*", "*Ensemble 8 × 2*", "*Ensemble 4 × 4*", "*Ensemble 2 × 8*", "*Ensemble 1 × 16*".
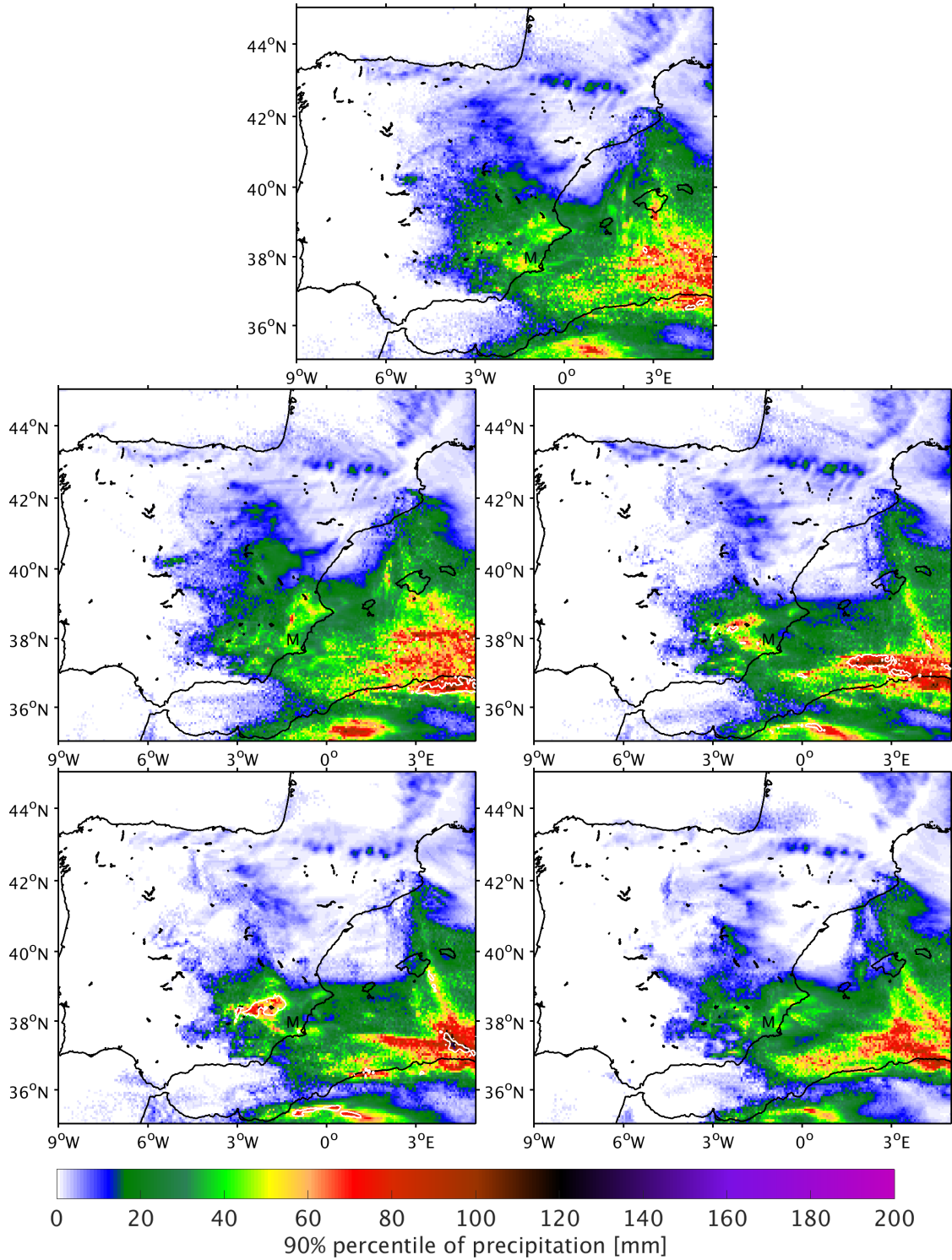
Figure 7.3: 90% percentiles of the 24 h accumulated precipitation fields (colored) from 12 October 2012, 0000 UTC and 40 mm of ensemble interquartile range (white isolines). All ensemble settings are shown in the order "*Ensemble 16 × 1*", "*Ensemble 8 × 2*", "*Ensemble 4 × 4*", "*Ensemble 2 × 8*", "*Ensemble 1 × 16*".
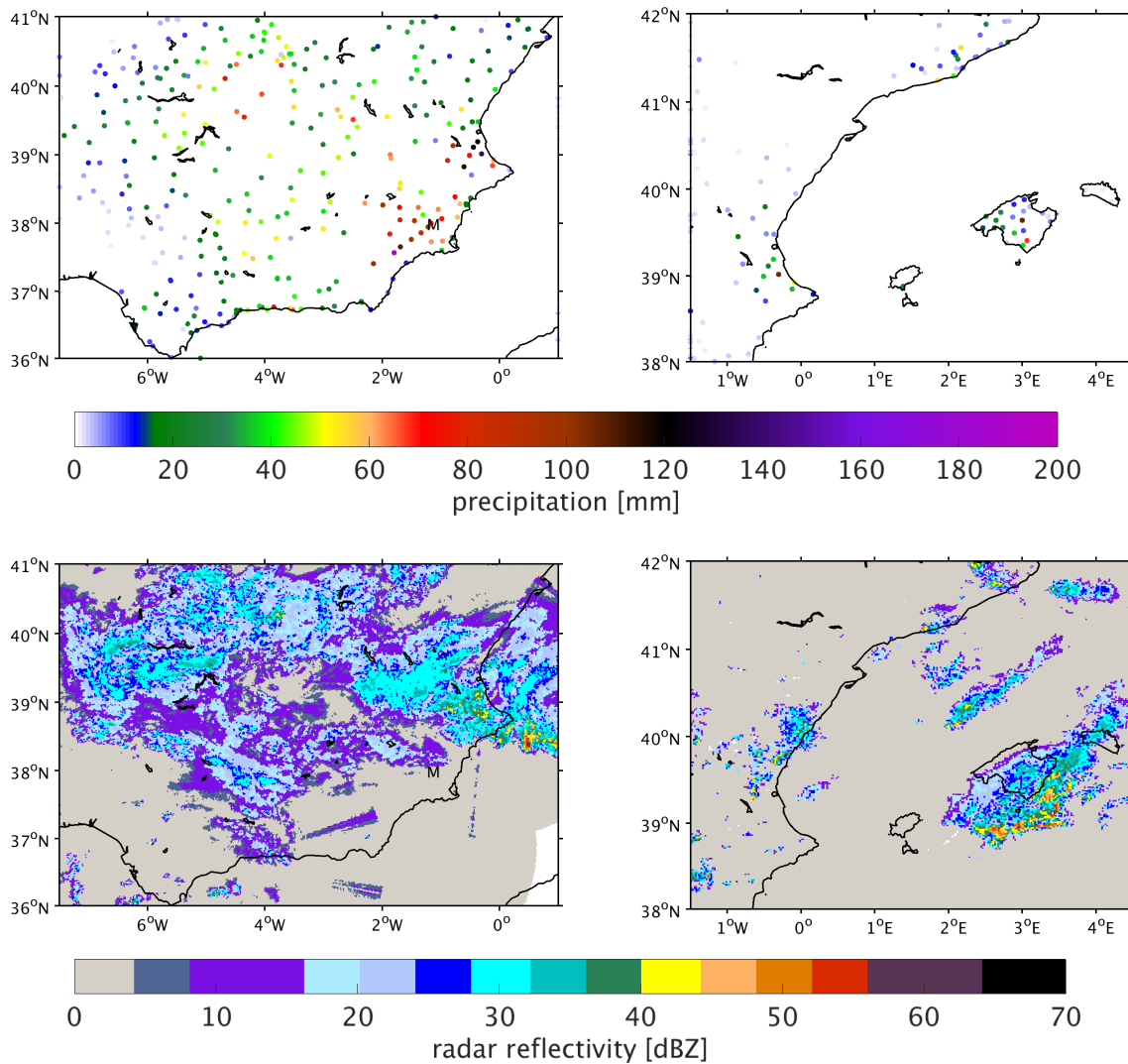
Figure 7.4: Measured 24 h accumulated precipitation (top) and observed radar reflectivities at 1500 UTC on 28 September 2012 (bottom left) and at 1400 UTC on 12 October 2012 (bottom right) in the specific areas of investigation for HyMeX IOP8 (left) and HyMeX IOP12b (right).

Ensemble spread vs. variability of observations

All five introduced ensemble settings are studied now concerning the fact, whether they encompass all plausible scenarios compatible with the information about the state of the atmosphere and its evolution. In the perfect case, the non-parametric range of the plausible predicted states should be sampled uniformly. To visualize this behavior, rank histograms (sec. 3.3.5) are used. For their calculation, observations of raingauges and radar systems are taken into account. A well calibrated ensemble should show a flat rank histogram, which would reveal that each bin defined by the range between ranked ensemble members is equally likely. As the expectable precipitation is the variable of highest interest, rank histograms were calculated first for the comparison of simulated and measured 24 h accumulated precipitation amounts. The studied time periods are the same as used
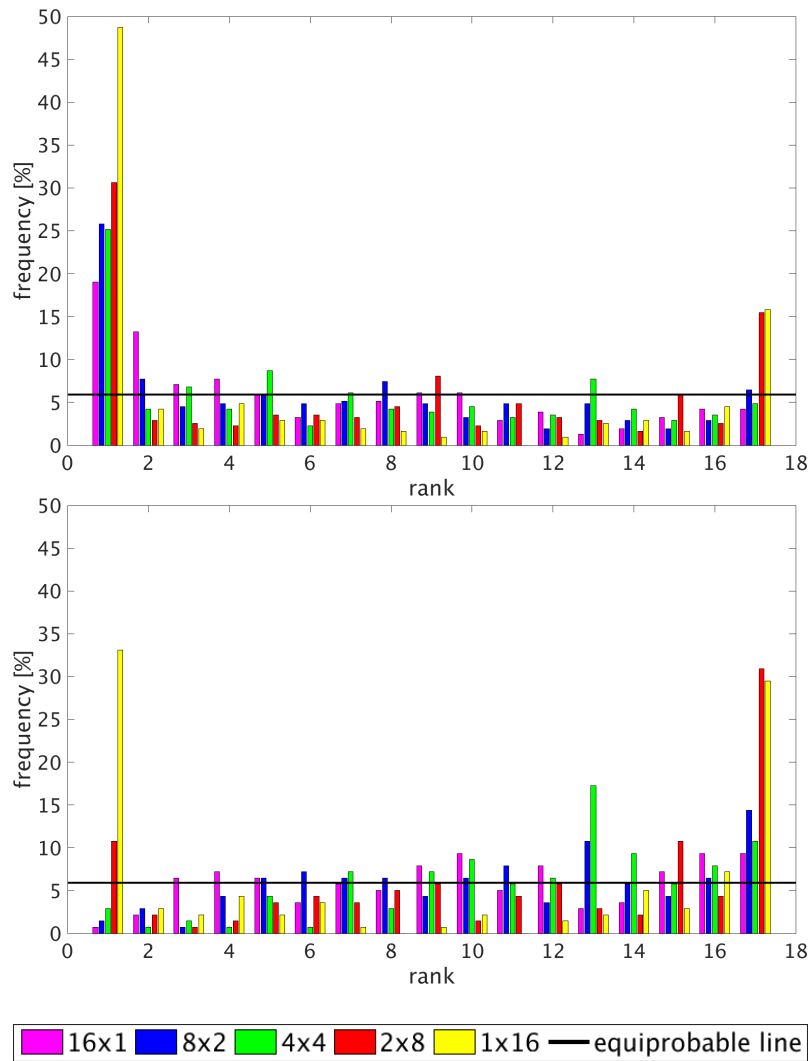
Figure 7.5: Rank histograms for HyMeX IOP8 based on the 24 h accumulated precipitation field. Top: All data included. Bottom: Extreme values of more than 30 mm.

in the prior section. To concentrate on the meteorological raingauges that measured the heavy rain events, the following investigations were performed for two smaller areas (Fig. 7.1, blue and green box). They were taken based on the associated 24 h accumulated precipitation amounts, measured by raingauges, for both events (Fig. 7.4, top).

All available surface weather station measurements were taken into account for both case studies. A first finding for HyMeX IOP8 is a positive bias in the rank histogram (Fig. 7.5, top). The fact that a large quantity of observations was assigned to rang number "1" shows that all ensemble members predicted more precipitation than measured for those cases. This positive bias is most likely for the chosen threshold value of $0\,\mathrm{mm}\,24\,\mathrm{h}^{-1}$. After Dierer et al. (2009), typical forecast errors of numerical weather prediction models are the overestimation of stratiform rain and the underestimation of convective precipitation, whereas the precipitation forecast is very sensitive on the initially available moisture as well as the chosen parameterization scheme for deep convection. Regarding the higher
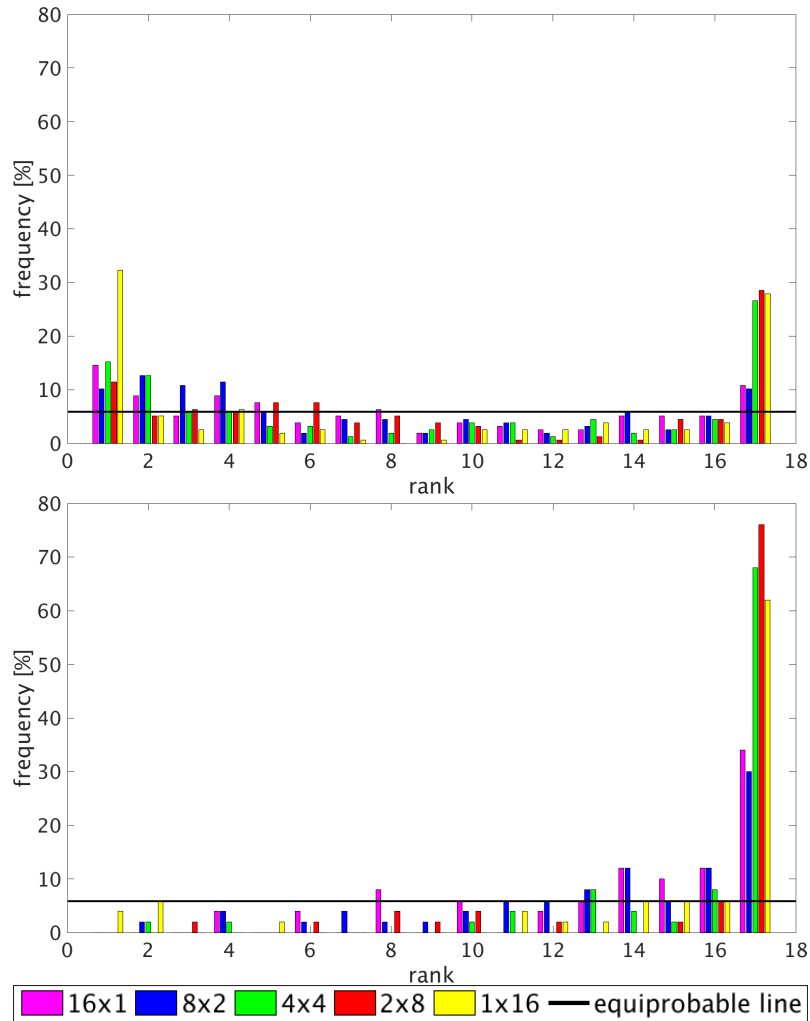
Figure 7.6: Rank histograms for HyMeX IOP12b based on the 24 h accumulated precipitation field. Top: All data included. Bottom: Extreme values of more than 5 mm.

ranks for HyMeX IOP8, they are approximately equally distributed for *Ensembles 16 × 1*, *8 × 2* and *4 × 4*. In contrary, *Ensembles 2 × 8* and *1 × 16* are showing a negative bias. Involving the rank numbers in between, a pronounced U-shaped form results for those two ensembles. This means that these ensembles are underdispersive, i.e. the ensemble spread is here smaller than the measured variability. These findings are confirming the hypothesis that in a synoptically strongly forced case, more large-scale variability is needed to reproduce the uncertainty of the meteorological situation.

For HyMeX IOP12b (Fig. 7.6, top), a U-shaped form is represented in *Ensembles 2 × 8* and *1 × 16*, too. Unexpectedly, the other ensembles have a similar behavior. The underdispersiveness is less pronounced for *Ensembles 8 × 2* and *16 × 1*, but nevertheless identifiable as well.

As both HyMeX IOPs are heavy precipitation events, the rank histograms are studied also for high rainfall amounts. For HyMeX IOP8, a threshold value of more than $30\,\text{mm}\,24\,\text{h}^{-1}$
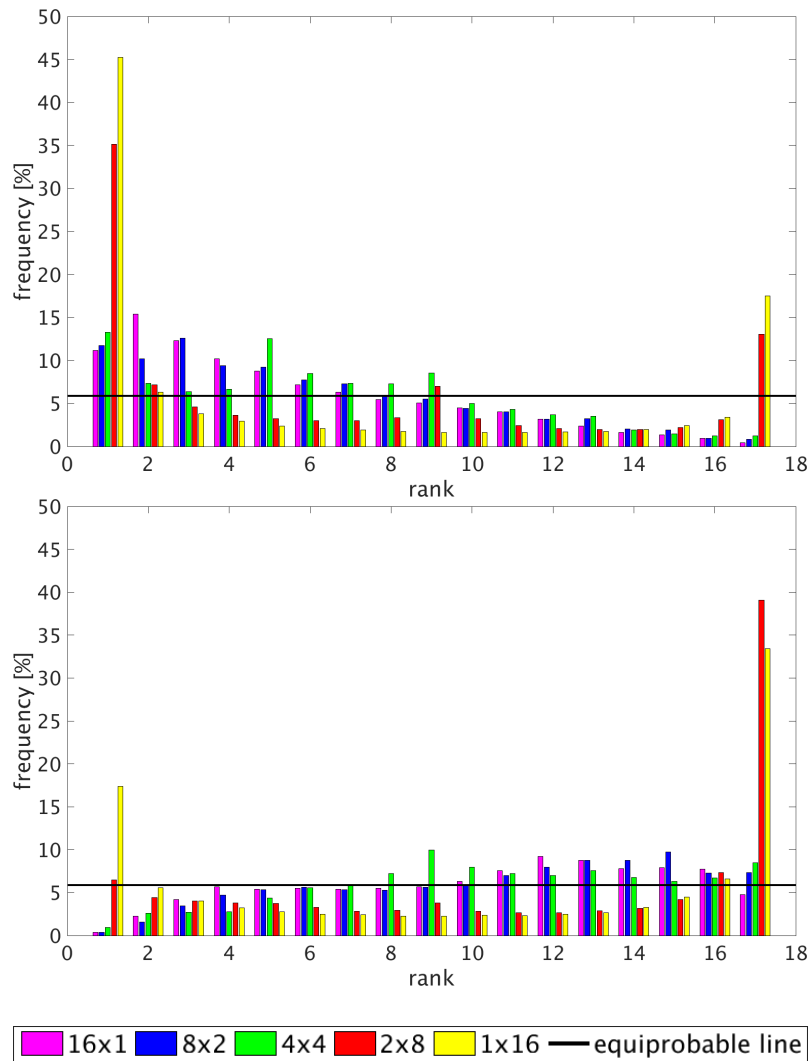
Figure 7.7: Rank histograms for HyMeX IOP8 based on averaged hourly radar reflectivity fields. Top: All data included. Bottom: Extreme values of more than 30 dBZ.

was used. Due to very few surface station measurements for HyMeX IOP12b and due to the lower maximum precipitation values for this case, the threshold value was set here to $5\,\mathrm{mm}\,24\,\mathrm{h}^{-1}$. In contrary to the threshold value of $0\,\mathrm{mm}\,24\,\mathrm{h}^{-1}$, a clear bias can be observed here for both case studies for increasing rank numbers (Figs. 7.5 and 7.6, bottom). This corresponds to the above mentioned problem of the numerical simulation of heavy precipitation events. For HyMeX IOP8, underdispersiveness is only present for the two ensembles with most small-scale uncertainty. *Ensembles 4 × 4, 8 × 2* and *16 × 1* show thus a better performance for heavy rainfall amounts. The hypothesis that a certain amount of large-scale uncertainty is needed to get acceptable dispersion in the forecast of the rainfall amount of this strongly synoptic forced situation is proven again.

For HyMeX IOP12b, the variability of the rainfall over Mallorca is not reproducible with most of the deployed ensembles. Only the 90% percentile of *Ensemble 16 × 1* has some signal over the southern part of the Island (Fig. 7.3). It is the only ensemble that provides an indication of the heavy rainfall due to an isolated MCS of more than $100\,\mathrm{mm}\,24\,\mathrm{h}^{-1}$,
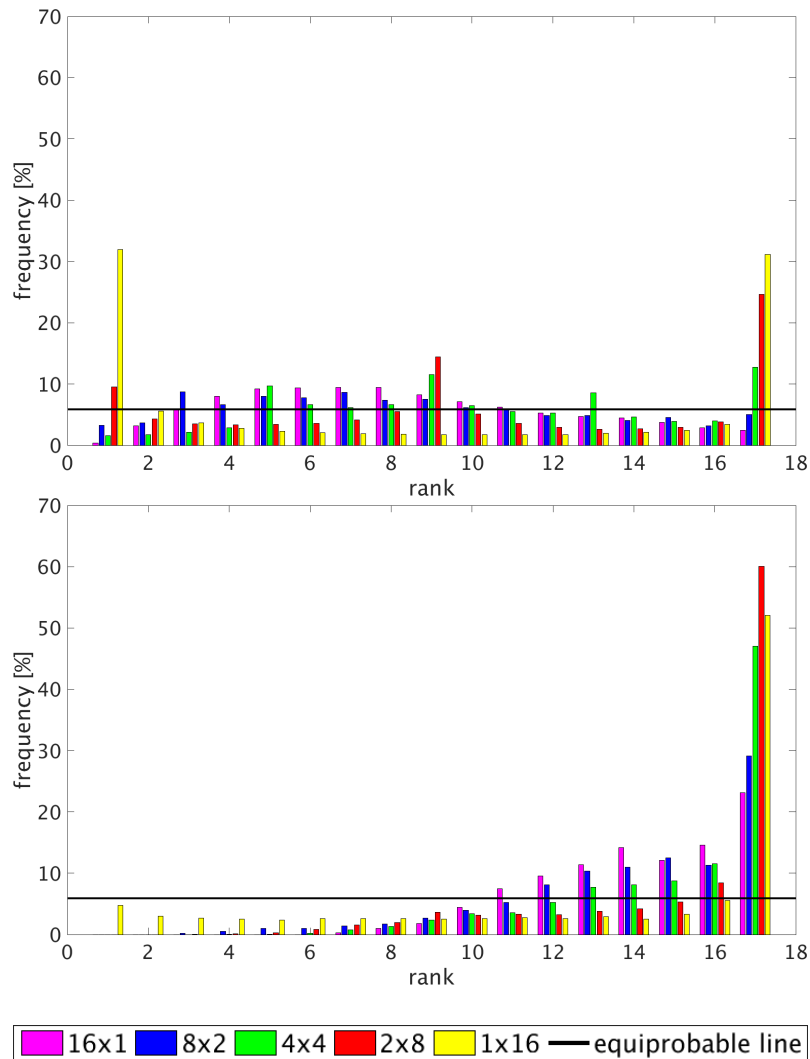
Figure 7.8: Rank histograms for HyMeX IOP12b based on averaged hourly radar reflectivity fields. Top: All data included. Bottom: Extreme values of more than 30 dBZ.

registered in the center of the island. The settings of *Ensembles 1 × 16*, *2 × 8* and *4 × 4* led to frequencies of more than 60% for the highest rank number (Fig. 7.6, bottom). In all these cases, the measured precipitation was thus higher than simulated. This feature can have several reasons. One might be the fact that Mallorca is situated at the edge of the simulated precipitation area. The main heavy precipitation area for HyMeX IOP12b is located south of Mallorca, near the African coast (Fig. 7.3). This could indicate systematic problems of the ECMWF-EPS, of COSMO or of the clustering algorithm to produce the heavy rainfall in the correct geographic location. Maybe it would be possible in the core region of the simulated precipitation fields to validate the hypothesis that less large-scale uncertainty is needed for the prediction of the heavy precipitation during HyMeX IOP12b and that added variability by the Plant-Craig scheme would then lead to a better representation of the natural variability of convective clouds.

Apart from that, conclusions derived from the rank histograms are hindered by the few number of meteorological raingauges observations for both case studies, but especially for HyMeX IOP12b. For HyMeX IOP8, 310 surface stations could be used in total. Precipitation amounts of more than $30\,\mathrm{mm}\,24\,\mathrm{h}^{-1}$ were measured by only 139 stations. For HyMeX IOP12b, only 50 stations (of 158 in total) remained for precipitation amounts of more than $5\,\mathrm{mm}\,24\,\mathrm{h}^{-1}$. To overcome this lack of available measurements, data from radar systems are compared in the following with the simulated radar reflectivity of the ensemble simulations. Radar systems have the great advantage that their measurements cover a large spatial region. Besides, the spatial resolution is very high. For both IOPs significant radar reflectivity was present in major parts in the area of interest (Fig. 7.4, bottom). Thus, a large number of model grid points could be evaluated. As it is not meaningful to accumulate reflectivity values over several hours, another procedure was selected here to gain the resulting rank histograms. For the COSMO simulations, reflectivity values were computed every hour. For each hour, a rank histogram was calculated with the temporally nearest available radar measurement data. After, the mean of all rank histograms was taken so that an averaged rank histogram resulted.

First, all reflectivity larger than $0\,\mathrm{dBZ}$ is studied for HyMeX IOP8 (Fig. 7.7, top). Like for the precipitation, a positive bias to low rank number exists. This bias is less pronounced for the *Ensembles 4 × 4, 8 × 2* and *16 × 1*, which supports the hypothesis for the need of more large-scale variability to cover the evolution of the uncertainty region in the phase space. For higher reflectivity values over $30\,\mathrm{dBZ}$ (Fig. 7.7, bottom), an inverse bias exists. The ensembles have difficulties to reproduce prominent reflectivity values. The underdispersiveness for *Ensembles 2 × 8* and *1 × 16* and the overall flatter rank histograms for ensembles with more different large-scale members strengthens the above mentioned hypothesis also for extreme reflectivity values.

Regarding HyMeX IOP12b, the data basis for radar reflectivity is significantly higher than for the surface stations (Fig. 7.4, right panels). The associated rank histograms are thus statistically more significant. By investigating all radar measurements, the five ensembles show a quite different behavior (Fig. 7.8, top). Whereas underdispersiveness is present for *Ensembles 1 × 16* and *2 × 8*, the other ensemble show already overdispersiveness (dome-shaped) structures. Especially for *Ensembles 16 × 1* and *8 × 2*, a characteristic hill shape results. This result corresponds to the hypothesis that a weaker synoptically forced case may need less large-scale uncertainty to represent the natural variability of precipitation. The behavior is not reflected in the rank histograms for the 24 h accumulated precipitation amount. Probably this is due to the fact that main precipitation areas were simulated over the Mediterranean Sea, where no raingauges exists for a probabilistic verification. Also for more extreme reflectivity values, this feature is not mapped (Fig. 7.8, bottom). Here, the strong bias towards higher rank numbers indicates that the ensembles were not able to reproduce extreme radar reflectivity values.

7.2.2 Discrimination between events and non-events

In addition to the rank histograms, ROC curves (sec. 3.3.5) are used in this section to investigate the quality of each experimental ensemble configuration in discriminating between certain predictors. With concentration on extreme events, precipitation threshold
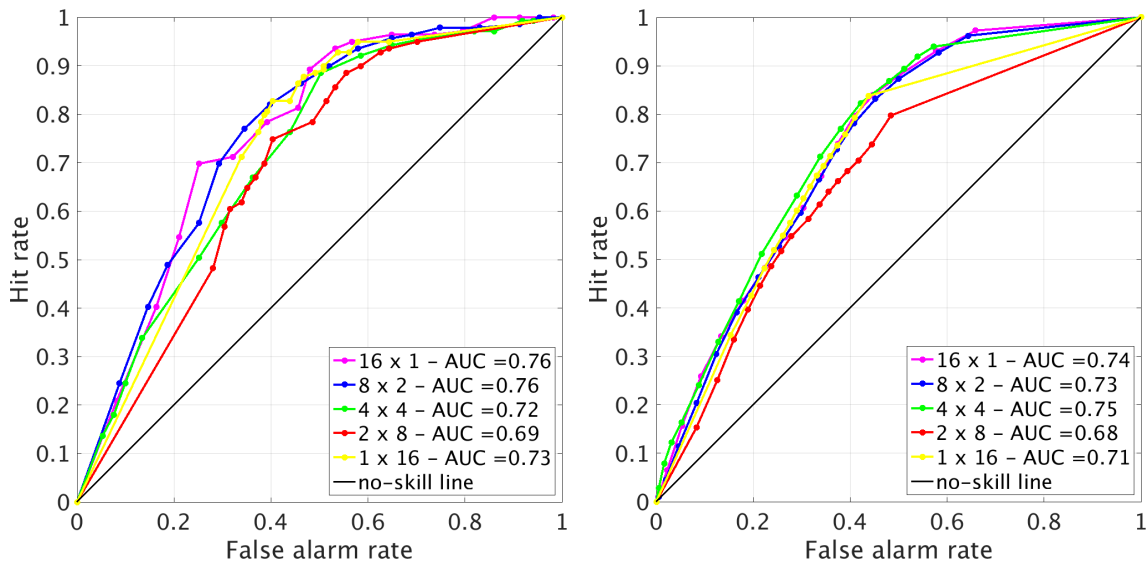
Figure 7.9: ROC curves for HyMeX IOP8. Left: 24 h accumulated precipitation threshold value of more than 30 mm. Right: Hourly reflectivity threshold value of more than 30 dBZ. These mean ROC curves are based on the hourly curves between 28 September 2012, 1000 UTC until 29 September 2012, 0000 UTC.

values of more than $30\,\mathrm{mm}\,24\,\mathrm{h}^{-1}$ (HyMeX IOP8) and $5\,\mathrm{mm}\,24\,\mathrm{h}^{-1}$ (HyMeX IOP12b) and radar reflectivity values of more than 30 dBZ (both cases) are used as predictors. As for the rank histograms, the ROC curves for the comparison of simulated and measured radar reflectivity are averaged for all available single hours.

The resulting ROC curves for precipitation and radar reflectivity comparison during Hy-MeX IOP8 (Fig. 7.9) follow the classical and plausible structure: for high probability thresholds, so for low percentiles, small hit rates (eq. 3.15) and small false alarm rates (eq. 3.16) are resulting. With increasing percentile, a higher hit rate, but also a higher false alarm rate results. Regarding the ROC curve based on precipitation, the areas under the ROC curves (AUC: eq. 3.17) reach values between 0.69 and 0.76 (Fig. 7.9, left). The associated values derived from radar reflectivity data are significantly smaller with values between only 0.58 and 0.67 (not shown). One reason for this worse behavior could be the lack of observational data during the morning hours on 28 September 2012 (see also sec. 5.2). Therefore, the shown ROC curve for radar data (Fig. 7.9, right) was calculated for the hours from 1000 UTC on 28 September 2012 until 29 September 2012, 0000 UTC. Now, the resulting AUC values are within 0.68 to 0.75 very similar to the associated AUC values from the ROC curves gained by precipitation data. From the afore formulated hypothesis, it is expected that a synoptically strongly forced case needs a relatively high amount of large-scale uncertainty to capture best the natural variability of heavy precipitation. This theory is reflected in the quality of the ROC curves for HyMeX IOP8, where quality is diminishing from *Ensemble 16 × 1* to *Ensemble 2 × 8*. *Ensemble 16 × 1* captures best the meteorological uncertainty of this synoptically strongly forced case. The added variability from the Plant-Craig scheme may be responsible for the fact that *Ensembles 8 × 2* and *4 × 4* have comparable skill to *Ensemble 16 × 1*. But by sampling the
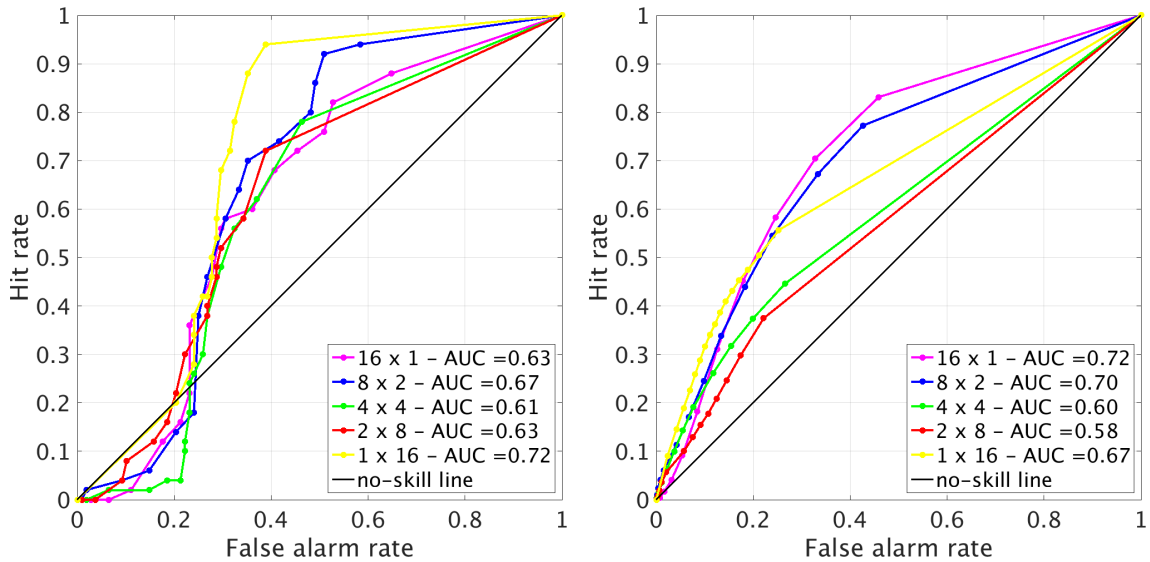
Figure 7.10: ROC curves for HyMeX IOP12b. Left: 24 h accumulated precipitation threshold value of more than 5 mm. Right: Hourly reflectivity threshold value of more than 30 dBZ.

initial and boundary conditions uncertainty with only two samples, the quality decreases significantly and leads to worse AUC values for *Ensemble 2 × 8*. An exception of this behavior is *Ensemble 1 × 16*. Even with only one large-scale situation, the quality of the ROC curve is increasing again. One hypothesis for that fact is that the control forecast of ECMWF-EPS, which was used for this ensemble by default, produces COSMO initial conditions close enough to reality so that the small-scale amplitude perturbations added by the Plant-Craig scheme successfully encompass the actual event. Supposing that all members of ECMWF-EPS are alike, this hypothesis would mean that the better skill of *Ensemble 1 × 16* is due to a matter of chance. The effect that the performance of a nested forecast is strongly correlated to the accuracy of the initial conditions was also found in further ensemble studies concerning the prediction of heavy precipitation (e.g. Barrett et al., 2015).

Regarding the AUC values for the ROC curves of HyMeX IOP12b, created with precipitation data, *Ensemble 1 × 16* provides with 0.72 the best score of all five ensembles (Fig. 7.10, left). The control forecast thus seem to have the same tendency as for HyMeX IOP8. The skill of the other four ensembles almost decreases continuously from *Ensemble 16 × 1* down to *Ensemble 2 × 8*, but has a local maximum AUC value for *Ensemble 8 × 2*. Following these observances, it can be supposed that 16 or 8 large-scale situations are necessary to represent the meteorological uncertainty. With sufficient 8 large-scale members, the ensemble spread may be further improved by the use of the stochastic Plant-Craig scheme. With only 4 or 2 different large-scale initial conditions, the ensemble is not able to discriminate between events and non-events. Concerning the overall structure of the discussed ROC curves for HyMeX IOP12b, a deviation of the expected shape can be stated. For low percentiles, the false alarm rate is significantly higher than the associated hit rate. Only with percentiles higher than approximately 30%, the

ROC curve is positioned above the no-skill line. One hypothesis for this behavior is that many ensemble members are forecasting high precipitation values in regions where less precipitation was measured. But it could also result from the very low number of only 50 raingauge measurements above $5\,\mathrm{mm}\,24\,\mathrm{h}^{-1}$.

Comparing the radar-based ROC curves with the precipitation-based ones, the continuous quality decrease from *Ensemble 16 × 1* to *Ensemble 2 × 8* can be remarked, too (Fig. 7.8). *Ensemble 1 × 16* performs again better than expected but does not outperform all other ensembles. The shape of the ROC curves follows the expected form so that it is supposed again that a statistically underrepresentation of measured heavy precipitation led to the untypical shape of the precipitation-based ROC curves.

In accordance with the above discussed rank histograms for extreme meteorological values, the ROC curves for HyMeX IOP12b do not indicate that an ensemble setting with less large-scale variability (in favor of more small-scale variability) performs better for the prediction of severe weather in a synoptically weakly forced situation.

Summary

In this chapter, the contribution of different sources of uncertainty on the prediction of two differently forced heavy precipitation events in the western Mediterranean was studied. The first fraction of variability is derived via perturbations in the initial conditions. The second part is gained by stochastic variations in the parameterization scheme for cumulus convection in the numerical weather prediction model. A continuously varying percentage of both sources of uncertainty is managed through five ensembles with each time 16 members. To combine synoptic-scale and convective-scale variability in one ensemble is a quite novel approach. The procedure is based on the hypothesis that the predictability of a synoptically strongly forced case is better represented when large-scale uncertainty is high, whereas a weaker synoptically forced event is supposed to be less dependent on the synoptic scale. In such a case it is hypothesized that remaining resources due to less perturbations in the initial conditions may be used for additional variability on the small-scale. Then, a more accurate forecast of the natural variability of convective clouds could be achieved.

HyMeX IOP8, the synoptically strongly forced case, was contrasted with HyMeX IOP12b, a synoptically weaker forced case. For HyMeX IOP8 it was found that the above mentioned was fulfilled: the more large-scale uncertainty the ensemble included, the better the scores were. This relationship could be found for all studied rank histograms (flatter structure for ensembles with 16, 8 or 4 different initial conditions) as well as for the ROC curves based on extreme threshold values (decreasing quality from AUC = 0.74 for *Ensemble 16 × 1* to AUC = 0.68 for *Ensemble 2 × 8*) of the analyzed meteorological variables. For HyMeX IOP12b, the conclusions were not that pronounced. The complete reflectivity-based rank histogram points to the assumption that 16 or 8 large-scale initial conditions are necessary to encompass the actual event. For extreme threshold values for precipitation and radar reflectivity, synoptic uncertainty is found to be very important, even in this weakly forced event.

8 Summary and Outlook

In this thesis, two convective heavy precipitation events that affected the western Mediterranean area in autumn 2012 were studied. Whereas the first event on 28 September 2012 (HyMeX IOP8) led to daily rainfall amounts partly higher than 200 mm along the Spanish Mediterranean coast, more than 100 mm were measured on the Balearic Islands during the second case on 12 October 2012 (HyMeX IOP12b). The large-scale synoptic conditions differed significantly regarding their strength. An upper-level cut-off low with an associated surface low-pressure system were the determining synoptic features during HyMeX IOP8. The synoptic-scale forcing was much weaker during HyMeX IOP12b, where a mean zonal flow was disturbed by secondary short-wave troughs.

To understand the initiation and the development of HyMeX IOP8, an extensive diagnostic study was performed for this case. First, the preconditions for deep moist convection were analyzed in detail. After Doswell et al. (1996), three ingredients are necessary: a high moisture content in the lower troposphere, a potential unstable atmosphere and a lifting mechanism to trigger possible deep moist convection. An analysis based on measurements of meteorological surface stations as well as on a high-resolution numerical model simulation revealed that the first requirement was fulfilled for large regions within the western Mediterranean area. High moisture was naturally present over the Mediterranean Sea. But also at large parts along the Spanish Mediterranean coast, warm and humid airmasses indicated areas with suitable low-level conditions. Conclusions from radiosoundings at Murcia and Palma de Mallorca pointed to different characteristics of the vertical atmospheric instability over those two locations. In Murcia, the atmosphere was slightly unstable until 1200 UTC. By 1800 UTC, instability was released and a stable profile resulted in the lower levels. Over Palma de Mallorca, a strong inversion zone in mid-levels determined the situation. Although a strong low-level potential instability developed during the day, it was blocked by the overlying inversion. A lifting mechanism that could have removed the inversion was missing at Palma for the whole studied time period. Thus, deep convective processes were inhibited in this region. This fact was underlined by corresponding weak vertical velocities in upper-levels. However, two possible trigger mechanisms for the release of potential instability near Murcia were found. One is a low-level mesoscale convergence line. Westerly airmasses arriving from the Strait of Gibraltar and easterly airmasses coming from the Mediterranean Sea converged at a sharp frontal zone, linked to the surface low-pressure system. The boundary line was already detected in the near surface-level fields of relative moisture and temperature and was reproduced very well in the associated model simulated field of equivalent potential temperature Θ_e. Very prominent, the convergence line was reflected by wind measurements and simulations in 10 m height. The analysis of two following time steps at 0900 UTC and 1500 UTC showed a northeasterly movement of the convergence line with a displacement

speed of about $60 \, \mathrm{km \, h^{-1}}$. This movement was forced by the cut-off-low in upper-levels. As a second trigger mechanism, an influence of the steep orography with heights up to more than $3000 \, \mathrm{m}$ at the Spanish Mediterranean coast was suspected. An interaction with the incoming flow from the Mediterranean Sea was found to be likely for orographic lifting effects.

The resulting heavy precipitation during HyMeX IOP8 occurred primarily in the regions which were found as favorable for deep moist convection. Especially the hotspot around Murcia was very pronounced in the raingauges measurements. Also the high-resolution numerical simulation captured this distribution. Over the sea, the model output was verified against satellite derived precipitation estimates. With main focus on the structure of a 3-hourly accumulated rainfall period, a satisfying accordance was achieved between both datasets. Also the comparison with an additional numerical model, particularly designed for the western Mediterranean area, revealed a very good performance of the chosen high-resolution simulation. In particular, the peak of the heavy precipitation event was simulated very similarly in both models. A further analysis of the numerical model simulations was performed concerning radar reflectivity values. The output from radar systems was used as highly correlated measure of precipitation. In contrary to the raingauges, which are only available over land, the radar stations can deliver measurements in a wide radius even over the sea. With the evaluated European composite, almost the whole area of interest was covered with spatially dense observational data. To diagnose the quality of the numerical simulation in comparison to the radar data, the spatial verification method SAL (Wernli et al., 2008) was applied. An almost perfect correspondence resulted with respect to the structure of the reflectivity patterns in both datasets. Regarding the intensity of the reflectivity patterns, the numerical model overestimated the measured values.

Based on the satisfying results concerning the general performance of the high-resolution model, the simulation was used to conduct a deeper investigation of the physical processes involved in HyMeX IOP8. The atmospheric stability was analyzed over several distinct points over land and over the Mediterranean Sea. Over the sea, strong potential instability was present at 1200 UTC, whereas vertical gradients of Θ_e were much weaker over land. At around 1500 UTC, the potential instability was released for both regions. Regarding the situation over the sea, this procedure could be linked directly to the passage of the horizontal wind convergence line. The resulting hourly precipitation amount of about $10 \, \mathrm{mm}$ was found to be fed by Mediterranean sea surface moisture. Over land, the moist convection triggered by the convergence line was superimposed by orographic effects. Significant upslope winds in the region around Murcia point to classical orographic lifting as trigger for deep moist convection and associated precipitation. Most prominent upslope values occurred isochronically with strongest rainfall. A sensitivity numerical experiment, in which the orography of the western Mediterranean area was flattened to a height of $10 \, \mathrm{m}$, verify this assumption. With removed orography, significantly less precipitation was simulated in the vicinity of Murcia. To study the moisture origins for HyMeX IOP8, a further numerical study was performed. With the calculation of forward Lagrangian trajectories, moisture sources of the Atlantic Ocean and of the Mediterranean Sea itself were found as crucial. Whereas Atlantic moisture precipitated in southern Spain, Mediterranean humid air fed the heavy precipitation systems between Murcia and Valencia along the Spanish Mediterranean coast.

A big challenge in the numerical weather forecast is the prediction of heavy precipitation events like HyMeX IOP8 and HyMeX IOP12b. To study their predictability, a quite novel approach was applied in this thesis. For both case studies, five different ensemble forecasts were performed. The ensembles consist of different percentages of synoptic-scale uncertainty and convective-scale uncertainty, introduced by a stochastic parameterization scheme for cumulus convection (Plant and Craig, 2008). It was assumed that the synoptically stronger forced case HyMeX IOP8 would need more numerical large-scale uncertainty to encompass the meteorological situation. By contrast, the ensemble spread of the weaker forced case HyMeX IOP12b is supposed to need fewer large-scale uncertainty and that an added value can be gained by the small-scale stochastic perturbations. With the aid of various statistical probabilistic scores, the performance of all five ensembles was studied for both heavy rain events. As comparative measures to the output of the single ensemble members, raingauges measurements and the output from radar systems were used. Rank histograms were calculated to evaluate the ensemble spread in comparison to the variability of the observations. ROC curves highlight the ability of an ensemble to discriminate between a severe rain event and a non-event.

For HyMeX IOP8, ensembles with 50% or more of synoptic-scale uncertainty have clearly better quality than ensembles with more convective-scale uncertainty. Within the studied rank histograms, overall flatter, thus more reliable, structures result for large-scale driven ensembles. Also the skill of the ROC curves is generally decreasing towards ensembles with less synoptic-scale variability.

Concerning HyMeX IOP12b, the initially stated hypothesis was confirmed with respect to the rank histogram based on the complete set of radar reflectivity data. As expected, a too large spread occurred for the two ensembles with more than 50% of synoptic-scale uncertainty. The best performance is found here for the ensemble where large-scale and small-scale uncertainty are equally quantified. Regarding extreme threshold values, a large impact of the synoptic-scale was found in rank histograms and in the ROC curves. This leads to the assumption that synoptic uncertainty is very important, even in this weakly forced event.

The novel approach to construct an ensemble prediction system with mixed-scale uncertainty is found to be very promising for future research projects. Within this thesis, two single case studies were evaluated with the newly introduced methodology. Strong indications were found for the assumption that the combination of synoptic- and convective-scale uncertainty could be an appropriate tool to forecast differently forced heavy precipitation events. To diagnose whether the presented ensemble can be used in an adaptive way, further cases should be evaluated. With more investigated events, statistical significance of the evaluation can be achieved.

List of Figures

List of Tables

Bibliography

Adler, B., N. Kalthoff, M. Kohler, J. Handwerker, A. Wieser, U. Corsmeier, C. Kottmeier, D. Lambert, and O. Bock, 2015: The variability of water vapour and pre-convective conditions over the mountainous island of Corsica. *Quart. J. Roy. Meteor. Soc.*, doi: 10.1002/qj.2545.

Ahijevych, D., E. Gilleland, and B. G. Brown, 2009: Application of spatial verification methods to idealized and NWP-gridded precipitation forecasts. *Wea. Forecasting*, **24**, 1485–1497, doi:10.1175/2009WAF2222298.1.

Alpert, P., T. Ben-Gai, A. Baharad, Y. Benjamini, D. Yekutieli, M. Colacino, L. Diodato, C. Ramis, V. Homar, R. Romero, S. Michaelides, and A. Manes, 2002: The paradoxical increase of Mediterranean extreme daily rainfall in spite of decrease in total values. *Geophys. Res. Lett.*, **29 (11)**, 31–1–31–4, doi:10.1029/2001GL013554.

Amengual, A., V. Homar, and O. Jaume, 2015: Potential of a probabilistic hydrometeorological forecasting approach for the 28 September 2012 extreme flash flood in Murcia, Spain. *Atmos. Res.*, **166**, 10–23, doi:10.1016/j.atmosres.2015.06.012.

Arakawa, A., 2004: The cumulus parameterization problem: past, present, and future. *J. Climate*, **17 (13)**, 2493–2525, doi:10.1175/1520-0442(2004)017⟨2493:RATCPP⟩2. 0.CO;2.

Banacos, P. C. and D. M. Schultz, 2005: The use of moisture flux convergence in forecasting convective initiation: historical and operational perspectives. *Wea. Forecasting*, **20**, 351–366, doi:10.1175/WAF858.1.

Barrett, A. I., S. L. Gray, D. J. Kirshbaum, N. M. Roberts, D. M. Schultz, and J. Jonathan G. Fairman, 2015: The utility of convection-permitting ensembles for the prediction of stationary convective bands. *Mon. Wea. Rev.*, doi:10.1175/MWR-D-15-0148.1.

Barros, S., D. Dent, L. Isaksen, G. Robinson, G. Mozdzynski, and F. Wollenweber, 1995: The IFS model: a parallel production weather code. *Parallel Comput.*, **21**, 1621–1638, doi:10.1016/0167-8191(96)80002-0.

Barry, R. G., 2008: *Mountain weather and climate*. Cambridge University Press, New York, 506 pp.

Barthlott, C., B. Adler, N. Kalthoff, J. Handwerker, M. Kohler, and A. Wieser, 2014: The role of Corsica in initiating nocturnal offshore convection. *Quart. J. Roy. Meteor. Soc.*, doi:10.1002/qj.2415.

Bibliography

Barthlott, C. and D. J. Kirshbaum, 2013: Sensitivity of deep convection to terrain forcing over Mediterranean islands. *Quart. J. Roy. Meteor. Soc.*, **139 (676)**, 1762–1779, doi: 10.1002/qj.2089.

Bjerknes, V., 1904: Das Problem der Wettervorhersage, betrachtet vom Standpunkt der Mechanik und der Physik. *Meteor. Z.*, **21**, 1–7.

Björnsson, H. and S. Venegas, 1997: A manual for EOF and SVD analyses of climatic data. *CCGCR Report*, **97 (1)**, 1–54.

Bolton, D., 1980: The computation of equivalent potential temperature. *Mon. Wea. Rev.*, **108 (7)**, 1046–1053, doi:10.1175/1520-0493(1980)108⟨1046:TCOEPT⟩2.0.CO;2.

Bresson, R., D. Ricard, and V. Ducrocq, 2009: Idealized mesoscale numerical study of Mediterranean heavy precipitating convective systems. *Meteor. Atmos. Phys.*, **103**, 45–55, doi:10.1007/s00703-008-0338-z.

Buzzi, A. and L. Foschini, 2000: Mesoscale meteorological features associated with heavy precipitation in the Southern Alpine region. *Meteor. Atmos. Phys.*, **72 (2-4)**, 131–146, doi:10.1007/s007030050011.

Callado, A., P. Escribà, J. A. García-Moya, J. Montero, C. Santos, D. Santos-Muñoz, and J. Simarro, 2013: *Ensemble forecasting*. InTech, 57 pp., doi:10.5772/55699.

Campins, J., M. Aran, A. Genovés, and A. Jansà, 2007: High impact weather and cyclones simultaneity in Catalonia. *Adv. Geosci.*, **12**, 115–120, doi:10.5194/adgeo-12-115-2007.

Campins, J., A. Genovés, M. A. Picornell, and A. Jansà, 2011: Climatology of Mediterranean cyclones using the ERA-40 dataset. *Int. J. Climatol.*, **31**, 1596–1614, doi: 10.1002/joc.2183.

Campins, J., A. Jansà, and A. Genovés, 2006: Heavy rain and strong wind events and cyclones in the Balearics. *Adv. Geosci.*, **7**, 73–77, doi:10.5194/adgeo-7-73-2006.

Campins, J., B. Navascués, C. Santos, and A. Amo-Baladrón, 2013: Influence of targeted observations on short-term forecasts of high-impact weather events in the Mediterranean. *Nat. Hazards Earth Syst. Sci.*, **13**, 2891–2910, doi:10.5194/ nhess-13-2891-2013.

Chaboureau, J.-P., F. Pantillon, D. Lambert, E. Richard, and C. Claud, 2012: Tropical transition of a Mediterranean storm by jet crossing. *Quart. J. Roy. Meteor. Soc.*, **138**, 596–611, doi:10.1002/qj.960.

Cohen, B. G. and G. C. Craig, 2006: Fluctuations in an equilibrium convective ensemble. Part II: Numerical experiments. *J. Atmos. Sci.*, **63**, 2005–2015, doi:10.1175/JAS3710.1.

Cohuet, J., R. Romero, V. Homar, V. Ducrocq, and C. Ramis, 2011: Initiation of a severe thunderstorm over the Mediterranean Sea. *Atmos. Res.*, **100**, 603–620, doi:10.1016/j. atmosres.2010.11.002.

Corsmeier, U., N. Kalthoff, C. Barthlott, F. Aoshima, A. Behrendt, P. D. Girolamo, M. Dorninger, J. Handwerker, C. Kottmeier, H. Mahlke, S. Mobbs, E. Norton, J. Wickert, and V. Wulfmeyer, 2011: Processes driving deep convection over complex terrain: a multi-scale analysis of observations from COPS IOP 9c. *Quart. J. Roy. Meteor. Soc.*, **137 (S1)**, 137–155, doi:10.1002/qj.754.

Courant, R., K. Friedrichs, and H. Lewy, 1928: Über die partiellen Differentialgleichungen der mathematischen Physik. *Math. Ann.*, **100**, 32–74.

Craig, G. C. and B. G. Cohen, 2006: Fluctuations in an equilibrium convective ensemble. Part I: Theoretical formulation. *J. Atmos. Sci.*, **63**, 1996–2004, doi:10.1175/JAS3709.1.

d'Abreton, P. and P. Tyson, 1996: Three-dimensional kinematic trajectory modelling of water vapour transport over Southern Africa. *Water SA*, **22**, 297–306.

Davies-Jones, R., 2009: On formulas for equivalent potential temperature. *Mon. Wea. Rev.*, **137**, 3137–3148, doi:10.1175/2009MWR2774.1.

Davis, C. A., B. Brown, and R. Bullock, 2006a: Object-based verification of precipitation forecasts. Part I: Methodology and application to mesoscale rain areas. *Mon. Wea. Rev.*, **134**, 1772–1784, doi:10.1175/MWR3145.1.

Davis, C. A., B. Brown, and R. Bullock, 2006b: Object-based verification of precipitation forecasts. Part II: Application to convective rain systems. *Mon. Wea. Rev.*, **134**, 1785–1795, doi:10.1175/MWR3146.1.

Davis, C. A., B. G. Brown, R. Bullock, and J. Halley-Gotway, 2009: The method for object-based diagnostic evaluation (MODE) applied to numerical forecasts from the 2005 NSSL/SPC spring program. *Wea. Forecasting*, **24**, 1252–1267, doi:10.1175/2009WAF2222241.1.

Delrieu, G., V. Ducrocq, E. Gaume, J. Nicol, O. Payrastre, E. Yates, P.-E. Kirstetter, H. Andrieu, P.-A. Ayral, C. Bouvier, J.-D. Creutin, M. Livet, S. Anquetin, M. Lang, L. Neppel, C. Obled, J. P. du Chatelet, G.-M. Saulnier, A. Walpersdorf, and W. Wobrock, 2005: The catastrophic flash-flood event of 8–9 September 2002 in the Gard Region, France: a first case study for the Cévennes–Vivarais Mediterranean hydrometeorological observatory. *J. Hydrometeorol.*, **6**, 34–52, doi:10.1175/JHM-400.1.

Dierer, S., M. Arpagaus, A. Seifert, E. Avgoustoglou, R. Dumitrache, F. Grazzini, P. Mercogliano, M. Milelli, and K. Starosta, 2009: Deficiencies in quantitative precipitation forecasts: sensitivity studies using the COSMO model. *Meteor. Z.*, **18 (15)**, 631–645, doi:10.1127/0941-2948/2009/0420.

Doswell, C. A., 1987: The distinction between large-scale and mesoscale contribution to severe convection: a case study example. *Wea. Forecasting*, **2 (1)**, 3–16, doi:10.1175/1520-0434(1987)002⟨0003:TDBLSA⟩2.0.CO;2.

Doswell, C. A., H. E. Brooks, and R. A. Maddox, 1996: Flash flood forecasting: an ingredients-based methodology. *Wea. Forecasting*, **11 (4)**, 560–581, doi:10.1175/1520-0434(1996)011⟨0560:FFFAIB⟩2.0.CO;2.

Bibliography

Doswell, C. A., C. Ramis, R. Romero, and S. Alonso, 1998: A diagnostic study of three heavy precipitation episodes in the Western Mediterranean region. *Wea. Forecasting*, **13**, 102–124, doi:10.1175/1520-0434(1998)013⟨0102:ADSOTH⟩2.0.CO;2.

Drobinski, P., V. Ducrocq, P. Alpert, E. Anagnostou, K. Béranger, M. Borga, I. Braud, A. Chanzy, S. Davolio, G. Delrieu, C. Estournel, N. F. Boubrahmi, V. G. J. Font, S. Gualdi, V. Homar, B. Ivančan-Picek, C. Kottmeier, V. Kotroni, K. Lagouvardos, P. Lionello, M. C. Llasat, W. Ludwig, C. Lutoff, A. Mariotti, E. Richard, R. Romero, R. Rotunno, O. Roussot, I. Ruin, S. Somot, I. Taupier-Letage, J. Tintore, R. Uijlenhoet, and H. Wernli, 2014: HyMeX: a 10-year multidisciplinary program on the Mediterranean water cycle. *Bull. Amer. Meteor. Soc.*, **95**, 1063–1082, doi: 10.1175/BAMS-D-12-00242.1.

Ducrocq, V., I. Braud, S. Davolio, R. Ferretti, C. Flamant, A. Jansa, N. Kalthoff, E. Richard, I. Taupier-Letage, P.-A. Ayral, S. Belamari, A. Berne, M. Borga, B. Boudevillain, O. Bock, J.-L. Boichard, M.-N. Bouin, O. Bousquet, C. Bouvier, J. Chiggiato, D. Cimini, U. Corsmeier, L. Coppola, P. Cocquerez, E. Defer, J. Delanoë, P. D. Girolamo, A. Doerenbecher, P. Drobinski, Y. Dufournet, N. Fourrié, J. J. Gourley, L. Labatut, D. Lambert, J. L. Coz, F. S. Marzano, G. Molinié, A. Montani, G. Nord, M. Nuret, K. Ramage, W. Rison, O. Roussot, F. Said, A. Schwarzenboeck, P. Testor, J. V. Baelen, B. Vincendon, M. Aran, and J. Tamayo, 2014: HyMeX-SOP1, the field campaign dedicated to heavy precipitation and flash flooding in the northwestern Mediterranean. *Bull. Amer. Meteor. Soc.*, **95**, 1083–1100, doi: 10.1175/BAMS-D-12-00244.1.

Duffourg, F. and V. Ducrocq, 2011: Origin of the moisture feeding the heavy precipitating systems over Southeastern France. *Nat. Hazards Earth Syst. Sci.*, **11 (4)**, 1163–1178, doi:10.5194/nhess-11-1163-2011.

Duffourg, F. and V. Ducrocq, 2013: Assessment of the water supply to Mediterranean heavy precipitation: a method based on finely designed water budgets. *Atmos. Sci. Let.*, **14 (3)**, 133–138, doi:10.1002/asl2.429.

Déqué, M., C. Dreveton, A. Braun, and D. Cariolle, 1994: The ARPEGE/IFS atmosphere model: a contribution to the French community climate modelling. *Clim. Dyn.*, **10 (4-5)**, 249–266, doi:10.1007/BF00208992.

Ebert, E. E., 2001: Ability of a poor man's ensemble to predict the probability and distribution of precipitation. *Mon. Wea. Rev.*, **129**, 2461–2480, doi:10.1175/ 1520-0493(2001)129⟨2461:AOAPMS⟩2.0.CO;2.

Emanuel, K. A., 1994: *Atmospheric convection*. Oxford University Press, New York, 580 pp.

Fita, L., R. Romero, and C. Ramis, 2006: Intercomparison of intense cyclogenesis events over the Mediterranean basin based on baroclinic and diabatic influences. *Adv. Geosci.*, **7**, 333–342, doi:10.5194/adgeo-7-333-2006.

Fourrié, N. and M. Nuret, 2014: Reanalysis AROME-WMED V1. doi:10.6096/HYMEX. REANALYSIS_AROME_WMED_V1.2014.02.10.

Fresnay, S., A. Hally, C. Garnaud, E. Richard, and D. Lambert, 2012: Heavy precipitation events in the Mediterranean: sensitivity to cloud physics parameterisation uncertainties. *Nat. Hazards Earth Syst. Sci.*, **12**, 2671–2688, doi:10.5194/nhess-12-2671-2012.

Garcia-Moya, J.-A., A. Callado, P. Escribà, C. Santos, D. Santos-Muñoz, and J. Simarro, 2011: Predictability of short-range forecasting: a multimodel approach. *Tellus A*, **63**, 550–563, doi:10.1111/j.1600-0870.2010.00506.x.

Garcies, L. . and V. Homar, 2009: Ensemble sensitivities of the real atmosphere: application to Mediterranean intense cyclones. *Tellus A*, **61**, 394–406, doi:10.1111/j. 1600-0870.2009.00392.x.

Garcies, L. and V. Homar, 2010: An optimized ensemble sensitivity climatology of Mediterranean intense cyclones. *Nat. Hazards Earth Syst. Sci.*, **10 (12)**, 2441–2450, doi:10.5194/nhess-10-2441-2010.

Gilleland, E., D. Ahijevych, B. G. Brown, B. Casati, and E. E. Ebert, 2009: Intercomparison of spatial forecast verification methods. *Wea. Forecasting*, **24**, 1416–1430, doi: 10.1175/2009WAF2222269.1.

Giorgi, F., 2006: Climate change hot-spots. *Geophys. Res. Lett.*, **33 (8)**, 1–4, doi:10.1029/ 2006GL025734.

Giorgi, F. and P. Lionello, 2008: Climate change projections for the Mediterranean region. *Glob. Planet. Chang.*, **63 (2-3)**, 90–104, doi:10.1016/j.gloplacha.2007.09.005.

Grams, C. M., H. Wernli, M. Böttcher, J. Campa, U. Corsmeier, S. C. Jones, J. H. Keller, C.-J. Lenz, and L. Wiegand, 2011: The key role of diabatic processes in modifying the upper-tropospheric wave guide: a North Atlantic case-study. *Quart. J. Roy. Meteor. Soc.*, **137**, 2174–2193, doi:10.1002/qj.891.

Groenemeijer, P., 2009: Convective storm development in contrasting thermodynamic and kinematic environments. Ph.D. thesis, Karlsruhe Institute of Technology.

Groenemeijer, P. and G. Craig, 2012: Ensemble forecasting with a stochastic convective parameterization based on equilibrium statistics. *Atmos. Chem. Phys.*, **12 (10)**, 4555–4565, doi:10.5194/acp-12-4555-2012.

Hally, A., E. Richard, and V. Ducrocq, 2014: An ensemble study of HyMeX IOP6 and IOP7a: sensitivity to physical and initial and boundary condition uncertainties. *Nat. Hazards Earth Syst. Sci.*, **14 (5)**, 1071–1084, doi:10.5194/nhess-14-1071-2014.

Hamill, T. M., 2001: Interpretation of rank histograms for verifying ensemble forecasts. *Mon. Wea. Rev.*, **129 (3)**, 550–560, doi:10.1175/1520-0493(2001)129⟨0550:IORHFV⟩ 2.0.CO;2.

Bibliography

Holton, J. R., 2004: *An Introduction to dynamic meteorology*, International Geophysics Series, Vol. 88. Elsevier Academic Press, Amsterdam, 535 pp.

Homar, V., A. Jansà, J. Campins, A. Genoves, and C. Ramis, 2007: Towards a systematic climatology of sensitivities of Mediterranean high impact weather: a contribution based on intense cyclones. *Nat. Hazards Earth Syst. Sci.*, **7 (4)**, 445–454, doi: 10.5194/nhess-7-445-2007.

Homar, V., A. Jansà, J. Campins, and C. Ramis, 2006a: Towards a climatology of sensitivities of Mediterranean high impact weather – first approach. *Adv. Geosci.*, **7**, 259–267, doi:10.5194/adgeo-7-259-2006.

Homar, V., C. Ramis, R. Romero, S. Alonso, J. A. García-Moya, and M. Alarcón, 1999: A case of convection development over the Western Mediterranean Sea: A study through numerical simulations. *Meteor. Atmos. Phys.*, **71**, 169–188, doi:10.1007/s007030050054.

Homar, V., R. Romero, C. Ramis, and S. Alonso, 2002: Numerical study of the October 2000 torrential precipitation event over eastern Spain: analysis of the synoptic-scale stationarity. *Ann. Geophys.*, **20**, 2047–2066, doi:10.5194/angeo-20-2047-2002.

Homar, V. and D. J. Stensrud, 2004: Sensitivities of an intense Mediterranean cyclone: Analysis and validation. *Quart. J. Roy. Meteor. Soc.*, **130 (602)**, 2519–2540, doi:10.1256/qj.03.85.

Homar, V., D. J. Stensrud, J. J. Levit, and D. R. Bright, 2006b: Value of human-generated pertubations in short-range ensemble forecasts of severe weather. *Wea. Forecasting*, **21 (3)**, 347–363, doi:10.1175/WAF920.1.

Horvath, K., L. Fita, R. Romero, and B. Ivancan-Picek, 2006: A numerical study of the first phase of a deep Mediterranean cyclone: cyclogenesis in the lee of the Atlas Mountains. *Meteor. Z.*, **15 (2)**, 133–146, doi:10.1127/0941-2948/2006/0113.

Houze, R. A., 1993: *Cloud dynamics*, International Geophysics Series, Vol. 53. Academic Press, San Diego, 573 pp.

Jansà, A., J. Campins, M. A. Picornell, and J. A. Guijarro, 2014a: Heavy rain and strong wind events over Spain during HyMeX SOP1. *Journal of Mediterranean Meteorology and Climatology*, **11**, 25–38, doi:10.3369/tethys.2014.11.03.

Jansà, A., A. Genoves, M. A. Picornell, J. Campins, R. Riosalido, and O. Carretero, 2001: Western Mediterranean cyclones and heavy rain. Part 2: Statistical approach. *Meteorol. Appl.*, **8 (1)**, 43–56, doi:10.1017/S1350482701001049.

Jansà, A., P. Alpert, P. Arbogast, A. Buzzi, B. Ivancan-Picek, V. Kotroni, M. C. Llasat, C. Ramis, E. Richard, R. Romero, and A. Speranza, 2014b: MEDEX: a general overview. *Nat. Hazards Earth Syst. Sci. Discuss.*, **2 (1)**, 535–580, doi:10.5194/nhessd-2-535-2014.

Jolliffe, I. T. and D. B. Stephenson, 2012: *Forecast verification - a practitioner's guide in atmospheric science*. 2d ed., John Wiley and Sons Ltd., Chichester, 240 pp.

Kahl, J. D., J. M. Harris, and G. A. Herbert, 1989: Intercomparison of three long-range trajectory models applied to Arctic haze. *Tellus*, **41 (5)**, 524–536, doi:10.1111/j.1600-0889.1989.tb00139.x.

Kain, J. S., 2004: The Kain–Fritsch convective parameterization: an update. *J. Appl. Meteor.*, **43**, 170–181, doi:10.1175/1520-0450(2004)043⟨0170:TKCPAU⟩2.0.CO;2.

Kain, J. S. and J. M. Fritsch, 1990: A one-dimensional entraining/detraining plume model and its application in convective parameterization. *J. Atmos. Sci.*, **47 (23)**, 2784–2802, doi:10.1175/1520-0469(1990)047⟨2784:AODEPM⟩2.0.CO;2.

Kalnay, E., 2003: *Atmospheric modeling, data assimilation and predictability*. Cambridge University Press, New York, 341 pp.

Kalthoff, N., B. Adler, C. Barthlott, U. Corsmeier, S. Mobbs, S. Crewell, K. Träumner, C. Kottmeier, A. Wieser, V. Smith, and P. D. Girolamo, 2009: The impact of convergence zones on the initiation of deep convection: A case study from COPS. *Atmos. Res.*, **93 (4)**, 680–694, doi:10.1016/j.atmosres.2009.02.010.

Keane, R. J., G. C. Craig, C. Keil, and G. Zängl, 2014: The Plant–Craig stochastic convection scheme in ICON and its scale adaptivity. *J. Atmos. Sci.*, **71**, 3404–3415, doi:10.1175/JAS-D-13-0331.1.

Keane, R. J. and R. S. Plant, 2012: Large-scale length and time-scales for use with stochastic convective parametrization. *Quart. J. Roy. Meteor. Soc.*, **138**, 1150–1164, doi:10.1002/qj.992.

Keil, C. and G. C. Craig, 2009: A displacement and amplitude score employing and optical flow technique. *Wea. Forecasting*, **24**, 1297–1308, doi:10.1175/2009WAF2222247.1.

Khodayar, S., F. Raff, N. Kalthoff, and O. Bock, 2015: Diagnostic study of a high precipitation event in the Western Mediterranean region: adequacy of current operational networks. *Quart. J. Roy. Meteor. Soc.*, doi:10.1002/qj.2600.

Kidd, C., P. Bauer, J. Turk, G. J. Huffman, R. Joyce, K.-L. Hsu, and D. Braithwaite, 2012: Intercomparison of high-resolution precipitation products over Northwest Europe. *J. Hydrometeorol.*, **13 (1)**, 67–83, doi:10.1175/JHM-D-11-042.1.

Klüpfel, V., N. Kalthoff, L. Gantner, and C. Kottmeier, 2011: Evaluation of soil moisture ensemble runs to estimate precipitation variability in convection-permitting model simulations for West Africa. *Atmos. Res.*, **101 (1-2)**, 178–193, doi:10.1016/j.atmosres.2011.02.008.

Klüpfel, V., N. Kalthoff, L. Gantner, and C. M. Taylor, 2012: Convergence zones and their impact on the initiation of a mesoscale convective system in West Africa. *Quart. J. Roy. Meteor. Soc.*, **138**, 950–963, doi:10.1002/qj.979.

Bibliography

Kober, K., A. M. Foerster, and G. C. Craig, 2015: Examination of a stochastic and deterministic convection parameterization in the COSMO model. *Mon. Wea. Rev.*, **143 (10)**, 4088–4103, doi:10.1175/MWR-D-15-0012.1.

Kottek, M., J. Grieser, C. Beck, B. Rudolf, and F. Rubel, 2006: World map of the Köppen-Geiger climate classification updated. *Meteor. Z.*, **15 (3)**, 259–263(5), doi:10.1127/0941-2948/2006/0130.

Kottmeier, C. and B. Fay, 1998: Trajectories in the Antarctic lower troposphere. *J. Geophys. Res.*, **103 (D9)**, 10 947–10 959, doi:10.1029/97JD00768.

Kottmeier, C., N. Kalthoff, C. Barthlott, U. Corsmeier, J. van Baelen, A. Behrendt, R. Behrendt, A. Blyth, R. Coulter, S. Crewell, P. D. Girolamo, M. Dorninger, C. Flamant, T. Foken, M. Hagen, C. Hauck, H. Holler, H. Konow, M. Kunz, H. Mahlke, S. Mobbs, E. Richard, R. Steinacker, T. Weckwerth, A. Wieser, and V. Wulfmeyer, 2008: Mechanisms initiating deep convection over complex terrain during COPS. *Meteor. Z.*, **17 (6)**, 931–948, doi:10.1127/0941-2948/2008/0348.

Kraut, I., 2015: Separating the aerosol effect in case of a "Medicane". Ph.D. thesis, Karlsruhe Institute of Technology.

Kunz, M., 2007: The skill of convective parameters and indices to predict isolated and severe thunderstorms. *Nat. Hazards Earth Syst. Sci.*, **7 (2)**, 327–342, doi:10.5194/nhess-7-327-2007.

Lambert, D., M. Mallet, V. Ducrocq, F. Dulac, F. Gheusi, and N. Kalthoff, 2011: CORSiCA: a Mediterranean atmospheric and oceanographic observatory in Corsica within the framework of HyMeX and ChArMEx. *Adv. Geosci.*, **26**, 125–131, doi:10.5194/adgeo-26-125-2011.

Lenz, C.-J., U. Corsmeier, and C. Kottmeier, 2012: Numerical modelling of Mediterranean cyclones. *High performance computing in science and engineering '11*, W. E. Nagel, D. B. Kröner, and M. M. Resch, Eds., Springer Berlin Heidelberg, 489–501, doi:10.1007/978-3-642-23869-7_35.

Leutbecher, M. and T. Palmer, 2008: Ensemble forecasting. *J. Comput. Phys.*, **227 (7)**, 3515–3539, doi:10.1016/j.jcp.2007.02.014.

Lin, Y.-L., S. Chiao, T.-A. Wang, M. L. Kaplan, and R. P. Weglarz, 2001: Some common ingredients for heavy orographic rainfall. *Wea. Forecasting*, **16 (6)**, 633–660, doi:10.1175/1520-0434(2001)016⟨0633:SCIFHO⟩2.0.CO;2.

Lionello, P., 2006: *Mediterranean climate variability*. Elsevier Academic Press, Amsterdam, 421 pp.

Lionello, P., 2012: *The climate of the Mediterranean region*. Elsevier Academic Press, Amsterdam, 502 pp.

Llasat-Botija, M., M. C. Llasat, and L. López, 2007: Natural hazards and the press in the western Mediterranean region. *Adv. Geosci.*, **12**, 81–85, doi:10.5194/adgeo-12-81-2007.

Lorenz, E. N., 1963: Deterministic nonperiodic flow. *J. Atmos. Sci.*, **20 (2)**, 130–141, doi:10.1175/1520-0469(1963)020⟨0130:DNF⟩2.0.CO;2.

MacQueen, J., 1976: Some methods for classification and analysis of multivariate observations. *Proceedings of the fifth Berkeley symposium on mathematical statistics and probability*, L. Lecam and J. Neyman, Eds., Vol. 1, 281–297.

Maddox, R. A., 1980: Mesoscale convective complexes. *Bull. Amer. Meteor. Soc.*, **61 (11)**, 1374–1387.

Markowski, P. and Y. Richardson, 2010: *Mesoscale meteorology in midlatitudes*, Vol. 2. John Wiley and Sons Ltd., Chichester, 407 pp.

Marshall, J. S. and W. M. K. Palmer, 1948: The distribution of raindrops with size. *J. Meteor.*, **5 (4)**, 165–166, doi:10.1175/1520-0469(1948)005⟨0165:TDORWS⟩2.0.CO;2.

Marsigli, C., F. Boccanera, A. Montani, and T. Paccangnella, 2005: The COSMO-LEPS mesoscale ensemble system: validation of the methodology and verification. *Nonlin. Process. Geophys.*, **12 (4)**, 527–536, doi:10.5194/npg-12-527-2005.

Marsigli, C., A. Montani, and T. Paccangnella, 2008: A spatial verification method applied to the evaluation of high-resolution ensemble forecasts. *Meteorol. Appl.*, **15 (1)**, 125–143, doi:10.1002/met.65.

Martinez, C., J. Campins, A. Jansà, and A. Genoves, 2008: Heavy rain events in the Western Mediterranean: an atmospheric pattern classification. *Adv. Sci. Res.*, **2**, 61–64, doi:10.5194/asr-2-61-2008.

Mehta, A. V. and S. Yang, 2008: Precipitation climatology over Mediterranean basin from ten years of TRMM measurements. *Adv. Geosci.*, **17**, 87–91, doi:10.5194/adgeo-17-87-2008.

Mittermaier, M. P., 2007: Improving short-range high-resolution model precipitation forecast skill using time-lagged ensembles. *Quart. J. Roy. Meteor. Soc.*, **133 (627)**, 1487–1500, doi:10.1002/qj.135.

Molteni, F., R. Buizza, C. Marsigli, A. Montani, F. Nerozzi, and T. Paccagnella, 2001: A strategy for high-resolution ensemble prediction. I: Definition of representative members and global-model experiments. *Quart. J. Roy. Meteor. Soc.*, **127 (576)**, 2069–2094, doi:10.1002/qj.49712757612.

Montani, A., D. Cesari, C. Marsigli, and T. Paccangnella, 2011: Seven years of acivity in the field of mesoscale ensemble forecasting by the COSMO-LEPS system: main achievements and open challenges. *Tellus*, **63 (3)**, 605–624, doi:10.1111/j.1600-0870.2010.00499.x.

Bibliography

Neiman, P. J., F. M. Ralph, A. White, D. Kingsmill, and P. Persson, 2002: The statistical relationship between upslope flow and rainfall in California's coastal mountains: observations during CALJET. *Mon. Wea. Rev.*, **130 (6)**, 1468–1492, doi: 10.1175/1520-0493(2002)130⟨1468:TSRBUF⟩2.0.CO;2.

Nyquist, H., 1924: Certain factors affecting telegraph speed. *American Telephone and Telegraph Co., New York, N. Y.*, **XLIII**, 412–422, doi:10.1109/T-AIEE.1924.5060996.

Oke, T., 2002: *Boundary layer climates*. Methuen, London, 435 pp.

Palmer, T., G. Shutts, R. Hagedorn, F. Doblas-Reyes, T. Jung, and M. Leutbecher, 2005: Representing model uncertainty in weather and climate prediction. *Annu. Rev. Earth Planet. Sci.*, **33**, 163–193, doi:10.1146/annurev.earth.33.092203.122552.

Palmer, T. and S. Tibaldi, 1988: On the prediction of forecast skill. *Mon. Wea. Rev.*, **116 (12)**, 2453–2480, doi:10.1175/1520-0493(1988)116⟨2453:OTPOFS⟩2.0.CO;2.

Pascual, R. and A. Callado, 2002: Mesoanalysis of recurrent convergence zones in northeastern Iberian Peninsula. *Radar Meteorology (ERAD)*, 59–64.

Pascual, R., A. Callado, and M. Berenguer, 2004: Convective storm initiation in central Catalonia. *Radar Meteorology (ERAD)*, 464–468.

Pfahl, S. and H. Wernli, 2012: Quantifying the relevance of cyclones for precipitation extremes. *J. Climate*, **25 (19)**, 6770–6780, doi:10.1175/JCLI-D-11-00705.1.

Plant, R. and G. Craig, 2008: A stochastic parameterization for deep convection based on equilibrium statistics. *J. Atmos. Sci.*, **65 (1)**, 87–105, doi:10.1175/2007JAS2263.1.

Pytharoulis, I., G. C. Craig, and S. P. Ballard, 2000: The hurricane-like Mediterranean cyclone of January 1995. *Meteorol. Appl.*, **7 (3)**, 261–279, doi:10.1017/S1350482700001511.

Quintana, P., V. Homar, M. C. Llasat, A. Jansà, J. Font, and M. Aran, 2012: A look to the HyMeX program. *Journal of Mediterranean Meteorology and Climatology*, **9**, 53–63, doi:10.3369/tethys.2012.9.06.

Ramis, C., V. Homar, A. Amengual, R. Romero, and S. Alonso, 2013: Daily precipitation records over mainland Spain and the Balearic Islands. *Nat. Hazards Earth Syst. Sci.*, **13 (10)**, 2483–2491, doi:10.5194/nhess-13-2483-2013.

Ramis, C., R. Romero, and V. Homar, 2009: The severe thunderstorm of 4 October 2007 in Mallorca: an observational study. *Nat. Hazards Earth Syst. Sci.*, **9 (4)**, 1237–1245, doi:10.5194/nhess-9-1237-2009.

Reale, O., L. Feudale, and B. Turato, 2001: Evaporative moisture sources during a sequence of floods in the Mediterranean region. *Geophys. Res. Lett.*, **28 (10)**, 2085–2088, doi:10.1029/2000GL012379.

Reiff, J., G. S. Forbes, F. T. M. Spieksma, and J. J. Reynders, 1986: African dust reaching northwestern Europe: a case study to verify trajectory calculations. *J. Clim. Appl. Meteorol.*, **25**, 1543–1567, doi:10.1175/1520-0450(1986)025⟨1543:ADRNEA⟩2.0.CO;2.

Ricard, D., V. Ducrocq, and L. Auger, 2012: A climatology of the mesoscale environment associated with heavily precipitating events over a Northwestern Mediterranean area. *J. Clim. Appl. Meteorol.*, **51 (3)**, 468–488, doi:10.1175/JAMC-D-11-017.1.

Roe, G. H., 2005: Orographic precipitation. *Annu. Rev. Earth Planet. Sci.*, **33**, 645–671, doi:10.1146/annurev.earth.33.092203.122541.

Roebber, P. J., D. M. Schultz, and R. Romero, 2002: Synoptic regulation of the 3 May 1999 tornado outbreak. *Wea. Forecasting*, **17 (3)**, 399–429, doi:10.1175/ 1520-0434(2002)017⟨0399:SROTMT⟩2.0.CO;2.

Romero, R., 2001: Sensitivity of a heavy-rain-producing western Mediterranean cyclone to embedded potential-vorticity anomalies. *Quart. J. Roy. Meteor. Soc.*, **127 (578)**, 2559–2597, doi:10.1002/qj.49712757805.

Romero, R., C. A. Doswell, and C. Ramis, 2000: Mesoscale numerical study of two cases of long-lived quasi-stationary convective systems over eastern Spain. *Mon. Wea. Rev.*, **128 (11)**, 3731–3751, doi:10.1175/1520-0493(2001)129⟨3731:MNSOTC⟩2.0.CO;2.

Romero, R. and K. Emanuel, 2013: Medicane risk in a changing climate. *J. Geophys. Res.*, **118 (12)**, 5992–6001, doi:10.1002/jgrd.50475.

Romero, R., C. Ramis, and V. Homar, 2014: On the severe convective storm of 29 October 2013 in the Balearic Islands: observational and numerical study. *Quart. J. Roy. Meteor. Soc.*, **141 (689)**, 1208–1222, doi:10.1002/qj.2429.

Romero, R., G. Sumner, C. Ramis, and A. Genoves, 1999: A classification of the atmospheric circulation patterns producing significant daily rainfall in the spanish Mediterranean area. *Int. J. Climatol.*, **19 (7)**, 765–785, doi:10.1002/(SICI) 1097-0088(19990615)19:7⟨765::AID-JOC388⟩3.0.CO;2-T.

Rossby, C.-G., 1932: Thermodynamics applied to air mass analysis. *Meteorological Papers*, **1**, 1–57, doi:10.1575/1912/1139.

Rysman, J.-F., C. Claud, J.-P. Chaboureau, J. Delanoë, and B. M. Funatsu, 2015: Severe convection in the Mediterranean from microwave observations and a convection-permitting model. *Quart. J. Roy. Meteor. Soc.*, doi:10.1002/qj.2611.

Röhner, L., K.-U. Nerding, and U. Corsmeier, 2016: Diagnostic study of a HyMeX heavy precipitation event over Spain by investigation of moisture trajectories. *Quart. J. Roy. Meteor. Soc.*, doi:10.1002/qj.2825.

Sanchez, E., C. Gallardo, M. Gaertner, A. Arribas, and M. Castro, 2004: Future climate extreme events in the Mediterranean simulated by a regional climate model: a first approach. *Glob. Planet. Chang.*, **44 (1-4)**, 163–180, doi:10.1016/j.gloplacha.2004.06. 010.

Scherrer, S. C., C. Appenzeller, P. Eckert, and D. Cattani, 2004: Analysis of the spread–skill relations using the ECMWF ensemble prediction system over Europe. *Wea. Forecasting*, **19 (3)**, 552–565, doi:10.1175/1520-0434(2004)019⟨0552:AOTSRU⟩2.0.CO;2.

Schumacher, R. S. and A. J. Clark, 2014: Evaluation of ensemble configurations for the analysis and prediction of heavy-rain-producing mesoscale convective systems. *Mon. Wea. Rev.*, **142 (11)**, 4108–4138, doi:10.1175/MWR-D-13-00357.1.

Schättler, U., G. Doms, and C. Schraff, 2012: *A description of the nonhydrostatic regional COSMO-model. Part VII: User's guide*. Deutscher Wetterdienst, Offenbach, 192 pp.

Seity, Y., P. Brousseau, S. Malardel, G. Hello, P. Bénard, F. Bouttier, C. Lac, and V. Masson, 2011: The AROME-France convective-scale operational model. *Mon. Wea. Rev.*, **139 (3)**, 976–991, doi:10.1175/2010MWR3425.1.

Sekhon, R. S. and R. C. Srivastava, 1971: Doppler radar observations of drop-size distributions in a thunderstorm. *J. Atmos. Sci.*, **28 (6)**, 983–994, doi:10.1175/1520-0469(1971)028⟨0983:DROODS⟩2.0.CO;2.

Shaw, W. N., 1903: The meteorological aspects of the storm of February 26–27, 1903. *Quart. J. Roy. Meteor. Soc.*, **29 (128)**, 233–262, doi:10.1002/qj.49702912801.

Sherwood, S. C., 2000: On moist instability. *Mon. Wea. Rev.*, **128 (12)**, 4139–4142, doi:10.1175/1520-0493(2000)129⟨4139:OMI⟩2.0.CO;2.

Simpson, J., R. F. Adler, and G. R. North, 1988: A proposed tropical rainfall measuring mission (TRMM) satellite. *Bull. Amer. Meteor. Soc.*, **69 (3)**, 278–295, doi:10.1175/1520-0477(1988)069⟨0278:APTRMM⟩2.0.CO;2.

Smith, R. B., 1979: The influence of mountains on the atmosphere. *Adv. Geosci.*, **21**, 87–230.

Sprenger, M. and H. Wernli, 2015: The Lagrangian analysis tool LAGRANTO - version 2.0. *Geosci. Model Dev. Discuss.*, **8 (2)**, 1893–1943, doi:10.5194/gmdd-8-1893-2015.

Stein, U. and P. Alpert, 1993: Factor separation in numerical simulations. *J. Atmos. Sci.*, **50 (14)**, 2107–2115, doi:10.1175/1520-0469(1993)050⟨2107:FSINS⟩2.0.CO;2.

Steppeler, J., G. Doms, U. Schattler, H. W. Bitzer, A. Gassmann, U. Damrath, and G. Gregoric, 2003: Meso-gamma scale forecasts using the nonhydrostatic model LM. *Meteor. Atmos. Phys.*, **82 (1-4)**, 75–96, doi:10.1007/s00703-001-0592-9.

Stevens, B., 2005: Atmospheric moist convection. *Annu. Rev. Earth Planet. Sci.*, **33**, 605–643, doi:10.1146/annurev.earth.33.092203.122658.

Stohl, A., 1998: Computation, accuracy and applications of trajectories—a review and bibliography. *Atmos. Environ.*, **32 (6)**, 947–966, doi:10.1016/S1352-2310(97)00457-3.

Stull, R. B., 1988: *An introduction to boundary layer meteorology*. Kluwer Academic Publishers, Dordrecht, 670 pp.

Tiedtke, M., 1989: A comprehensive mass flux scheme for cumulus parameterization in large-scale models. *Mon. Wea. Rev.*, **117 (8)**, 1779–1800, doi:10.1175/1520-0493(1989)117⟨1779:ACMFSF⟩2.0.CO;2.

Tous, M. and R. Romero, 2012: Meteorological environments associated with medicane development. *Int. J. Climatol.*, **33 (1)**, 1–14, doi:10.1002/joc.3428.

Tuduri, E. and C. Ramis, 1997: The environments of significant convective events in the Western Mediterranean. *Wea. Forecasting*, **12 (2)**, 294–306, doi:10.1175/1520-0434(1997)012⟨0294:TEOSCE⟩2.0.CO;2.

Turner, S., J.-L. Brenguier, and C. Lac, 2012: A subgrid parameterization scheme for precipitation. *Geosci. Model Dev.*, **5 (2)**, 499–521, doi:10.5194/gmd-5-499-2012.

Uppala, S. M., P. W. Kallberg, A. J. Simmons, U. Andrae, V. D. C. Bechtold, M. Fiorino, J. K. Gibson, J. Haseler, A. Hernandez, G. A. Kelly, X. Li, K. Onogi, S. Saarinen, N. Sokka, R. P. Allan, E. Andersson, K. Arpe, M. A. Balmaseda, A. C. M. Beljaars, L. V. D. Berg, J. Bidlot, N. Bormann, S. Caires, F. Chevallier, A. Dethof, M. Dragosavac, M. Fisher, M. Fuentes, S. Hagemann, E. Holm, B. J. Hoskins, L. Isaksen, P. A. E. M. Janssen, R. Jenne, A. P. Mcnally, J. Mahfouf, J.-J. Morcrette, N. A. Rayner, R. W. Saunders, P. Simon, A. Sterl, K. E. Trenberth, A. Untch, D. Vasiljevic, P. Viterbo, and J. Woollen, 2005: The ERA-40 re-analysis. *Quart. J. Roy. Meteor. Soc.*, **131 (612)**, 2961–3012, doi:10.1256/qj.04.176.

U.S. Government Printing Office, W., 1976: U.S. standard atmosphere, 1976.

Vich, M., R. Romero, and V. Homar, 2011: Ensemble prediction of Mediterranean high-impact events using potential vorticity pertubations. Part II: Adjoint-derived sensitivity zones. *Atmos. Res.*, **102 (3)**, 311–319, doi:10.1016/j.atmosres.2011.07.016.

Vie, B., O. Nuissier, and V. Ducrocq, 2011: Cloud-resolving ensemble simulations of Mediterranean heavy precipitating events: uncertainty on initial conditions and lateral boundary conditions. *Mon. Wea. Rev.*, **139 (2)**, 403–423, doi:10.1175/2010MWR3487.1.

Weigel, A. P., M. A. Liniger, and C. Appenzeller, 2008: Can multi-model combination really enhance the prediction skill of probabilistic ensemble forecasts? *Quart. J. Roy. Meteor. Soc.*, **134 (630)**, 241–260, doi:10.1002/qj.210.

Weisman, M. L., W. C. Skamarock, and J. B. Klemp, 1997: The resolution dependence of explicitly modeled convective systems. *Mon. Wea. Rev.*, **125 (4)**, 527–548, doi:10.1175/1520-0493(1997)125⟨0527:TRDOEM⟩2.0.CO;2.

Wernli, H., 1997: A Lagrangian-based analysis of extratropical cyclones. II: A detailed case-study. *Quart. J. Roy. Meteor. Soc.*, **123 (542)**, 1677–1706, doi:10.1002/qj.49712354211.

Wernli, H. and H. C. Davies, 1997: A Lagrangian-based analysis of extratropical cyclones. I: The method and some applications. *Quart. J. Roy. Meteor. Soc.*, **123 (538)**, 467–489, doi:10.1002/qj.49712353811.

Bibliography

Wernli, H., C. Hofmann, and M. Zimmer, 2009: Spatial forecast verification methods intercomparison project: application of the SAL technique. *Wea. Forecasting*, **24 (6)**, 1472–1484, doi:10.1175/2009WAF2222271.1.

Wernli, H., M. Paulat, M. Hagen, and C. Frei, 2008: SAL - a novel quality measure for the verification of quantitative precipitation forecasts. *Mon. Wea. Rev.*, **136 (11)**, 4470–4487, doi:10.1175/2008MWR2415.1.

Whitaker, J. S. and A. F. Loughe, 1998: The relationship between ensemble spread and ensemble mean skill. *Mon. Wea. Rev.*, **126 (12)**, 3292–3302, doi:10.1175/1520-0493(1998)126⟨3292:TRBESA⟩2.0.CO;2.

Wilks, D. S., 1995: *Statistical methods in the atmospheric sciences*. Academic Press, San Diego, 467 pp.

Wüest, M., C. Frei, A. Altenhoff, M. Hagen, M. Litschi, and C. Schär, 2010: A gridded hourly precipitation dataset for Switzerland using rain-gauge analysis and radar-based disaggregation. *Int. J. Climatol.*, **30 (12)**, 1764–1775, doi:10.1002/joc.2025.

Yanai, M., S. Esbensen, and J.-H. Chu, 1973: Determination of bulk properties of Tropical cloud clusters from large-scale heat and moisture budgets. *J. Atmos. Sci.*, **30 (4)**, 611–627, doi:10.1175/1520-0469(1973)030⟨0611:DOBPOT⟩2.0.CO;2.

Ziegler, C. L. and E. N. Rasmussen, 1998: The initiation of moist convection at the dryline: forecasting issues from a case study perspective. *Wea. Forecasting*, **13 (4)**, 1106–1131, doi:10.1175/1520-0434(1998)013⟨1106:TIOMCA⟩2.0.CO;2.

Zimmer, M. and H. Wernli, 2011: Verification of quantitative precipitation forecasts on short time-scales: A fuzzy approach to handle timing errors with SAL. *Meteor. Z.*, **20 (2)**, 95–105, doi:10.1127/0941-2948/2011/0224.

Acknowledgements

Mehr als drei Jahre sind nun seit dem Start dieser Dissertation vergangen. Viele viele Menschen haben mich auf diesem Weg ein Stück begleitet. Sie teilten ihr Wissen mit mir, lieferten mir Daten, stellten die richtigen Fragen, diskutierten mit mir über Methoden und Ergebnisse, waren einfach da ... und haben mich somit auf die ein oder andere Art und Weise unterstützt. Danken möchte ich insbesondere:

Víctor Homar: Without you, this thesis would never have come so far. You hosted me for three months in your working group in Mallorca and inducted me into the fascinating world of verification and ensemble forecasting. After my stay at UIB you were continuously interested in my working progress, you took the time to discuss with me as often as possible and you always believed in me. Molt gràcies!

Ulli Corsmeier: Schon seit 2009 durfte ich in deiner Arbeitsgruppe "Konvektive Systeme" mitarbeiten. Egal ob als HiWi oder als Doktorandin habe ich dein meteorologisches Fachwissen immer sehr geschätzt. Vielen Dank, dass du mich so lange Zeit unterstützt und betreut hast, immer offen für Fragen warst und durch viele Diskussionen diese Doktorarbeit weit voran gebracht hast.

Christoph Kottmeier: Dass Sie mich als Doktorandin angenommen haben hat diese Doktorarbeit überhaupt erst möglich gedacht. Und die Gespräche mit Ihnen sorgten jedesmal dafür, dass ich die übergeordneten Fragestellungen wieder vor Augen hatte und mich nicht zu sehr in technischen Details verlor. Dafür danke ich Ihnen sehr!

PANDOWAE: Durch dieses Forschungsprojekt (FOR 896) wurde diese Arbeit finanziert. Doch PANDOWAE war viel mehr als das. Bei vielen Gesamtworkshops konnte ich meine Arbeitsfortschritte einer immer sehr interessierten Zuhörerschaft präsentieren. Auch für das nicht-meteorologische Wohl gab es immer wieder tolle Veranstaltungen zu diversen "softskills". Besonders hervorheben möchte ich aber die tolle YS-Gemeinschaft innerhalb von PANDOWAE. Und mich an dieser Stelle vor allem für die Unterstützung meiner Mitdoktorand(inn)en **Evi Giannakaki**, **Franziska Gierth**, **Hilke Lentink**, **Julian Quinting**, **Lisa Quandt** und **Gabriel Wolf** bedanken.
Die Auswertungen mit dem Konvektionsschema "Plant-Craig" wurden hauptsächlich von **George Craig** initiiert. Für das Implementieren des Schemas in COSMO danke ich außerdem **Tobias Selz**.

HyMeX: Many discussions at several workshops of this Mediterranean research project developed my work significantly. And without the provided data I could not have gained the presented results. Special thank goes here to **Andrea Montani** for the COSMO-LEPS data and to **Laurent Labatut** for the radar data.